RADARSAT-2 Polarimetric Radar Imaging for Lake Ice Mapping

by

Feng Pan

A thesis

presented to the University of Waterloo

in the fulfilment of the

thesis requirement for the degree of

Master of Science

in

Geography

Waterloo, Ontario, Canada, 2017

AUTHOR'S DECLARATION

I hereby declare that I am the sole author of this thesis. This is a true copy of the thesis, including any required final revisions, as accepted by my examiners.

I understand that my thesis may be made electronically available to the public.

Abstract

Changes in lake ice dates and duration are useful indicators for assessing long-term climate trends and variability in northern countries. Lake ice cover observations are also a valuable data source for predictions with numerical ice and weather forecasting models. In recent years, satellite remote sensing has assumed a greater role in providing observations of lake ice cover extent for both modeling and climate monitoring purposes. Polarimetric radar imaging has become a promising tool for lake ice mapping at high latitudes where cloud cover and polar darkness severely limit observations from optical sensors. In this study, we assessed and characterized the physical scattering mechanisms of lake ice from fully polarimetric RADARSAT-2 datasets obtained over Great Bear Lake, Canada, with the intent of classifying open water and ice cover during the freeze-up and break-up periods. Model-based and eigen-based decompositions were employed to construct the coherency matrix into deterministic scattering mechanisms, and secondary physical parameters were generated following the polarimetric decompositions. This study presents an application of the Markov Random Field by introducing radar signals and polarimetric parameters as features. These features were labeled using the entropy-alpha Wishart classifier. We show that the selected polarimetric parameters can help with interpretation of radar-ice/water interactions and can be used successfully for water-ice segmentation. As more satellite SAR sensors are being launched or planned, such as the Sentinel-1a/b series and the upcoming RADARSAT Constellation Mission, the rapid volume growth of data and their analysis require the development of robust automated algorithms. The approach developed in this study was therefore designed with the intent of moving towards fully automated mapping of lake ice for consideration by ice services.

Acknowledgements

This thesis could not have been possible without the support, generosity and assistance of many individuals, and it is truly impossible to fully acknowledge everyone.

My sincere gratitude goes to my supervisor, Dr. Claude Duguay, for his guidance, support and patience throughout the years to overcome difficult circumstances and complete this research. I am extremely appreciative of the freedom that you have given me to study and explore on my own and the guidance to steer me back on track. I hope to replicate your dedication and enthusiasm to the field that I am immersed in for the following years, and I am deeply grateful for the philosophy of life that I learned from you.

I would like to extend my appreciation to Dr. Richard Kelly, Dr. Andrea Scott, and Dr. Homa Kheyrollah Pour for serving as my committee members and readers on this thesis. Your continued advice and support have made this thesis possible. I also gratefully acknowledge Véronique Pinard, of the Canadian Ice Service, Environment and Climate Change Canada for her work on the accuracy assessment of this study.

I would like to thank all of the friends I have met during my time at the University of Waterloo. In particular, I have been fortunate to have the support of Aaron Thompson, Qinghuan Li, Paul Donchenko, Jeffrey Chan, Vicky Vanthof, Janine Naijnath, Sofya Antonova, and Jessie Tang. A special thanks to all those friends outside of academics, who have actively supported me for the past years, including Zhexuan Wang, Zhaoyan Wu, Qinghuan Li, and Xianda Sun. At the same time, I mourn the loss of my friend, Fan Li. A thanks also to all my team colleagues: Homa Kheyrollah Pour, Cristina Surdu, Junqian Wang, Marie Hoekstra. A special thanks to Kevin (Kyung-Kuk) Kang, who undertook a monumental effort to make another's life difficult; I learned a lot from his "Les Misérables".

Most importantly, I would like to thank my family for their support and faith during this journey. I am extremely grateful to my girlfriend, Hongjing, for being my sounding board and harbour. Thank you to my family, especially my parents and Hongjing's parents, who supported me continuously in getting to this point.

Table of Contents

List of Figures

List of Tables

List of Symbols

∇f	Gradient of a scalar field f
$\nabla \cdot \boldsymbol{A}$	Divergence of a vector field **A**
$\nabla \times \boldsymbol{A}$	Curl of a vector field **A**
∇^2	Laplace operator, the divergence of the gradient of a function
$\boldsymbol{E}$	Electric field
$\boldsymbol{D}$	Electric displacement field
$\boldsymbol{P}$	Electric polarization or polarization density
ε	Permittivity
ε_0	Vacuum permittivity
ε_r	Relative permittivity
ρ	Total volume charge density
ρ_f	Volume density of free charges
ρ_b	Volume density of bound charges
$\boldsymbol{H}$	Magnetic field or magnetic field strength or intensity
$\boldsymbol{B}$	Magnetic induction
$\boldsymbol{M}$	Magnetization
μ	Permeability
μ_0	Magnetic permeability of free space
μ_r	Relative permeability
$\boldsymbol{J}$	Total current density
$\boldsymbol{J_0}$	Conduction current density ($\boldsymbol{J_0} = \sigma \boldsymbol{E}$)
$\boldsymbol{J_c}$	Convection current density

c	The speed of light in vacuum
χ	Susceptibility
σ	Conductivity (1/ ρ)
ρ	Resistivity
T	Period
ω	Angular frequency ($\omega = \frac{2\pi}{T}$)
λ	Wavelength
k	Wave number or spatial frequency ($k = \frac{2\pi}{\lambda}$)
φ	Phase at the origin
j	Imaginary unit
A	Ellipse amplitude
ϕ	Ellipse orientation
τ	Ellipticity or ellipse aperture
$\boldsymbol{J}$	Jones Vector
$\boldsymbol{I}_n$	$n \times n$ identity matrix
$\boldsymbol{\sigma}_n$	Pauli spin matrices, where $\boldsymbol{\sigma}_0$ is I_2
$\boldsymbol{V}^*$	Conjugate of the vector $\boldsymbol{V}$
$\boldsymbol{V}^T$	Transpose of the vector $\boldsymbol{V}$
$\boldsymbol{g}$	Stokes vector
P	Power
S	Power density
G	Antenna gain
A_e	Antenna effective aperture
σ	Radar cross section

σ^0	Scattering coefficient
$\boldsymbol{S}$	Scattering matrix
$\boldsymbol{k}$	Scattering vector
$\boldsymbol{\psi}$	Basis matrices or matrix set
$Trace(\boldsymbol{A})$	Trace of the square matrix $\boldsymbol{A}$
$Span(\boldsymbol{S})$	Total power of scattering, span
r_{co}	Co-polarization ratio
r_{cross}	Cross-polarization ratio
r_{depol}	Depolarization ratio
ϕ	Co-polarization phase difference
ρ	Co-polarized correlation coefficient
$\boldsymbol{C}$	Covariance matrix
$\boldsymbol{T}$	Coherency matrix
$\boldsymbol{U}$	Unitary matrix
$\boldsymbol{\Sigma}$	Diagonal eigenvalue matrix
λ	Eigenvalue
$\boldsymbol{u}$	Eigenvector
α	Alpha angle
P	Probability
H	Entropy
$\bar{\alpha}$	Weighted average of alpha angle
$Real(x)$	Real part of the complex number x
N	Number of looks

Δr	Range spacing
Δa	Azimuth spacing
θ	Incidence angle
i	Real component of a signal
q	Imaginary components of a signal
A	Amplitude of a polarization
I	Intensity
e	Mathematical constant, the base of the natural logarithm
$\mathcal{N}(\dots)$	Gaussian distribution
$\mathcal{E}xp(\dots)$	Exponential distribution
$\chi^2(\dots)$	Chi-squared distribution
$\mathrm{E}(\dots)$	Mean or expectation
$\mathrm{Var}(\dots)$	Mean or expectation
μ	Mean or expectation of a distribution
σ	Standard deviation
σ^2	Variance
$\Gamma(\dots)$	Gamma function or Gamma distribution
$\mathrm{K}_\alpha(\dots)$	Modified Bessel function of the second kind
$\mathrm{I}_\alpha(\dots)$	Modified Bessel function of the first kind
$argmax$	Arguments of the maxima
S	Graph
Λ	Range of the classes where label can choose from
ω	Class
C	Clique
U	Energy function

Ω	Labeling conditions
V_c	Clique potential
i	Real part of the polarization signal
q	Imaginary part of the polarization signal
σ^0	Sigma nought, radar backscatter coefficient
β^0	Beta nought, radar brightness
γ^0	Gamma nought
α	Local incidence angle
S	Scattering amplitude

List of Abbreviations

DN	Digital number
ECCC	Environment and Climate Change Canada
CIS	Canadian Ice Service
SAR	Synthetic Aperture Radar
NASA	National Aeronautics and Space Administration
JPL	NASA Jet Propulsion Laboratory
CSA	Canadian Space Agency
ESA	European Space Agency
RCM	RADARSAT Constellation Mission
MDA	MacDonald, Dettwiler and Associates Ltd.
MAP	Maximum a Posteriori
EM	Expectation Maximization
MRF	Markov Random Field
SQnW	Wide Standard Quad-Polarization Beam Mode at n^{th} swath position
ROI	Region of Interest
dB	Decibels
MHz	Megahertz
kHz	kilohertz
m	Metre
km	Kilometre

1 Introduction

1.1 General Introduction

In Canada, over 4 million square kilometres of waters are covered by ice in winter (Canadian Ice Service [CIS], 2017). Lake ice, river ice, sea ice, icebergs and other forms of ice are observed, recorded, and reported by CIS. The monitoring of ice cover is essential due to its profound impacts on Canadian life in many ways: aquatic ecology, economics, marine transportation, fishing, resource development, and tourism (CIS, 2017).

Lakes are widespread land features and are covered by ice for many months of the year in most regions of Canada. Ice cover is an important component of the Canadian cryosphere (Duguay et al., 2006). Ice cover is governed by the following processes: supercooling of the water, initial ice formation, ice thickening, and ice cover breakup (Ashton, 1986). Lake ice phenology (freeze-up, break-up, and duration) is strongly influenced by local weather/climate conditions and global climate change (Duguay et al., 2015); therefore, lake ice has been proven to be a sensitive indicator of climatic variability and change (Duguay et al., 2006; Colbeck, 2012; Brown & Duguay, 2012). Ice dates and duration play a key role in weather and climate, balancing cryosphere-atmosphere energy interactions, controlling heat fluxes, and have an impact important hydrological, ecological and economical implications (Duguay et al., 2006; Brown & Duguay, 2012; Du et al., 2017). More specifically, lake ice has a significant influence on aquatic life including the composition and abundance of aquatic species, and human activities including marine transportation, fishing, resource development, and tourism (Du et al., 2017; CIS, 2017).

Canadian studies have been conducted on observing, monitoring, and documenting lake ice for many years (e.g. Duguay et al., 2006; Geldsetzer, van der Sanden, & Brisco, 2010). Due to the increasing need for monitoring lake ice cover across Canada in the context of improved numerical weather forecasting, the CIS is actively employing remote sensing technology as an operational tool. Since many lakes are located at high latitudes, monitoring of ice cover is limited when using optical sensors alone due to polar darkness and extensive cloud cover (Gurney, Foster, &

Parkinson, 1993; Warner, Foody, & Nellis, 2009). Although passive microwave remote sensing has its unique value for global mapping, the main drawback of passive microwave sensors is the coarse spatial resolution (tens of km) they offer (Ulaby, Moore, & Fung, 1981). Active microwave remote sensing is not only insusceptible to solar illumination conditions and cloud cover, but is also capable of providing details with much finer spatial resolution (tens of meters or better) (Ulaby, Moore, & Fung, 1981). Thus, active microwave remote sensing has become the preferred choice for lake ice monitoring (Duguay et al., 2002; Nghiem & Leshkevich, 2007; Geldsetzer, van der Sanden & Brisco, 2010; Geldsetzer & van der Sanden, 2013; Leshkevich & Nghiem, 2013).

Synthetic Aperture Radar (SAR) is the most common imaging active microwave sensor. In the 1960s, as SAR was derestricted from military purposes and could be used for civilian applications, its development flourished (Natural Resources Canada [NRC], 2017). SEASAT, the first civilian SAT satellite, was launched in 1978 by NASA/JPL. With the growing need for earth observation, RADARSAT-1, launched in 1995 and declared non-operational in 2013, proved to be an invaluable source for managing resources and monitoring global climate change (Canadian Space Agency [CSA], 2014). The follow-on RADARSAT-2, launched in 2007, enhanced marine surveillance, ice observation, resource management and environment monitoring globally (CSA, 2015). The series of next generation Earth observation missions being planned and currently in orbit, for example, the Sentinel mission of the European Space Agency (ESA) and the upcoming RADARSAT Constellation Mission (RCM) by the CSA, will ensure the continuity of data, and enhance operational use of SAR (ESA, 2017; CSA, 2017). In addition, these missions will not only enhance the traditional Earth observations and applications, but also broaden their use and the development of services (e.g. lake ice monitoring).

The CIS has the responsibility for operational monitoring lake ice, sea ice, and iceberg conditions in Canadian regions and adjacent waters (Arkett et al., 2013). To accomplish this mandate, the CIS primarily relies on visual interpretation of satellite optical and SAR imagery to conduct analyses and prepare products (e.g. ice charts for Laurentian Great Lakes and ice fraction for other large lakes across Canada and the northern U.S.). Due to the advantages of SAR under polar darkness and cloud-covered conditions, fractional ice cover (reported in tenth) from 139

Canadian lakes is currently monitored by CIS using single-pol (HH or VV) and dual-pol (HH+VV or VV+VH) C-band SAR and optical images to meet its responsibilities. Since the performance of single and dual-polarized imagery is limited by the loss of full polarization and phase information, there is a great deal of interest by CIS in using polarimetric SAR for lake and sea ice monitoring. Given the large volume of satellite images already used operationally by CIS and the expected rapid growth of more data from new and upcoming missions, exploring automated image classification of SAR imagery is paramount (Arkett et al., 2013; CIS, 2017). In this thesis, we analyzed the physical scattering mechanisms of lake ice using a quadrature polarimetric RADARSAT-2 dataset obtained over Great Bear Lake, Canada, with the intent of automatically classifying open water and ice cover during the freeze-up and break-up periods.

1.2 Study Objectives

As mentioned above, automated classification of SAR imagery is a research field of high interest for ice cover monitoring. Therefore, the primary goal of this thesis is to analyze polarimetric parameters for ice mapping and to propose a classification method for polarimetric radar imaging to discriminate open water and ice cover. The RADARSAT-2 quadrature polarimetric data was used to achieve the following objectives:

1. Analyze polarimetric parameters in identifying open water and lake ice to improve understanding of lake ice observations.
2. Develop an image classification approach that can segment open water and lake ice from polarimetric parameters.

1.3 Thesis Structure

This manuscript-based thesis is comprised of four chapters which address the objectives identified in Section 1.2. This introductory chapter provides the general context related to the necessity of lake ice monitoring and the remote sensing of lake ice. It identifies the need for automated lake ice classification. Background Chapter 2 provides a review of current SAR research for lake ice mapping and methodologies being used for dual-pol and quad-pol classification. It summarizes the basics of polarized electromagnetic waves, polarimetric radar scatterings, target decompositions, statistical property of polarimetric parameters and classifiers relevant to this study. To addresses the objectives listed above, the manuscript chapter (Chapter 3) implements the Markov Random Field to segment open water and ice from polarimetric parameters. Fourteen RADARSAT-2 polarimetric images are employed to conduct the study for training and testing purposes. The final chapter (Chapter 4) provides a summary of the thesis. It also discusses some of the limitations of the study and identifies possible directions for further research.

The manuscript is included in its own format, containing its own introduction, background, methodology and conclusion sections. This inevitably results in the partial duplication of equations, background material and methodologies from other chapters of the thesis.

2 Background

2.1 Introduction

The research topic of this thesis requires a strong background knowledge in various fields of research. This chapter presents a review of previous lake ice investigations using radar remote sensing, the basic principles of electromagnetic wave and scattering representations, the extraction of polarimetric features, and classification algorithms relevant to this study. Section 2.2 reviews previous studies on lake ice mapping/monitoring using SAR and the current research challenges for lake ice/open water discrimination. The necessity of an automated classification method for lake ice mapping is identified, and previous methodologies for solving the polarimetric classification is presented from physical and mathematical aspects, respectively. Section 2.3 presents the basic principles of monochromatic electromagnetic waves to introduce the basics for understanding the representations of polarization in Section 2.4 and then polarimetric scattering in Section 2.5. Section 2.4 describes the polarization ellipse, which is the basis for the vector-format representation of polarization. The monochromatic plane wave can be represented by Jones vector and Stokes vector, which simulate the status of the polarizations before and after scattering; therefore, the scattering processes or polarization transfer is depicted by the scattering matrix in Section 2.5. Section 2.5 begins with the radar equation that links the power of radar signal and scatterer characteristics. Section 2.6 presents the polarimetric decomposition theorems. The decomposition is developed to separate a scattering process to individual basic scattering mechanisms. Insight into the scattering characteristics can therefore be achieved through polarimetric decomposition. Section 2.7 introduces the statistical properties of polarization intensity and other polarimetric features. The basic principles of the two classifiers: Entropy-alpha Wishart classifier (Lee et al., 2009) and Markov Random Field (MRF), the classifiers employed in this study, are presented in the Section 2.7.4. Finally, Section 2.8 contains a description of RADARSAT-2 and the dataset used in this study. This section also provides the link between the RADARSAT-2 quadrature polarized signals and the theories of polarization descriptors and scattering operators introduced in Sections 2.4 and 2.5, respectively.

2.2 Reviews of Lake Ice Mapping and Classification

The changing ice cover regime of lakes affects local and regional weather/climate as well as aquatic ecosystems and socio-economic activities. As a sensitive indicator of climate change and an important component of lake-atmosphere interactions at high-latitude, lake ice cover needs to be monitored frequently (ideally on a daily basis). Synthetic aperture radar (SAR) has been widely used for lake ice mapping due of its capacity in operating under darkness and in all weather conditions.

The monitoring of ice formation and decay processes and the determination of freeze-up (ice-on) and break-up (ice-off) dates has been the primary focus of most investigations. As mentioned in the introductory chapter, trends and variability in ice dates have been used as climate indicators. The task of mapping and monitoring lake ice during the freeze-up and break-up periods has largely been based on the use of C-band SAR in recent years. For instance, multi-polarized RADARSAT-2 images have been employed to monitor ice cover on shallow Arctic lakes during the break-up period. Methods based on thresholds in backscatter have been used to distinguish melting lake ice from open water (Geldsetzer, van der Sanden & Brisco, 2010). Polarimetric and non-polarimetric parameters retrieved from RADARSAT-2 have been compared for their capacity in identifying ice and open water during the freeze-up period (Geldsetzer & van der Sanden, 2013). Trends in freeze-up and break-up dates have been documented for many lakes across Canada during the second half of the 20th century based on ground-based observations (Duguay et al., 2006). Radar remote sensing is seen as a useful tool that could replace the ever-declining ground-based lake ice observational networks.

Table 2.1 presents a summary of studies that have used SAR imagery to map/monitor ice cover on Canadian lakes. The earlier investigations have utilized SAR to distinguish between floating ice and grounded ice on Arctic and sub-Arctic lakes. The backscatter from lake ice during the initial ice formation (i.e. thin ice) has been reported to be lower than -18 dB (Morris et al., 1995; Duguay et al., 2002). Floating ice on shallow lakes is characterized by high backscatter, which was originally attributed to the double bounce scattering from columnar air inclusions and

ice-water interface, and an increase in volume scattering (Geldsetzer, van der Sanden & Brisco, 2010). However, recent experiments rather support single bounce scattering (surface scattering) at the ice-water interface as the dominant scattering mechanism (Atwood et al., 2015). Low radar return occurs when the ice freezes to the bottom of lakes in the case of shallow lakes (Duguay et al., 2002; Atwood et al., 2015). A significant decrease in backscatter can also be observed during the break-up period due to the microwave absorption by the wet snow and specular reflection from the water or ponds on the ice surface (Duguay et al., 2002; Geldsetzer, van der Sanden & Brisco, 2010). Co-polarized backscattering at a given frequency from open water not only depends on incidence angle, but also relates to the wind speed and wind direction relative to radar looking direction (Geldsetzer & van der Sanden, 2013). However, cross-polarized backscattering is relatively independent of wind direction and incidence angle (Vachon & Wolfe, 2011). Both co-pol and cross-pol backscattering from lake ice are affected by the geometry of ice surface, ice structure, dielectric properties, and incidence angle (Duguay et al., 2002; Geldsetzer & van der Sanden, 2013). Since single and dual-polarized data are limited by their capability to distinguish open water and different ice types (Scheuchl et al., 2004; Geldsetzer & Yackel, 2009), the dual-pol signals combined with polarimetric parameters may increase the potential for ice discrimination (Geldsetzer et al., 2011). C-band polarimetric and non-polarimetric parameters, including sigma naught of individual polarization, co-pol and cross-pol ratio, the co-pol correlation coefficient, entropy, anisotropy and alpha angle have been assessed and summarized for their potential to discriminate lake ice and open water on small, shallow, lakes (Geldsetzer & van der Sanden, 2013). It has been shown that the single-pol VV is preferred when wind speed data is available from a nearby meteorological station and incidence angle is low. The co-pol ratio has been recommended when the incidence angle is larger than 31.2°, and when no wind speed data is available (Geldsetzer & van der Sanden, 2013). Anisotropy has also been shown to be useful when the incidence angle is lower than 27.6°; however, it is insensitive to wind as well (Geldsetzer & van der Sanden, 2013). More recently, as the Canadian RADARSAT Constellation (RCM) and other future missions are planned and launched, more interest has been drawn on compact polarimetry (CP) for (sea) ice classification due to the additional information that CP can provide compared to dual-pol and wider swath widths than quad-pol (Dabboor & Geldsetzer, 2014). However, the necessity of an efficient and automated segmentation or classification of SAR

imagery is still paramount to enhance lake ice monitoring on lakes of all sizes in Canada in view of the operational requirements of weekly lake ice monitoring by the Canadian Ice Service.

Table 2.1: The Summary of Recent Studies of Canadian Lake Ice Mapping Using SAR

Author	Year	Satellite	Methods	Parameters	Content
Duguay et al.	2002	RADARSAT	Backscatter characteristics	HH backscatter	Monitoring ice growth, decay and related processes of shallow sub-Arctic lakes
Duguay & Lafleur	2003	ERS-1 & Landsat TM	Backscatter differences	VV backscatter	Utilizing SAR to determine whether lakes were frozen to bed
Nghiem & Leshkevich	2007	ERS-2, RADARSAT, & Envisat	Backscatter signatures	Co-pol backscatter, co-pol ratio	Mapping ice cover on the Laurentian Great Lakes with ground-based radar and satellite measurements
Geldsetzer, van der Sanden, & Brisco	2010	RADARSAT-2	Backscatter threshold	HH and HV backscatter	Monitoring lake ice during spring melt period on shallow lakes
Geldsetzer van der Sanden, & Drouin	2011	RADARSAT-2	Parameter evaluation	Multi-polarized and polarimetric SAR parameters	Investigating the potential of multi-polarized and polarimetric parameters for monitoring river and lake ice
Geldsetzer & van der Sanden	2013	RADARSAT-2	Decision tree classifier	Single polarized backscatter, co-pol ratio, cross-/co-pol ratio, anisotropy, alpha angle	Monitoring of lake ice during freeze-up period on shallow lakes
Leshkevich & Nghiem	2013	Envisat ASAR, RADARSAT-2	Ice backscatter library	Multi-polarization, quad-pol	Mapping ice cover on the Laurentian Great Lakes with ground-based radar and satellite measurements

The characteristics of scattering mechanisms from ice and open water have been investigated. When the incidence angle is small (lower than 30°), scattering is dominated by surface scattering from open water where water with high relative permittivity has higher co-pol backscatter than ice (Leshkevich & Nghiem, 2013). For large incidence angles, surface scattering is dominant for both open water surface and ice covered area, and volume scattering tends to contribute more from ice (Nghiem & Leshkevich, 2007; Leshkevich & Nghiem, 2013). More specifically, surface scattering mainly comes from the air-ice, air-snow and snow-ice surface (Hossain et al., 2014; Atwood et al., 2015). When the ice surface is smooth enough to be a specular reflector, little or no backscatter can be observed (Cable et al., 2014). Volume scattering is contributed due to the dielectric discontinuities of the medium and geometry of the ice structure (Hossain et al., 2014). Double-bounce scattering occasionally occurs on ice ridges and ice fractures, and it is rarely dominant for the overall scattering compared to surface and volume scattering (Scheuchl, Hajnsek & Cumming, 2002).

The scattering matrix generated from polarimetric signal enables insight into the contributing scattering mechanisms from targets (Atwood et al., 2015), therefore, polarized backscatters have widely been used for ice discrimination and monitoring (Geldsetzer & Yackel, 2009; Leshkevich & Nghiem, 2013; Geldsetzer & van der Sanden, 2013). Due to the distributed nature of targets (introduced later in Section 2.5.5), the target or the environment can be depicted by second order stochastic processes, where the covariance matrix is employed (Lee et al., 1999; Lee & Pottier, 2009). Several studies have been conducted for understanding the scattering mechanisms by decomposing the covariance matrix into second order descriptors corresponding to canonical scatterings or modelled scatterings, which is so called incoherent decomposition (Huynen, 1970; van Zyl; 1989; Cloude & Pottier, 1996; Freeman & Durden, 1998; Yamaguchi, Moriyama, Ishido & Yamada, 2005; Lee, Ainsworth & Wang, 2014). Results from target decompositions are widely used for classification (Cloude & Pottier, 1997; Lee et al., 1999), including sea ice (Scheuchl, Hajnsek & Cumming, 2002; Gill & Yackel, 2012) and lake ice classification (Geldsetzer & van der Sanden, 2013; Leshkevich & Nghiem, 2013). Therefore, the backscatter intensity, covariance matrix and decomposition results are employed for classification in the present thesis.

Ice discrimination is challenging for three reasons. First, the radar signal is sensitive to the geometry and dielectric properties of the objects being sensed, which results in that the object scatters incoherent signals or coherent signals with different polarizations and intensities. Second, the radar signal is easily affected by noise from the environment and the system. Third, different objects may have similar scattering under geometric conditions of illuminations in different locations and incident angles.

There are generally two directions of solving classification problems. The first is to consider the inherent characteristics of the polarimetric features, and classifiers are usually based on the physical scattering mechanisms. Huynen (1970) presented the phenomenological theory to extract the physical properties and the structure of a radar target. The Huynen decomposition theorem aims to separate the Mueller matrix as the sum of a single average target and a residue component called N-target (Cloude & Pottier, 1996; Lee & Pottier, 2009). Cloude (1985) was the first to consider eigen-based decomposition where singular value decomposition was employed. Freeman & Durden (1993) developed the model-based decomposition for physically fitting the three-component scattering model to the covariance matrix or polarimetric observations (Cloude & Pottier, 1996; Freeman & Durden, 1998; Lee & Pottier, 2009). Following from the eigen-based decomposition, Cloude & Pottier (1997) proposed the entropy based classification, extracting average scattering parameters to determine the randomness of the scatters. The second direction is to consider the mathematical modelling, which includes the traditional image processing, probabilities, statistics, and machine learning. Yueh et al. (1988) introduced Bayesian theorem for the complex Gaussian distributed polarimetric returns. Lee et al. (1999) proposed a distance measure of covariance matrix based on complex Wishart distribution. The unsupervised classifier employed the expectation maximization for optimization. Furthermore, Du and Lee (1996) introduced fuzzy set theory into k-means (expectation maximization) clustering algorithm for multi-look polarimetric SAR images to deal with the case where the area covered by a pixel embraces imprecise classes. In recent years, the success of deep learning in the field of computer vision, image/speech recognition has resurrected the use of neural networks. However, Hara et al. (1994), Chen et al. (1996), and Tzeng & Chen (1998) implemented neural networks for polarimetric image classification in the last century. Rignot & Chellappa (1992) proposed an

optimal region labeling model using maximum a posteriori (MAP) estimate, where MAP combined the conditional distribution of polarimetric complex data with a Markov random field for the region labels as prior. Other machine learning methods also show their capabilities on qualitative or quantitative analysis in remote sensing field. Non-probabilistic binary linear classifiers, such as support vector machine, are widely used because they are easy to apply and generalize to testing cases without even considering the statistical and physical properties. When features cannot be linearly separated in lower-dimensional space, mapping variables into higher order spaces, where these features may be linearly separated, is an alternative way to deal with this case. However, the curse of dimensionality may arise from organizing data in high-dimensional spaces. At present, models with cheaper computational operations, for instance, kernel methods, K-nearest neighbors, may be helpful.

2.3 Electromagnetic Wave

This section presents the basic principles of monochromatic electromagnetic waves to provide some basis for understanding the representations of polarization developed in Section 2.4 and then polarimetric scattering in Section 2.5.

2.3.1 Equation of Propagation

The behavior of electromagnetic waves in time and space is governed by the Maxwell equations. They are presented to describe the electromagnetic filed vector and polarization descriptors, which will be used to determine the scattering operator. The Maxwell's equations are given by

$$\begin{aligned} &\text{i.} && \nabla \cdot \boldsymbol{D} = \rho_f \\ &\text{ii.} && \nabla \times \boldsymbol{E} = -\frac{\partial \boldsymbol{B}}{\partial t} \\ &\text{iii.} && \nabla \cdot \boldsymbol{B} = 0 \\ &\text{iv.} && \nabla \times \boldsymbol{H} = \boldsymbol{J} + \frac{\partial \boldsymbol{D}}{\partial t} \end{aligned} \tag{2.1}$$

which are the differential forms with magnetic and polarizable media. The electric field, electric displacement field, magnetic field, and magnetic induction are presented as vector field $\boldsymbol{E}$, $\boldsymbol{D}$, $\boldsymbol{B}$, and $\boldsymbol{H}$, respectively. The total current density $\boldsymbol{J}$ is composed of conduction current density $\boldsymbol{J}_0$ and magnetization current density $\boldsymbol{J}_m$ and polarization current density $\boldsymbol{J}_p$ as follows:

$$\boldsymbol{J} = \boldsymbol{J}_0 + \boldsymbol{J}_m + \boldsymbol{J}_p \tag{2.2}$$

In the following, it is assumed that a monochromatic electromagnetic wave is propagated in a linear medium, free of source (Lee & Pottier, 2009). This assumption implies that magnetization $\boldsymbol{M}$=0, electric polarization $\boldsymbol{P}$=0, the volume charge density $\rho = 0$, and currents related to sources are also zeros ($\boldsymbol{J}_m = 0, \boldsymbol{J}_p = 0$). The differential form of Maxwell's equations (Equation 2.1) in the absence of magnetic and polarizable media can be transformed to

$$\begin{aligned} &\text{i.} && \nabla \cdot \boldsymbol{E} = \frac{\rho}{\varepsilon_0} = 0 \\ &\text{ii.} && \nabla \times \boldsymbol{E} = -\frac{\partial \boldsymbol{B}}{\partial t} \\ &\text{iii.} && \nabla \cdot \boldsymbol{B} = 0 \\ &\text{iv.} && \nabla \times \boldsymbol{B} = \mu_0 \boldsymbol{J_0} + \mu_0 \varepsilon_0 \frac{\partial \boldsymbol{E}}{\partial t} \end{aligned} \tag{2.3}$$

The wave propagation equation is obtained by taking the curl of the curl of electric field

$$\nabla \times (\nabla \times \boldsymbol{E}) = -\frac{\partial}{\partial t}(\nabla \times \boldsymbol{B}) = -\mu_0 \varepsilon_0 \frac{\partial^2 \boldsymbol{E}}{\partial t^2} \tag{2.4}$$

and considering vector identity equation

$$\nabla \times (\nabla \times \boldsymbol{E}) = \nabla(\nabla \cdot \boldsymbol{E}) - \nabla^2 \boldsymbol{E} \tag{2.5}$$

where ∇^2 is the Laplace operator. The Equation 2.4 equals to Equation 2.5, and $\nabla \cdot \boldsymbol{E}$ is zero according to Equation 2.3; therefore, the propagation equation can be presented as

$$\mu_0 \varepsilon_0 \frac{\partial^2 \boldsymbol{E}}{\partial t^2} - \nabla^2 \boldsymbol{E} = 0 \tag{2.6}$$

where $\mu_0 \varepsilon_0 = 1/c^2$.

2.3.2 Monochromatic Plane Wave Solution

Without any loss of generality, the direction of monochromatic wave propagation is defined as **z** in an orthogonal basis {**x**, **y**, **z**}. Since the electric field is dependent only on the spatial variable and temporal variable t, the wave equation in one of space dimensions (**x** and **y**) can be written as follows:

$$\frac{\partial^2 \boldsymbol{E}}{\partial t^2} = \mathrm{c}^2 \frac{\partial^2 \boldsymbol{E}}{\partial z^2} \tag{2.7}$$

In this case, the temporal part of the wave function takes the form of $e^{j\omega t}$, and the spatial part takes the form of $e^{\pm jkz}$, so the total wave equation can be represented by

$$\boldsymbol{E}(\mathrm{z},\mathrm{t}) = \mathrm{A}e^{j(\omega t \pm kz + \varphi)} \tag{2.8}$$

where $c = \omega/k$. Positive and negative z represent wave equations travelling in two opposite directions in **z**. In terms of radar imaging, only one direction in **z** is considered (we take negative z in this case); thus, the electric field can be expressed in a vector from as follows:

$$\boldsymbol{E}(\mathrm{z},\mathrm{t}) = \begin{bmatrix} E_{x0}e^{j(\omega t - kz + \varphi_x)} \\ E_{y0}e^{j(\omega t - kz + \varphi_y)} \end{bmatrix} = \begin{bmatrix} E_{x0}\cos(\omega t - kz + \varphi_x) + jE_{x0}\sin(\omega t - kz + \varphi_x) \\ E_{y0}\cos\big(\omega t - kz + \varphi_y\big) + jE_{y0}\sin\big(\omega t - kz + \varphi_y\big) \end{bmatrix} \tag{2.9}$$

The disturbance (instantaneous amplitude) and phase are recorded by the real and imaginary parts of the radar signal, respectively. They describe a helical trajectory in **z** direction as general elliptic polarization case. Two special cases of polarization can be determined by the difference of phases ($\varphi = \varphi_x - \varphi_y$). Linear polarization occurs when $\varphi = k\pi$; circular polarization occurs when $\varphi = k\pi + \frac{2}{\pi}$. Measuring instantaneous amplitude and phase at four polarizations is a possible way to construct the Stokes vector and scattering matrix (Durden et al., 1989), which will be introduced in Sections 2.3.3 and 2.4.2, respectively.

2.4 Polarization Descriptors

With the knowledge of Maxwell equations and the wave propagation function from section 2.3.1 and 2.3.2, the electric field of monochromatic plane wave in time and space was represented in Equation 2.9. This section focuses on the concepts of polarization representation.

2.4.1 Polarization Ellipse

The polarized ellipse can be represented by three parameters: ellipse amplitude A, ellipse orientation $\phi \in \left[-\frac{\pi}{2},\ \frac{\pi}{2}\right]$, and ellipticity or ellipse aperture $\tau \in \left[\ 0,\ \frac{\pi}{4}\right]$. They can be determined through Equation 2.10 to Equation 2.12 as follows:

$$A = \sqrt{E_{x0}^2 + E_{y0}^2} \tag{2.10}$$

$$\tan 2\phi\ = \frac{2\ E_{x0}\ E_{y0}}{E_{x0}^2 - E_{y0}^2}\cos\varphi \tag{2.11}$$

$$|\sin 2\tau|\ = \frac{2\ E_{x0}\ E_{y0}}{E_{x0}^2 + E_{y0}^2}\ |\sin\varphi| \tag{2.12}$$

2.4.2 Jones Vector

To describe the polarization state of a plane monochromatic electric field, the Jones vector is generally employed. The time-space electric field in Equation 2.9 can be rewritten as

$$\boldsymbol{E}(\mathrm{z} = z_0, \mathrm{t} = t_0) = \begin{bmatrix} E_{x0}e^{j(\omega t - kz + \varphi_x)} \\ E_{y0}e^{j(\omega t - kz + \varphi_y)} \end{bmatrix} = \begin{bmatrix} E_{x0}e^{j\omega t}e^{-jkz}e^{j\varphi_x} \\ E_{y0}e^{j\omega t}e^{-jkz}e^{j\varphi_y} \end{bmatrix} \tag{2.13}$$

To describe the state of wave polarization at a fixed time ($t = t_0$) and a fixed space ($z = z_0$), Jones vector $\boldsymbol{J}$ is defined from Equation 2.10 (Lee & Pottier, 2009)

$$\boldsymbol{J} = \begin{bmatrix} E_{x0}e^{j\varphi_x} \\ E_{y0}e^{j\varphi_y} \end{bmatrix} = Ae^{j\alpha}\begin{bmatrix} \cos\phi & -\sin\phi \\ \sin\phi & \cos\phi \end{bmatrix}\begin{bmatrix} \cos\tau \\ j\sin\tau \end{bmatrix} \tag{2.14}$$

where α is an absolute phase term. The unit Jones vector and its associated orientation and ellipticity for some primary polarizations are presented in Table 2.2.

Table 2.2: The Jones Vectors and the Associated Polarization Ellipse Parameters for Canonical Polarization States

Polarization State	Unit Jones Vector	Orientation	Ellipticity
Horizontal	$\boldsymbol{J} = \begin{bmatrix}1\\0\end{bmatrix}$	0	0
Vertical	$\boldsymbol{J} = \begin{bmatrix}0\\1\end{bmatrix}$	$\frac{\pi}{2}$	0
Linear $\frac{\pi}{4}$	$\boldsymbol{J} = \frac{1}{\sqrt{2}}\begin{bmatrix}1\\1\end{bmatrix}$	$\frac{\pi}{4}$	0
Linear $-\frac{\pi}{4}$	$\boldsymbol{J} = \frac{1}{\sqrt{2}}\begin{bmatrix}1\\-1\end{bmatrix}$	$-\frac{\pi}{4}$	0
Left circular	$\boldsymbol{J} = \frac{1}{\sqrt{2}}\begin{bmatrix}1\\j\end{bmatrix}$		$\frac{\pi}{4}$
Right circular	$\boldsymbol{J} = \frac{1}{\sqrt{2}}\begin{bmatrix}1\\-j\end{bmatrix}$		$-\frac{\pi}{4}$

2.4.3 Stokes Vector

Besides the Jones vector, there is another characterization of polarization states of a plane monochromatic electric field: the Stokes vector. The Jones vector can be obtained through acquiring complex quantities in a coherent radar system. However, in non-coherent radar system, where only power measurement (real quantities of complex signal) is available, the Stokes vector is able to characterize the polarization of a wave (Lee & Pottier, 2009).

As identity matrix $\boldsymbol{I}_2$ introduced in Pauli matrices $\boldsymbol{\sigma}$ as $\boldsymbol{\sigma}_0$:

$$\boldsymbol{\sigma}_0 = \begin{bmatrix}1 & 0\\0 & 1\end{bmatrix}\ \boldsymbol{\sigma}_1 = \begin{bmatrix}1 & 0\\0 & -1\end{bmatrix}\ \boldsymbol{\sigma}_2 = \begin{bmatrix}0 & 1\\1 & 0\end{bmatrix}\ \boldsymbol{\sigma}_3 = \begin{bmatrix}0 & -j\\j & 0\end{bmatrix} \tag{2.15}$$

the product of a Jones vector and its conjugate transpose (a Hermitian matrix shown in Equation 2.16) can be decomposed.

$$\boldsymbol{JJ}^{*T} = \begin{bmatrix} E_x E_x^* & E_x E_y^* \\ E_y E_x^* & E_y E_y^* \end{bmatrix} = \frac{1}{2}(g_0\boldsymbol{\sigma}_0 + g_1\boldsymbol{\sigma}_1 + g_2\boldsymbol{\sigma}_2 + g_3\boldsymbol{\sigma}_3)$$

$$= \frac{1}{2}\begin{bmatrix} g_0 + g_1 & g_2 - jg_3 \\ g_2 + jg_3 & g_0 - g_1 \end{bmatrix} \tag{2.16}$$

Thus the Stokes vector denoted by $\boldsymbol{g}$ is presented:

$$\boldsymbol{g} = \begin{bmatrix} g_0 \\ g_2 \\ g_2 \\ g_3 \end{bmatrix} = \begin{bmatrix} E_x E_x^* + E_y E_y^* \\ E_x E_x^* - E_y E_y^* \\ E_x E_y^* + E_y E_x^* \\ j(E_x E_y^* + E_y E_x^*) \end{bmatrix} = \begin{bmatrix} |E_x|^2 + |E_y|^2 \\ |E_x|^2 - |E_y|^2 \\ 2Re(E_x E_y^*) \\ -2Im(E_x E_y^*) \end{bmatrix}$$

$$= \begin{bmatrix} E_{x0}^2 + E_{y0}^2 \\ E_{x0}^2 - E_{y0}^2 \\ 2E_{x0}^2 E_{y0}^2 \cos\varphi \\ 2E_{x0}^2 E_{y0}^2 \sin\varphi \end{bmatrix} = \begin{bmatrix} A^2 \\ A^2 \cos 2\phi \cos 2\tau \\ A^2 \sin 2\phi \cos 2\tau \\ A^2 \sin 2\tau \end{bmatrix} \tag{2.17}$$

The Stokes parameters characterize the polarization state of a wave, and three wave ellipse parameters (ellipse amplitude A, ellipse orientation ϕ, and ellipticity τ) can be determined from Stokes parameters. The unit Stokes vector and its associated unit Jones vector for some primary polarizations are presented in Table 2.3.

Table 2.3: The Stokes Vectors and the Associated Jones Vectors for Canonical Polarization States

Polarization State	Unit Jones Vector	Unit Stokes Vector
Horizontal	$\boldsymbol{J} = \begin{bmatrix} 1 \\ 0 \end{bmatrix}$	$\boldsymbol{g} = \begin{bmatrix} 1 \\ 1 \\ 0 \\ 0 \end{bmatrix}$
Vertical	$\boldsymbol{J} = \begin{bmatrix} 0 \\ 1 \end{bmatrix}$	$\boldsymbol{g} = \begin{bmatrix} 1 \\ -1 \\ 0 \\ 0 \end{bmatrix}$
Linear $\frac{\pi}{4}$	$\boldsymbol{J} = \frac{1}{\sqrt{2}}\begin{bmatrix} 1 \\ 1 \end{bmatrix}$	$\boldsymbol{g} = \begin{bmatrix} 1 \\ 0 \\ 1 \\ 0 \end{bmatrix}$
Linear $-\frac{\pi}{4}$	$\boldsymbol{J} = \frac{1}{\sqrt{2}}\begin{bmatrix} 1 \\ -1 \end{bmatrix}$	$\boldsymbol{g} = \begin{bmatrix} 1 \\ 0 \\ -1 \\ 0 \end{bmatrix}$
Left circular	$\boldsymbol{J} = \frac{1}{\sqrt{2}}\begin{bmatrix} 1 \\ j \end{bmatrix}$	$\boldsymbol{g} = \begin{bmatrix} 1 \\ 0 \\ 0 \\ 1 \end{bmatrix}$
Right circular	$\boldsymbol{J} = \frac{1}{\sqrt{2}}\begin{bmatrix} 1 \\ -j \end{bmatrix}$	$\boldsymbol{g} = \begin{bmatrix} 1 \\ 0 \\ 0 \\ -1 \end{bmatrix}$

2.5 Scattering Operator

With polarization of the wave represented by Jones vector or Stokes vector, the scattering processes can be described by transforming the status of polarizations before and after the scattering. This section begins with the radar equation that links the power of radar signal and the characteristics of scatterers, and then describes the scattering representations including scattering matrix and second-order covariance matrix.

2.5.1 Radar Equation

An electromagnetic wave may reach an object or a target and interact with it. The interaction may result in scattering (reflecting), transmitting, energy absorbing, and reradiating. The problems arising from the wave interaction with objects raise the necessity to characterize the scatters. In a case where the radar footprint is larger than the size of an object, the scatters are fully viewed within the footprint, and it can be characterized by a single radar cross section σ. When the radar footprint is smaller than the size of an object, the object will be characterized through considering its extent and determining the averaged radar cross section over a unit area, the so-called scattering coefficient σ^0. Changes in power are fundamental as the result of wave interaction with objects, they can be described by the radar equation in a monostatic radar system as follows:

$$P_R = \frac{P_T G_T}{4\pi r^2} \sigma \frac{A_e}{4\pi r^2} \tag{2.18}$$

where P_R is the power detected at the receiver, the peak transmitted power from radar is denoted as P_T, antenna gain as G_T, and the effective aperture of the receiver as A_e.

Since it is assumed that an isotropic radiator emits equal radiation in all directions and waves propagate in an ideal condition of linear medium and free of source, power density S at a distance r away from radiator can be expressed as

$$S = \frac{P}{4\pi r^2} \tag{2.19}$$

If the radiated power is redirected by radar antennas, it results in a redistribution (an increase) of the power density in direction of the propagation. This process is characterized by the antenna gain G. The antenna gain is related with antenna effective aperture A_e through

$$A_e = \frac{G\lambda^2}{4\pi} \tag{2.20}$$

The peak transmitted power from a radar is denoted as P_T, then the power density at incident point of the target using a directive antenna is given as

$$S_i = \frac{P_T G_T}{4\pi r^2} \tag{2.21}$$

The scattered power at the target is denoted as P_s; thus the scattered power density S_r seen from the radar, a distance r away from the target, can be simply represented by

$$S_r = \frac{P_s}{4\pi r^2} \tag{2.22}$$

The total power P_R received by an effective antenna area is

$$P_R = S_r A_e \tag{2.23}$$

The radar cross section σ is an area (m^2) defined as the ratio of backscatter density of reflecting signals in the direction of the receiver:

$$\sigma = \frac{P_s}{S_i} = 4\pi r^2 \frac{S_r}{S_i} = 4\pi r^2 \frac{|E_s|^2}{|E_i|^2} \tag{2.24}$$

As mentioned above, when the target is larger than the radar footprint, the scattering coefficient should be employed to model the target characteristics. The total power reviewed from the target is integrated in an illuminated area A_0 in a monostatic radar system:

$$P_R = \iint_{A_0} \frac{P_T G_T}{4\pi r^2} \sigma^0 \frac{A_e}{4\pi r^2}\, ds \tag{2.25}$$

The scattering coefficient σ^0, the averaged radar cross section over unit area, is a dimensionless parameter, which is different from radar cross section σ (unit: m^2). The relationship of these can be expressed as:

$$\sigma^0 = \frac{\sigma}{A_0} = \frac{4\pi r^2}{A_0}\frac{S_r}{S_i} = \frac{4\pi r^2}{A_0}\frac{|E_s|^2}{|E_i|^2} \tag{2.26}$$

2.5.2 Scattering Matrix

Since the polarization of a plane monochromatic electric field can be described by the Jones vector, given $\boldsymbol{J}_i, \boldsymbol{J}_s$ of the incident and scattered wave, respectively, the scattering can be depicted in the local coordinate system as follows:

$$\boldsymbol{J}_s = \frac{e^{-jkr}}{r}\boldsymbol{S}\,\boldsymbol{J}_i = \frac{e^{-jkr}}{r}\begin{bmatrix}\mathrm{S}_{XX} & \mathrm{S}_{XY}\\ \mathrm{S}_{YX} & \mathrm{S}_{YY}\end{bmatrix}\boldsymbol{J}_i = \frac{e^{-jkr}}{r}\begin{bmatrix}\mathrm{S}_{XX} & \mathrm{S}_{XY}\\ \mathrm{S}_{YX} & \mathrm{S}_{YY}\end{bmatrix}\begin{bmatrix}J_{Xi}\\ J_{Yi}\end{bmatrix} \tag{2.27}$$

where the $\boldsymbol{S}$ is defined as scattering matrix, and the S_{ij} is complex scattering coefficient. The diagonal elements and off-elements of $\boldsymbol{S}$ are called co-polar and cross-polar, respectively. The term $\frac{e^{-jkr}}{r}$ addresses the propagation process r away from the target to the receiving antenna. In a monostatic radar system, the scattering matrix $\boldsymbol{S}$ is named the Sinclair $\boldsymbol{S}$ matrix (Lee & Pottier, 2009). By considering Equation 2.24, the radar cross section can be relevant to the elements in the scattering matrix as

$$\sigma = 4\pi|S|^2 \tag{2.28}$$

In the following discussions, the polarizations are defined in the backscatter alignment (BSA) convention in a monostatic coordinate system. The Sinclair matrix described with quadrature polarization in linear horizontal and vertical bases can be expressed as

$$\boldsymbol{S} = \begin{bmatrix}\mathrm{S}_{HH} & \mathrm{S}_{HV}\\ \mathrm{S}_{VH} & \mathrm{S}_{VV}\end{bmatrix} \tag{2.29}$$

The reciprocity theorem in this monostatic backscattering case constrains the Sinclair matrix to be symmetrical, where $\mathrm{S}_{XY} = \mathrm{S}_{YX}$ (Lee & Pottier, 2009).

2.5.3 Scattering Vector

For further interpretation of target characteristics, the Sinclair matrix $\boldsymbol{S}$ can be converted to target vectors as follows:

$$\boldsymbol{k} = \mathrm{Trace}(\boldsymbol{S}\boldsymbol{\psi}) \tag{2.30}$$

where $\boldsymbol{\psi}$ is basis matrices. Two popular basis sets, lexicographic basis matrix set and Pauli spin matrix set, as introduced in Equation 2.15, are employed in this thesis

$$\{\boldsymbol{\psi}_L\} = \{\begin{bmatrix}1 & 0\\ 0 & 0\end{bmatrix} \begin{bmatrix}0 & 1\\ 0 & 0\end{bmatrix} \begin{bmatrix}0 & 0\\ 1 & 0\end{bmatrix} \begin{bmatrix}0 & 0\\ 0 & 1\end{bmatrix}\} \tag{2.31}$$

$$\{\boldsymbol{\psi}_P\} = \{\begin{bmatrix}1 & 0\\ 0 & 1\end{bmatrix} \begin{bmatrix}1 & 0\\ 0 & -1\end{bmatrix} \begin{bmatrix}0 & 1\\ 1 & 0\end{bmatrix} \begin{bmatrix}0 & -\mathrm{j}\\ \mathrm{j} & 0\end{bmatrix}\} \tag{2.32}$$

As mentioned above, the reciprocity theorem constrains the cross-polar to be the same, therefore the basis matrices can be reduced from four bases in Equation 2.31 and Equation 2.32 to three bases as follow (Lee & Pottier, 2009):

$$\{\boldsymbol{\psi}_L\} = \{\begin{bmatrix}1 & 0\\ 0 & 0\end{bmatrix} \sqrt{2}\begin{bmatrix}0 & 1\\ 0 & 0\end{bmatrix} \begin{bmatrix}0 & 0\\ 0 & 1\end{bmatrix}\} \tag{2.33}$$

$$\{\boldsymbol{\psi}_P\} = \{\begin{bmatrix}1 & 0\\ 0 & 1\end{bmatrix} \begin{bmatrix}1 & 1\\ 0 & -1\end{bmatrix} \begin{bmatrix}0 & 1\\ 1 & 0\end{bmatrix}\} \tag{2.34}$$

Their corresponding scattering vectors are

$$\boldsymbol{k}_L = \begin{bmatrix}\mathrm{S}_{HH} & \sqrt{2}\mathrm{S}_{HV} & 2\mathrm{S}_{VV}\end{bmatrix}^T \tag{2.35}$$

$$\boldsymbol{k}_P = \frac{\sqrt{2}}{2}[\mathrm{S}_{HH} + \mathrm{S}_{VV} \quad \mathrm{S}_{HH} - \mathrm{S}_{VV} \quad 2\mathrm{S}_{HV}]^T \tag{2.36}$$

The purpose of adding the factors in the bases sets is to keep total power of scattering consistent; therefore,

$$\mathrm{Span}(\boldsymbol{S}) = \mathrm{Trace}(\boldsymbol{S}\boldsymbol{S}^{*T}) = |\boldsymbol{k}_L|^2 = |\boldsymbol{k}_P|^2 = |\mathrm{S}_{HH}|^2 + 2|\mathrm{S}_{HV}|^2 + |\mathrm{S}_{VV}|^2 \tag{2.37}$$

2.5.4 Polarimetric Parameters

The complex correlation coefficients between polarizations are important effects on statistical distribution of the phase difference and polarization ratio. Those parameters can be discriminators for recognition and further estimations.

The total power of scattering $\mathrm{Span}(\boldsymbol{S})$ is provided in Equation 2.37. The co-polarization ratio r_{co} and cross-polarization ratios r_{cross} can be calculated through

$$r_{co} = \frac{|S_{HH}S_{HH}^*|}{|S_{VV}S_{VV}^*|} \tag{2.38}$$

$$r_{cross} = \frac{|S_{HV}S_{HV}^*|}{|S_{HH}S_{HH}^*|} \quad \text{or} \quad \frac{|S_{HV}S_{HV}^*|}{|S_{VV}S_{VV}^*|} \tag{2.39}$$

The depolarization Ratio r_{depol} is represented by

$$r_{depol} = \frac{2S_{hv}S_{hv}^*}{S_{hh}S_{hh}^* + S_{vv}S_{vv}^*} \tag{2.40}$$

Co-polarization phase difference ϕ can be represented by

$$\phi = \mathrm{Arg}(S_{HH}S_{VV}^*) = tan^{-1}\left[\frac{Im\langle S_{HH}S_{VV}^*\rangle}{Re\langle S_{HH}S_{VV}^*\rangle}\right] \tag{2.41}$$

Co-polarized correlation coefficient ρ can be calculated by

$$\rho = \frac{|S_{HH}S_{VV}^*|}{\sqrt{|S_{HH}S_{HH}^*||S_{VV}S_{VV}^*|}} \tag{2.42}$$

2.5.5 Covariance Matrix and Coherency Matrix

The signals received by a radar may be averaged or integrated scattering from various single targets, which are called distributed radar targets or distributed scatters. The scatters may not be stationary or fixed, subject to spatial and temporal variations in a dynamically changing environment, and the radar itself is also moving with respect to the illuminated area (Lee & Pottier, 2009). All the above circumstances may result in incoherent and partial-polarized wave received by radar. Due to the presence of speckle noises, it will also be an incoherent case once speckle filtering has been applied. Since the coherent scattering matrix $\boldsymbol{S}$ is able to characterize only the

coherent or pure scatterers, incoherent averaged covariance matrix and coherency matrix are introduced to statistically analyze stochastic processes more precisely. These two representations are equivalent to each other.

The covariance $\boldsymbol{C}$ matrix or coherency $\boldsymbol{T}$ matrix are formed from the outer product of the target vector and its conjugate transpose:

$$\boldsymbol{C} = \boldsymbol{k}_L \boldsymbol{k}_L{}^{*T} \tag{2.43}$$

$$\boldsymbol{T} = \boldsymbol{k}_P \boldsymbol{k}_P{}^{*T} \tag{2.44}$$

where the size of both covariance and coherency matrix is 3 by 3. Since $\boldsymbol{k}_L$ and $\boldsymbol{k}_P$ can be transformed to each other through unitary transformation matrix

$$\boldsymbol{k}_P = \boldsymbol{U}_{L-P} \boldsymbol{k}_L \tag{2.45}$$

where

$$\boldsymbol{U}_{L-P} = \frac{\sqrt{2}}{2} \begin{bmatrix} 1 & 0 & 1 \\ 1 & 0 & -1 \\ 0 & \sqrt{2} & 0 \end{bmatrix} \tag{2.46}$$

The covariance $\boldsymbol{C}$ matrix and coherency $\boldsymbol{T}$ matrix can also be transformed as

$$\boldsymbol{T} = \boldsymbol{U}_{L-P} \boldsymbol{C} \boldsymbol{U}_{L-P}^{-1} \tag{2.47}$$

2.6 Target Decomposition

The scattering operators introduced in Section 2.5 can be used to describe the scattering processes or polarization transfer. However, the insights of the scattering characteristics have not been interpreted. The target decomposition aims to find a statistical description that represents the scattering processes through a combination of scattering effects and noise (Lee & Pottier, 2009).

Polarimetric decomposition theorems are categorised into coherent and incoherent target decompositions. Coherent decomposition is based on the scattering matrix, which is expressed as a combination of canonical scattering matrices

$$\boldsymbol{S} = \sum_{k=1}^{K} \omega_k \boldsymbol{S}_k \tag{2.48}$$

Since the scattering matrix can characterize only the scattering process with both incident and scattered wave fully polarized, the coherent decompositions can decompose only the coherent targets (single or pure scatters) with coherent scattering. In this case, coherent decompositions ignore the disturbing environment and speckle noise associated with single-look data. To solve the noise influence, speckle filters more or less average the data, which leads us to a condition of using the covariance $\boldsymbol{C}$ matrix or coherency $\boldsymbol{T}$.

Incoherent decomposition is based on the incoherently averaged covariance or coherency matrices. The objective is to decompose the covariance matrix and coherency matrix into the second order descriptors corresponding to canonical scattering. The covariance $\boldsymbol{C}$ matrix and coherency $\boldsymbol{T}$ are most important observable measurements that account for local variations over the scattering matrix.

2.6.1 Pauli Decomposition

The Pauli decomposition expresses the scattering S matrix as the complex sum of the Pauli matrices as introduced in Equation 2.32. Thus, the canonical scattering mechanisms are associated with each basis matrix in the Pauli spin matrices as

$$\boldsymbol{S} = \begin{bmatrix} S_{HH} & S_{HV} \\ S_{VH} & S_{VV} \end{bmatrix} = \frac{a}{\sqrt{2}} \begin{bmatrix} 1 & 0 \\ 0 & 1 \end{bmatrix} + \frac{b}{\sqrt{2}} \begin{bmatrix} 1 & 0 \\ 0 & -1 \end{bmatrix} + \frac{c}{\sqrt{2}} \begin{bmatrix} 0 & 1 \\ 1 & 0 \end{bmatrix} + \frac{d}{\sqrt{2}} \begin{bmatrix} 0 & -\mathrm{j} \\ \mathrm{j} & 0 \end{bmatrix} \tag{2.49}$$

Those four components a, b, c, d are considered as follows: single scattering from a plane surface (single or odd bounce scattering), diplane scattering (double or even-bounce scattering) with relative orientation of 0°, diplane scattering with relative orientation of 45°, and antisymmetric components of the scattering $\boldsymbol{S}$ matrix (Lee & Pottier, 2009). The reciprocity theorem in the monostatic backscattering case results in $d = 0$. Therefore, the total power (Span) is given by

$$\mathrm{Span}(\boldsymbol{S}) = |\mathrm{S}_{HH}|^2 + 2|\mathrm{S}_{HV}|^2 + |\mathrm{S}_{VV}|^2 = |a|^2 + |b|^2 + |c|^2 \tag{2.50}$$

The scattering mechanisms which are not visible with the linear lexicographic basis can be enhanced through transformation of basis from linear to Pauli for a clear representation. The Pauli basis is therefore defined as the sum and difference of co-pol, and the sum of cross-pol in Equation 2.49. The first two elements in Pauli scattering vector represent the scattering from a trihedral or odd-bounce reflector for $\mathrm{S}_{HH} + \mathrm{S}_{VV}$, and from a dihedral or even-bounce reflector for $\mathrm{S}_{HH} - \mathrm{S}_{VV}$ (Van Zyl & Kim, 2010). The last term $2\mathrm{S}_{HV}$ occupies the cross-polarized components of the scattering; from a theoretical view, it represents the scattering from a dihedral reflector rotated by 45 degree (Van Zyl & Kim, 2010). In practise, cross-pol components are typically derived from a depolarization of the scattering; since this term involves only the cross-pol, it can be interpreted as random scattering in most circumstances.

The trihedral scattering characterizes the mechanisms where no cross-polarization components occur, co-polarized components are identical, and co-polarization components are in phase. The characteristics for a dihedral reflector are that no cross-polarized components are generated in a linear radar signal (horizontal or vertical) and co-pol components are identical but out of phase. A dihedral reflector rotated by 45 degrees results in cross pol components reaching the maximum, with no corresponding co-pol components.

2.6.2 Eigen Decomposition

The singular value decomposition factorize an $m \times n$ complex matrix $\boldsymbol{M}$ into a form of $\boldsymbol{U\Sigma V^{*T}}$, where $\boldsymbol{U}$ is an $m \times m$ unitary matrix; $\boldsymbol{\Sigma}$ is an $m \times n$ diagonal matrix with non-negative real numbers, and $\mathbf{V}$ is an $n \times n$ unitary matrix. Since the covariance $\boldsymbol{C}$ matrix or coherency $\boldsymbol{T}$ matrix are positive semi-definite matrices, and they are also Hermitian matrices, the coherency $\boldsymbol{T}$ matrix can be factorized as

$$\boldsymbol{T} = \boldsymbol{U\Sigma U^{*T}} = \boldsymbol{U\Sigma U^{-1}} \tag{2.51}$$

where $\boldsymbol{\Sigma}$ is a 3×3 diagonal nonnegative real eigenvalue matrix with $\lambda_1 \geq \lambda_2 \geq \lambda_3 \geq 0$, $\mathbf{U} = [\boldsymbol{u_1}\ \boldsymbol{u_2}\ \boldsymbol{u_3}]$ is a 3×3 unitary matrix. The $\boldsymbol{u_1}$, $\boldsymbol{u_2}$, and $\boldsymbol{u_3}$ are unit eigenvector orthogonal to each other. In this case, the coherency matrix can be decomposed into the sum of three independent scattering mechanisms. The contribution from the scattering mechanism is determined by the corresponding eigenvalue λ_i of the related unitary eigenvector $\boldsymbol{u_i}$. The Eigen decomposition can be written as

$$\boldsymbol{T} = \sum_{\boldsymbol{i=1}}^{\boldsymbol{3}} \lambda_i \boldsymbol{u_i u_i}^{*T} \tag{2.52}$$

If only one eigenvalue is nonzero, the scattering is related to a single scattering matrix from a pure target. If all the eigenvalues are equal, three orthogonal scattering mechanisms are included equally. The target is randomly distributed. The eigenvectors $\boldsymbol{u_i}$ can be formulated as (Cloude & Pottier, 1996)

$$\boldsymbol{u_i} = e^{j\phi_i} \begin{bmatrix} \cos\alpha_i \\ \sin\alpha_i \cos\beta_i\, e^{j\delta_i} \\ \sin\alpha_i \cos\beta_i\, e^{j\gamma_i} \end{bmatrix} \tag{2.53}$$

where α angle corresponds to the variation from surface scattering ($\alpha = 0°$) to randomly oriented dipole scattering ($\alpha = 45°$), and to double bounce scattering ($\alpha = 90°$). The β angle is the twice that of the polarization orientation angle. The δ angle is the phase difference between $S_{HH} + S_{VV}$ and $S_{HH} - S_{VV}$, the γ angle is the phase difference between $S_{HH} + S_{VV}$ and S_{HV}, and the ϕ angle is physically equivalent to target absolute phase $S_{HH} + S_{VV}$ (Lee et al., 1999).

2.6.3 Entropy-Alpha Decomposition

Cloude eigenvector decomposition is mathematically unique; however, its interpretation is not necessarily straightforward, because the eigenvectors are not guaranteed to represent known physical scattering mechanisms directly (van Zyl & Kim, 2010). In this case, the coordinate systems generated from the eigenvectors vary from pixel to pixel. Fortunately, a statistical model over the scatterer can be built as the sum of three eigenvectors with their corresponding contributions (eigenvalues) in Equation 2.52.

The averaged alpha angle $\bar{\alpha}$, directly related to three eigenvectors, can identify the dominant scattering mechanisms, which relies on the mean of α, which is defined as

$$\bar{\alpha} = \sum_{i=1}^{3} P_i \alpha_i \tag{2.56}$$

As introduced in 2.5.2, α angle varies from surface scattering to dipole scattering and to double bounce scattering. The $\bar{\alpha}$ is the averaged scattering mechanisms obtained by considering the contributions of each independent scattering.

The contribution from each eigenvector can be represented by the probability P_i, which given by

$$P_i = \frac{\lambda_i}{\sum_{j=1}^{3} \lambda_j} \tag{2.54}$$

In order to define the degree of statistical disorder of each distinct scatterer, the polarimetric entropy H is expressed by

$$H = -\sum_{i=1}^{3} P_i log_3(P_i) \tag{2.55}$$

The entropy ranges from 0 to 1. It represents the disorder of the scatterer from weakly depolarized isotropic ($H = 0$) to totally depolarized random scattering ($H = 1$). The Figure 2.1 suggests discrete distributions of entropy based on three contributions or pseudo probabilities P_i. When the scattering system is dominated by a single scattering, the entropy is relatively lower. If the system is highly depolarized or mixed with distinct scatterings, the entropy is relatively higher.

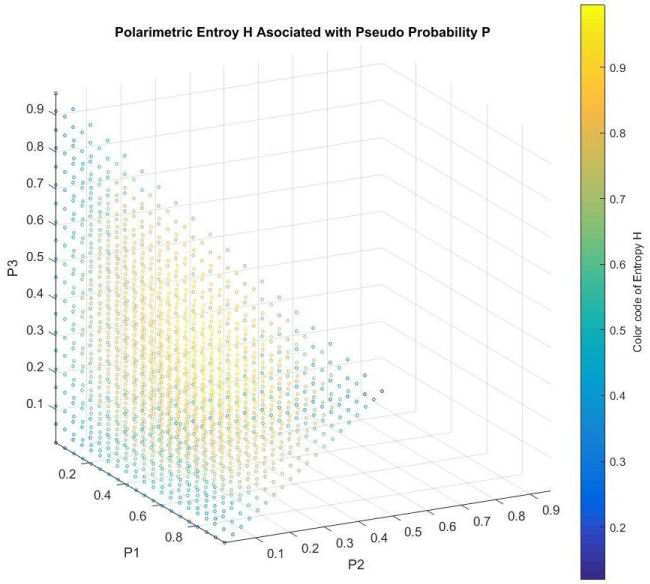

Figure 2.1: Discrete distributions of entropy based on three contributions or pseudo probabilities P_i. When the scattering system is dominated by a single scattering, the entropy is relatively lower. If the system is highly depolarized or mixed with multiple scatterings, the entropy is relatively higher.

2.6.4 Freeman-Durden Decomposition

A limitation of Eigen decomposition and the dichotomy of Kennaugh matrix is that they highly rely on mathematical methods instead of modeling the physical scatterings. Freeman & Durden (1993) proposed a three-component scattering mechanism model to estimate the contribution to the total backscatter from Bragg surface scatter, randomly oriented dipoles (volume), and even-bounce scattering mechanism. The volume scattering is an incoherent scattering model, while both of the surface scattering and the double-bounce scattering are coherent in nature (Lee, Thomas & Yanting, 2014).

The original idea behind the Freeman-Durden decomposition is to hypothesize that the covariance matrix can be decomposed into the combinations of predicted scattering covariance matrices, where the scattering mechanism of random oriented branches is modeled as volume scattering, the dihedral structure as double-bounce scattering, and the surface scattering

$$\boldsymbol{T} = \begin{bmatrix} T_{11} & T_{12} & T_{13} \\ T_{21} & T_{22} & T_{23} \\ T_{31} & T_{32} & T_{33} \end{bmatrix} = m_S \begin{bmatrix} 1 & \beta^* & 0 \\ \beta & |\beta|^2 & 0 \\ 0 & 0 & 0 \end{bmatrix} + m_D \begin{bmatrix} |\alpha|^2 & \alpha & 0 \\ \alpha^* & 1 & 0 \\ 0 & 0 & 0 \end{bmatrix} + m_V \begin{bmatrix} 2 & 0 & 0 \\ 0 & 1 & 0 \\ 0 & 0 & 1 \end{bmatrix} \tag{3.21}$$

The first component of the Freeman-Durden decomposition models the scattering from first-order Bragg scatter with a moderately rough surface. In this case, the cross-pol can be negligible. The scattering matrix for this component can be represented by

$$\boldsymbol{S_s} = \begin{bmatrix} \mathrm{R}_H & 0 \\ 0 & \mathrm{R}_V \end{bmatrix} \tag{2.57}$$

where R_H and R_V are associated with local incidence angle and the relative dielectric constant of the surface. The corresponding covariance matrix $\boldsymbol{C_s}$ of $\boldsymbol{S_s}$ can be represented as

$$\boldsymbol{C_s} = \begin{bmatrix} |\mathrm{R}_H|^2 & 0 & \mathrm{R}_H \mathrm{R}_V{}^* \\ 0 & 0 & 0 \\ \mathrm{R}_V \mathrm{R}_H{}^* & 0 & |\mathrm{R}_V|^2 \end{bmatrix} = f_S \begin{bmatrix} |\beta|^2 & 0 & \beta \\ 0 & 0 & 0 \\ \beta^* & 0 & 1 \end{bmatrix} \tag{2.58}$$

where $f_S = |\mathrm{R}_V|^2$ corresponds to the contribution of the odd-bounce scattering to the $|\mathrm{S}_{VV}|^2$, and $\beta = \mathrm{R}_H/\mathrm{R}_V$.

Double-bounce scattering is modeled by scattering from a dihedral reflector. The double-bounce scatterings are contributed mainly from ice ridges and ice fragments (Hossain et al., 2014). Recall Freeman & Durden's (1993) descriptions of this model: The reflection coefficients for horizontal surface are R_{GH} and R_{GV} for horizontal and vertical polarizations, respectively. The reflection coefficients for vertical surface are R_{TH} and R_{TV} for horizontal and vertical polarizations, respectively. The propagation term $e^{j2\gamma}$ models the intensity attenuation and phase changes along

the propagation. The cross-pol components are also negligible in this case. Thus, the scattering model of double-bounce is given by

$$\boldsymbol{S_D} = \begin{bmatrix} e^{j2\gamma_h}\mathrm{R}_{TH}\mathrm{R}_{GH} & 0 \\ 0 & e^{j2\gamma_v}\mathrm{R}_{TV}\mathrm{R}_{GV} \end{bmatrix} \tag{2.59}$$

It yields the corresponding covariance matrix $\boldsymbol{C_D}$

$$\boldsymbol{C_D} = \begin{bmatrix} |\mathrm{R}_{TH}\mathrm{R}_{GH}|^2 & 0 & e^{j2(\gamma_h-\gamma_v)}\mathrm{R}_{TH}\mathrm{R}_{GH}{\mathrm{R}_{TV}}^*{\mathrm{R}_{GV}}^* \\ 0 & 0 & 0 \\ e^{j2(\gamma_v-\gamma_h)}\mathrm{R}_{TV}\mathrm{R}_{GV}{\mathrm{R}_{TH}}^*{\mathrm{R}_{GH}}^* & 0 & |\mathrm{R}_{TV}\mathrm{R}_{GV}|^2 \end{bmatrix}$$

$$= f_D \begin{bmatrix} |\alpha|^2 & 0 & \alpha \\ 0 & 0 & 0 \\ \alpha^* & 0 & 1 \end{bmatrix} \tag{2.60}$$

where $f_D = |\mathrm{R}_{TV}\mathrm{R}_{GV}|^2$ represents the contribution of the even-bounce scattering to the $|\mathrm{S}_{VV}|^2$, and

$$\alpha = e^{j2(\gamma_h-\gamma_v)}\frac{\mathrm{R}_{TH}\mathrm{R}_{GH}}{\mathrm{R}_{TV}\mathrm{R}_{GV}} \tag{2.61}$$

The volume scattering is modeled as radar returns from a cloud of randomly oriented dipoles. The scattering matrix of a horizontally oriented dipole can be expressed by

$$\boldsymbol{S_{dipole}} = \begin{bmatrix} \mathrm{a} & 0 \\ 0 & \mathrm{b} \end{bmatrix} \tag{2.62}$$

where a and b are complex scattering coefficients, and a $\gg$ b. We simply rotate the horizontal dipole an angle θ, thus the scattering matrix of θ oriented can be derived from

$$\boldsymbol{S}(\theta) = \begin{bmatrix} \cos\theta & \sin\theta \\ -\sin\theta & \cos\theta \end{bmatrix} \boldsymbol{S_{dipole}} \begin{bmatrix} \cos\theta & -\sin\theta \\ \sin\theta & \cos\theta \end{bmatrix}$$

$$= \begin{bmatrix} a\cos^2\theta + b\sin^2\theta & (b-a)\sin\theta\cos\theta \\ (b-a)\sin\theta\cos\theta & a\sin^2\theta + b\cos^2\theta \end{bmatrix} \tag{2.63}$$

where the cross-pol components are the same. Since the volume scattering counts a mixture of scattering from randomly oriented dipoles, the second order covariance matrix $\boldsymbol{C_V}$ can be represented by

$$|\mathrm{S}_{HH}|^2 = |\mathrm{a}|^2 I_1 + |\mathrm{b}|^2 I_2 + 2Real(ab^*)I_4$$

$$|S_{VV}|^2 = |a|^2 I_2 + |b|^2 I_1 + 2Real(ab^*) I_4$$

$$|S_{HV}|^2 = |b - a|^2 I_4$$

$$S_{HH} S_{HV}^* = (b - a)^* (a I_5 + b I_6)$$

$$S_{HH} S_{VV}^* = (|a|^2 + |b|^2) I_4 + ab^* I_1 + ba^* I_2$$

$$S_{HV} S_{VV}^* = (b - a)(a^* I_6 + b^* I_5) \quad (2.64)$$

where

$$I_1 = \int_0^{2\pi} \cos^4 \theta \, d\theta = \frac{3\pi}{4}$$

$$I_2 = \int_0^{2\pi} \sin^4 \theta \, d\theta = \frac{3\pi}{4}$$

$$I_3 = \int_0^{2\pi} \sin^2 2\theta \, d\theta = \pi$$

$$I_4 = \int_0^{2\pi} \sin^2 \theta \cos^2 \theta \, d\theta = \frac{\pi}{4}$$

$$I_5 = \int_0^{2\pi} \cos^3 \theta \sin \theta \, d\theta = 0$$

$$I_6 = \int_0^{2\pi} \sin^3 \theta \cos \theta \, d\theta = 0 \quad (2.65)$$

We assume the orientation angles are uniform, which results

$$|S_{HH}|^2 = \frac{3\pi}{4}(|a|^2 + |b|^2) + \frac{\pi}{4} \cdot 2Real(ab^*)$$

$$|S_{VV}|^2 = \frac{3\pi}{4}(|a|^2 + |b|^2) + \frac{\pi}{4} \cdot 2Real(ab^*)$$

$$|S_{HV}|^2 = \frac{\pi}{4}|b - a|^2$$

$$S_{HH} S_{HV}^* = 0$$

$$S_{HH} S_{VV}^* = \frac{\pi}{4}(|a|^2 + |b|^2) + \frac{3\pi}{4} ab^* + \frac{3\pi}{4} ba^*$$

$$S_{HV} S_{VV}^* = 0 \quad (2.66)$$

Since we consider the scatter to be thin cylinder-like scatterers, which result in a $\gg$ b $\rightarrow$ 0, the Covariance matrix $\boldsymbol{C_V}$ is given by:

$$\boldsymbol{C_V} = \frac{\pi}{4}|\mathrm{a}|^2 \begin{bmatrix} 3 & 0 & 1 \\ 0 & 2 & 0 \\ 1 & 0 & 3 \end{bmatrix} = f_V \begin{bmatrix} 3 & 0 & 1 \\ 0 & 2 & 0 \\ 1 & 0 & 3 \end{bmatrix} \tag{2.67}$$

Hence, the covariance matrix $\boldsymbol{C}$ can be given by the sum of corresponding covariance matrix of surface, double-bounce and volume scattering:

$$\boldsymbol{C} = \begin{bmatrix} |\beta|^2 f_S + |\alpha|^2 f_D + 3f_V & 0 & \beta f_S + \alpha f_D + f_V \\ 0 & 2f_V & 0 \\ \beta^* f_S + \alpha^* f_D + f_V & 0 & f_S + f_D + 3f_V \end{bmatrix} \tag{2.68}$$

The next step is to estimate the three parameters: f_S, f_D, and f_V. It is easy to determine the value of f_V from the $2|\mathrm{S}_{HV}|^2$, and f_S and f_D should be positive real values since they are proportional to the contribution of surface and double bounce scattering. Since β is the ratio of horizontal to vertical polarized reflection coefficient for surface scattering, there should be no phase difference between HH and VV returns, so theoretically β is a positive real value; however, in practice, β remains to be a complex number when α has been fixed. There are various ways to fix the value of α and β or to add a relation function between α and β. Van Zyl (1989) determined the dominant contribution from the real part of $\mathrm{S}_{HH}\mathrm{S}_{VV}{}^*$. If $Real(\mathrm{S}_{HH}\mathrm{S}_{VV}{}^*) \geq 0$, the scattering is dominated by surface scattering, and $\alpha = -1$ is fixed; otherwise if $Real(\mathrm{S}_{HH}\mathrm{S}_{VV}{}^*) < 0$, double-bounce scattering is dominant, and $\beta = 1$.

Although the Freeman-Durden decomposition is simple to implement, it has two major deficiency: the reflection symmetry assumption and negative powers of surface and double-bounce scatterings. The Freeman-Durden decomposition concerns only the reflection symmetry instead of rotation symmetry or both. The assumption of reflection symmetry denies the correlations existing between co-pol and cross-pol (T_{13}, T_{23}**=0**). Therefore, all cross-pol power is assigned to volume scattering, and volume scattering tends to be overestimated. The overestimation of P_V contributes to the negative power of surface and double-bounce scattering, because when volume scattering is

determined, the rest of the elements in the coherency matrix should be undertaken only by surface and double-bounce scattering:

$$\boldsymbol{C_{SD}} = \begin{bmatrix} |\beta|^2 f_S + |\alpha|^2 f_D & \beta f_S + \alpha f_D \\ \beta^* f_S + \alpha^* f_D & f_S + f_D \end{bmatrix} = \begin{bmatrix} c_{11} & c_{13} \\ c_{31} & c_{33} \end{bmatrix} \tag{2.69}$$

This restriction results in an invalid power estimation (negative power), especially when any of the following conditions are violated:

$$T_{11} - 2T_{33} \geq 0$$

$$T_{22} - T_{33} \geq 0$$

$$(T_{11} - 2T_{33})(T_{22} - T_{33}) - |T_{12}|^2 \geq 0 \tag{3.22}$$

Negative power occurs when $|c_{13}|$ is too large, yielding a negative determinant of $\boldsymbol{C_{SD}}$. The negative powers can be avoided by adjusting the determinant of $\boldsymbol{C_{SD}}$ to 0 through fixing the magnitude of c_{13}:

$$c_{13}{}' = \frac{\sqrt{c_{11}c_{33}}}{|c_{13}|} c_{13} \tag{2.70}$$

This methodology has been written into the SNAP ESA software as generalized Freeman-Durden decomposition. On the other hand, the ratio $\frac{|\alpha|}{\beta}$ can be determined by

$$\frac{|\alpha|}{\beta} = \frac{\sum_{n_D} \frac{\mathrm{R}_{TH}\mathrm{R}_{GH}}{\mathrm{R}_{TV}\mathrm{R}_{GV}}}{\sum_{n_S} \frac{\mathrm{R}_H}{\mathrm{R}_V}} = \frac{n_D \cdot \frac{\mathrm{R}_{TH}\mathrm{R}_{GH}}{\mathrm{R}_{TV}\mathrm{R}_{GV}}}{n_S \cdot \frac{\mathrm{R}_H}{\mathrm{R}_V}} = \frac{n_D}{n_S} \tag{2.71}$$

where n_i is the number of corresponding scattering occurrences over the pixel field. Co-polarized ratio for surface and double-bounce scattering can be safely assumed as equal, and this information can be retrieved from the distribution of alpha angle α (alpha angle is different from the α ratio in Freeman-Durden decomposition) or entropy-alpha angle space. Once we fix one of the α and β or add the ratio $\frac{|\alpha|}{\beta}$, the residual parameters can be easily estimated from the rest of the equations.

When applying the traditional Freeman-Durden decomposition, the negative power issue may occur in open water area especially when the signals received by sensor are weak, which can be explained by the overestimated volume scattering and negative determinant of covariance matrix excluding the volume scattering. Note that the replacement of surface scattering by incoherent scattering model can mitigate the negative power problem in generalized Freeman-Durden decomposition.

In the end, the contribution of each scattering mechanism can be determined:

$$\mathrm{Span}(\boldsymbol{S}) = |\mathrm{S}_{HH}|^2 + 2|\mathrm{S}_{HV}|^2 + |\mathrm{S}_{VV}|^2 = \mathrm{P}_S + \mathrm{P}_D + \mathrm{P}_V \tag{2.72}$$

where

$$P_S = (1 + |\beta|^2) f_S \tag{2.73}$$

$$P_D = (1 + |\alpha|^2) f_D \tag{2.74}$$

$$P_V = 8 f_V \tag{2.75}$$

2.7 Statistics and Classifiers Used in This Thesis

The scattering operators and target decompositions were introduced in Sections 2.5 and 2.6, respectively. Therefore, all the polarimetric features (backscatter intensity, covariance matrix, decomposition parameters and secondary physical parameters) can be generated for can be used as inputs to classifiers. In this section, the statistical properties of these parameters is summarized and classifiers are then introduced in Section 2.7.4.

2.7.1 Multilooking

In a single-look complex mode, the azimuth resolution is generally higher than the resolution in range direction, which applies to RADARSAT-2 Single Look Complex data used in this thesis. Multilooking involves taking the average of N single-look data in the azimuth direction (Lee & Pottier, 2009). There are two benefits achieved from this processing: it reduces speckle noise on the one hand; on the other hand, the multilooking pixel spacing is nearly square in measurements.

The number of looks for a square pixel is calculated through

$$N = \frac{\Delta r}{\sin(\theta)\Delta a} \tag{2.76}$$

where Δr and Δa are range spacing and azimuth spacing respectively, and θ is the incidence angle. Note that the pixel spacing is different from the resolution. Pixel spacing is the distance between adjacent pixels in an image measured in metres, while spatial resolution is the minimum distance that radar can distinguish between adjacent targets.

2.7.2 Radar Signal Statistics for Intensity

2.7.2.1 Gaussian Distribution of Real and Imaginary Parts of Signals

The real and imaginary components, i and q, of each polarization have a Gaussian distribution, which is denoted as $i, q \sim \mathcal{N}(\mu = 0,\ \sigma^2)$. The probability density function (PDF) is

$$f(x|\mu, \sigma^2) = \frac{1}{\sigma\sqrt{2\pi}} e^{-\frac{(x-\mu)^2}{2\sigma^2}} \tag{2.77}$$

2.7.2.2 Rayleigh Distribution of Amplitude

The amplitude for individual polarization $A = \sqrt{i^2 + q^2}$ is Rayleigh distributed with mean $\sqrt{\frac{\pi}{2}}\sigma$ and variance $\frac{4-\pi}{2}\sigma^2$. The PDF of Rayleigh distribution is given by

$$f(A|\sigma) = \frac{A}{\sigma^2} e^{-\frac{A^2}{2\sigma^2}} \tag{2.78}$$

2.7.2.3 Gamma Distributions of Multilooked Intensity

The intensity $I = A^2 = i^2 + q^2$ has an exponential distribution, denoted as $I \sim \mathcal{E}xp(I|\lambda = \frac{1}{2\sigma^2})$. Its PDF is given by

$$f\left(I\middle|\lambda = \frac{1}{2\sigma^2}\right) = \frac{1}{2\sigma^2} e^{-\frac{I}{2\sigma^2}} \tag{2.79}$$

As an extension to the multilooking intensity is given by

$$I = \frac{1}{N}\sum_{n=1}^{N} I_n = \frac{1}{N}\sum_{n=1}^{N}({i_n}^2 + {q_n}^2) \tag{2.80}$$

Once the real part and the imaginary part of signals have been standardized to have a mean of 0 and standard deviation of 1, the NI will be distributed according to the Chi-squared distribution with $2N$ degrees of freedom, denoted as $NI \sim \chi^2(2N)$. The PDF of Chi-squared distribution is expressed as

$$f(x = NI|k = 2N) = \frac{1}{2^{\frac{k}{2}}\Gamma(\frac{k}{2})} x^{\frac{k}{2}-1} e^{-\frac{x}{2}} = \frac{1}{2^N \Gamma(N)} (NI)^{N-1} e^{-\frac{NI}{2}} \quad (2.81)$$

where $\Gamma(n)$ represents the gamma function. When n is a positive integer, the gamma function is

$$\Gamma(n) = (n-1)! \quad (2.82)$$

Thus, the $\mathrm{E}(I) = 2$ and $\mathrm{Var}(I) = \frac{4}{N}$. Note that the N-look amplitude $\sqrt{NI}$ has a Chi distribution.

When signals have not been standardized, the multilooked intensity NI is distributed according to the Gamma distribution, denoted as $NI \sim \Gamma(\alpha = \frac{k}{2} = N, \theta = 2\sigma^2)$, where α is the shape parameter, and θ the scale parameter. The PDF of multilooking intensity is given by

$$f(x = NI|\alpha = N, \theta = 2\sigma^2) = \frac{1}{\theta^\alpha \Gamma(\alpha)} x^{\alpha-1} e^{-\frac{x}{\theta}} = \frac{1}{2^N \sigma^{2N} \Gamma(N)} (NI)^{N-1} e^{-\frac{NI}{2\sigma^2}} \quad (2.83)$$

The mean and the variance are $\mathrm{E}(I) = 2\sigma^2$ and $\mathrm{Var}(I) = \frac{4\sigma^4}{N}$.

2.7.2.4 K-Distribution of Multilooked Intensity from Heterogeneous Scattering

Over homogeneous areas, the intensity of signals is Chi-squared distributed (or Gamma distributed if not standardized). However, signals from heterogeneous backscattering processes may be modeled more rationally through K-distribution. The intensity I_h received by a radar receiver can be modeled by a product of Gamma distribution and a Gamma distributed noise variable g as a texture descriptor (Lee & Pottier, 2009).

To make things simple, we rescale the multilooked intensity through

$$I_r = \frac{I}{E(I)} = \frac{I}{2\sigma^2} \tag{2.84}$$

Then the normalized multilooked intensity is gamma distributed $I_r \sim \Gamma(\alpha = N, \theta = \frac{1}{N})$, with its mean $\mathrm{E}(I_r) = 1$ and $\mathrm{Var}(I_r) = \frac{1}{N}$. The PDF is given by

$$f\left(I_r \middle| \alpha = N, \theta = \frac{1}{N}\right) = \frac{N^N {I_r}^{N-1}}{\Gamma(N)} e^{-NI_r} \tag{2.85}$$

On the other hand, multilooked intensity from the heterogeneous scattering may have a gamma processes on its mean value $\mathrm{E}(I_r) \sim \Gamma$; thus, we introduce a Gamma distributed texture descriptor $\mathrm{g} \sim \Gamma(\alpha = v, \theta = \frac{1}{v})$ as noises on the mean of normalized multilooked intensity:

$$f(\mathrm{g}) = \frac{v^v g^{v-1}}{\Gamma(v)} e^{-vg} \tag{2.86}$$

with its mean $\mathrm{E}(g) = 1$ and $\mathrm{Var}(g) = \frac{1}{v}$.

The multilooked intensity from heterogeneous scattering can be expressed as

$$I_h = gI_r \tag{2.87}$$

Its probability function is given by

$$f(I_h) = \int_0^\infty f(I_h|g) f(g)\, \mathrm{d}g \tag{2.88}$$

where $(I_h|g) \sim \Gamma(\alpha = N, \theta = \frac{g}{N})$ can be transformed from Equation 2.85, which is given by

$$f(I_h|g) = \frac{N^N {I_h}^{N-1}}{\Gamma(N) g^N} e^{-\frac{NI_h}{g}} \tag{2.89}$$

As briefly reviewed here, the intensity I_h received by a radar receiver can be modeled by a product of the Gamma distributed I_r and a Gamma distributed noise variable g. The I_r is gamma

distributed with mean g~ $\Gamma(\alpha = v, \theta = \frac{1}{v})$ and shape parameter $\alpha = N$. The mean of g is denoted as $\mu = 1$. Therefore, the PDF of K-distributed intensity from heterogeneous scattering can be represented by

$$f(I_h|\mu = 1, v, N) = \frac{2(Nv)^{\frac{N+v}{2}} I_h^{\frac{N+v}{2}-1}}{\Gamma(N)\Gamma(v)} \mathrm{K}_{v-N}(2\sqrt{NvI_h}) \tag{2.90}$$

where $\mathrm{K}_\alpha(.)$ is the modified Bessel function of the second kind, defined by:

$$\mathrm{K}_\alpha(x) = \frac{\pi}{2} \frac{\mathrm{I}_{-\alpha}(x) - \mathrm{I}_\alpha(x)}{\sin(\alpha\pi)} \tag{2.91}$$

where $\mathrm{I}_\alpha(.)$ is the modified Bessel function of the first kind, defined by:

$$\mathrm{I}_\alpha(x) = \sum_{m=0}^{\infty} \frac{1}{m!\Gamma(m+\alpha+1)} \left(\frac{x}{2}\right)^{2m+\alpha} \tag{2.92}$$

2.7.3 Scattering Statistics and Coherence Statistics between Polarizations

2.7.3.1 Complex Gaussian Distribution of Scattering Vector

In Section 2.4.3, complex scattering vectors $\boldsymbol{k}_L$ and $\boldsymbol{k}_P$ are represented in Equation 2.35 and 2.36 respectively. The dimension of scattering vector is denoted as $n = 3$ on a reciprocal condition. The mean of $\boldsymbol{k}$, $E(k_i) = \mu_i = 0$ for $i = 1,2 \ldots n$, so we have $\boldsymbol{\mu} = \mathbf{0}$. The PDF for scattering vector $\boldsymbol{k}$ is given by multivariate complex Gaussian distribution:

$$f(\boldsymbol{k}|\boldsymbol{\mu} = \mathbf{0}, \boldsymbol{\Sigma}) = \frac{1}{\pi^n|\boldsymbol{\Sigma}|} e^{-\boldsymbol{k}^{*T}\boldsymbol{\Sigma}^{-1}\boldsymbol{k}} \tag{2.93}$$

where $\boldsymbol{\Sigma}$ is the complex positive definite covariance matrix of $\boldsymbol{k}$, which can be the unbiased sample covariance matrix or can be estimated through maximum likelihood estimator.

2.7.3.2 Complex Wishart Distribution of Covariance Matrix or Coherency Matrix

The multilooked polarimetric analysis takes multiple single look complex covariance matrices. The N-look covariance matrix is expressed as

$$\boldsymbol{C_n} = \frac{1}{N}\boldsymbol{W} = \frac{1}{N}\sum_{i=1}^{N} \boldsymbol{k_i}\boldsymbol{k_i}^{*T} \tag{2.94}$$

where $\boldsymbol{k_i} \sim \mathcal{N}(\mathbf{0}, \boldsymbol{\Sigma})$. The matrix $\boldsymbol{W}$ is complex Wishart distributed $\boldsymbol{W} \sim \mathcal{W}(N, \boldsymbol{\Sigma})$, with N degrees of freedom, which is the number of looks in this case. The PDF of $\boldsymbol{W}$ is represented by

$$f(\boldsymbol{W}|N, \boldsymbol{\Sigma}) = \frac{|\boldsymbol{W}|^{N-n}}{I(N,n)|\boldsymbol{\Sigma}|^N} e^{-Trace(\boldsymbol{\Sigma}^{-1}\boldsymbol{W})} \tag{2.95}$$

where n is the dimension of $\boldsymbol{k}$ With

$$I(N, n) = \pi^{\frac{1}{2}n(n-1)} \prod_{i=1}^{n} \Gamma(N - i + 1) \tag{2.96}$$

where the Gamma function given by: $\Gamma(n) = (n-1)!$ The PDF for averaged covariance matrix $\boldsymbol{C_n}$ is given by

$$f(\boldsymbol{C_n}|N, \boldsymbol{\Sigma}) = \frac{N^{Nn}|\boldsymbol{C_n}|^{N-n}}{I(N,n)|\boldsymbol{\Sigma}|^N} e^{-N \cdot Trace(\boldsymbol{\Sigma}^{-1}\boldsymbol{C_n})} \tag{2.97}$$

2.7.4 Classification Approach Used in This Thesis

2.7.4.1 H-alpha Complex Wishart Classifier

Since radar signals are averaged through multilooking and speckle filtering, only the covariance matrix or coherency matrix can be employed for analyzing the incoherent targets. It was introduced in Section 2.7.3.2 that the covariance matrix and coherency matrix are complex Wishart distributed:

$$f(\boldsymbol{C}|N, \boldsymbol{\Sigma}) = \frac{N^{Nn}|\boldsymbol{C}|^{N-n}}{I(N,n)|\boldsymbol{\Sigma}|^N} e^{-N \cdot Trace(\boldsymbol{\Sigma}^{-1}\boldsymbol{C})} \tag{2.98}$$

where $\boldsymbol{C}$ is the covariance matrix variable, N is the number of looks, n is the dimension of the target vector, and $\boldsymbol{\Sigma}$ is the positive definite covariance matrix of moment matching.

The unsupervised H- alpha complex Wishart classifier developed by Lee et al. (1999) was proposed to maximize the posterior: $P(\omega|\boldsymbol{X})$ by applying Bayes' rule:

$$P(\omega|\boldsymbol{X}) = \frac{P(\boldsymbol{X}|\omega)P(\omega)}{P(\boldsymbol{X})} \tag{2.99}$$

where ω represents the classes or labels of a scattering vector $\boldsymbol{k}$. Since $P(\boldsymbol{X})$ is an independent constant number, $\boldsymbol{k}$ belongs to class $\omega = i$, if $P(\boldsymbol{X}|\omega = i)P(\omega = i) > P(\boldsymbol{X}|\omega = j)P(\omega = j)$, for all $j \neq i$. The $f(\boldsymbol{C}|N, \boldsymbol{\Sigma})$ is the model used for the likelihood of a feature given a label, $P(\boldsymbol{X}|\omega)$. Maximizing the posterior is equivalent to minimizing the negative natural logarithm of the posterior. The maximum a posterior (MAP) function is therefore given by

$$
\begin{aligned}
MAP &= argmax \prod P(\boldsymbol{X}|\omega)P(\omega) \\
&= argmin \sum -ln\big(P(\boldsymbol{X}|\omega)P(\omega)\big) \\
&= argmin \sum -Nn\ln(N) - (N-n)\ln(C) + N \cdot Trace(\boldsymbol{\Sigma}^{-1}\boldsymbol{C}) + \ln\big(I(N,n)\big) + N\ln(|\boldsymbol{\Sigma}|) \\
&\qquad - \ln(P(\omega)) \\
&= argmin \sum N \cdot Trace(\boldsymbol{\Sigma}^{-1}\boldsymbol{C}) + N\, ln(|\boldsymbol{\Sigma}|) - ln(P(\omega))
\end{aligned}
\tag{2.100}
$$

Since the prior $P(\omega)$ has an unknown probability, Lee et al., (1999) assumed priors to be equal, thus this classifier now is equivalent to maximum likelihood estimation instead of a MAP algorithm. We name this maximum likelihood function as loss function:

$$L(\omega, \boldsymbol{\Sigma}, \boldsymbol{C}) = argmin \sum Trace(\boldsymbol{\Sigma}^{-1}\boldsymbol{C}) + \ln(|\boldsymbol{\Sigma}|) \tag{2.101}$$

Therefore, the pixels are assigned to the class with minimum of loss to achieve the overall minimum of the loss function.

This unsupervised classification employed expectation maximization (EM) has its optimizing algorithm, which involves two iterative steps. In the first expectation step, it estimates the covariance matrix $\boldsymbol{\Sigma}$ through the methods of moment. In the second maximization step, it reassigns the pixels to the corresponding classes for minimizing the loss function. Those two steps are iterated until the loss function converges or the termination criterion is met.

2.7.4.2 Markov Random Field

Since the Entropy-alpha Wishart classifier assumes that the priors for each class is equal at any time, the objective does not incorporate prior knowledge. However, regions or clusters are often homogeneous with neighboring pixels having similar properties and features. To fulfill the knowledge of neighboring pixels and prior probability, the Markov properties are considered due to the conditional independence of any two non-adjacent pixels. Therefore, Markov Random Field (MRF), a graphical model of a joint probability distribution by considering the neighboring pixels, is employed in this thesis.

Let $s = (i, j)$ denote the pixel at i, j in the graph S. For each pixel s in the image, it has a feature vector X_s; thus, we have the feature $\boldsymbol{X} = \{\boldsymbol{X}_s, s \in S\}$ for the whole image. Each pixel s has its corresponding label $\omega_s \in \Lambda$, where the Λ is the range of the classes the label can choose from. For the whole image, we have $\boldsymbol{\omega} = \{\omega_s, s \in S\}$. According to the Bayes' theorem, the posteriori $P(\boldsymbol{\omega}|\boldsymbol{X})$ is given by

$$P(\boldsymbol{\omega}|\boldsymbol{X}) = \frac{P(\boldsymbol{X}|\boldsymbol{\omega})P(\boldsymbol{\omega})}{P(\boldsymbol{X})} \tag{2.102}$$

which measures the probability of labelling given the observed feature $\boldsymbol{X}$. The objective of classifying the whole image is to find an optimal labelling which maximizes the $P(\boldsymbol{\omega}|\boldsymbol{X})$ by maximum a posteriori (MAP) estimation. Since $P(\boldsymbol{X})$ is a constant and independent of any classes to be chosen, MAP is equivalent to

$$\arg max\, P(\boldsymbol{\omega}|\boldsymbol{X}) \propto P(\boldsymbol{X}|\boldsymbol{\omega})P(\boldsymbol{\omega}) \tag{2.103}$$

The labelling field can be modeled as a Markov Random Field (MRF) if all the $\omega_s \in \Lambda$: $P(\boldsymbol{\omega}) > 0$; and if for every $s \in S,\ \omega_s \in \Lambda$, we have

$$P(\omega_s|\omega_r, r \neq s) = P(\omega_s|\omega_r, r \in N_s) \tag{2.104}$$

where the neighbour set N_s is defined as the surrounding pixels of a pixel s. Besides the neighbours, a subset C is defined as a clique if every pair of pixels in C are neighbours. A clique C_n containing n pixels is called an nth order clique, thus the set of cliques is denoted as

$$C = C_1 \cup C_2 \cup \cdots \cup C_k \tag{2.105}$$

The first order and second order clique are named after singleton and doubleton, respectively.

According to the Hammersley-Clifford theorem, the joint probability $P(\boldsymbol{\omega})$ of a MRF follows a Gibbs distribution:

$$P(\boldsymbol{\omega}) = \frac{1}{Z} e^{-U(\boldsymbol{\omega})} = \frac{1}{Z} e^{-\sum_{c \in C} V_c(\boldsymbol{\omega})} \tag{2.106}$$

where $Z = \sum_{\boldsymbol{\omega} \in \Omega} \exp(V_c(\boldsymbol{\omega}))$ is the normalizing constant, and Ω denotes all the possible labelling conditions, the $V_c(\boldsymbol{\omega})$ denotes the clique potential of clique C, the $U(\boldsymbol{\omega})$ is called the energy function, which requires taking the sum of potentials of all cliques:

$$U(\boldsymbol{\omega}) = \sum_{c \in C} V_c(\boldsymbol{\omega}) = \sum_{C_1} V_{C_1}(\omega) + \sum_{C_2} V_{C_2}(\omega) + \cdots \tag{2.107}$$

In this case, we do not have any hidden layer within the Markov model. Only the first order (singletons) and second order cliques (doubletons) are considered for determining the clique potential V_c, which are given by

$$V_{C_1}(\omega_s, r \in N_s) = \begin{cases} 0 & if\ \ \omega_s \\ \varepsilon & else \end{cases} \tag{2.108}$$

$$V_{C_2}(\omega_s, \omega_r, r \in N_s) = \begin{cases} \beta & if\ \ \omega_s \neq \omega_r \\ -\beta & if\ \ \omega_s = \omega_r \end{cases} \tag{2.109}$$

where $\varepsilon, \beta > 0$ is a parameter tuning the weights of contributions of corresponding clique potentials.

The likelihood $P(\boldsymbol{X}|\boldsymbol{\omega})$ is determined by the distributions of the features themselves. For instance, the multi-looked intensity from heterogeneous scattering should be K-distributed according to the Equation 2.90, the scattering matrix and covariance matrix are complex Gaussian distributed and complex Wishart distributed, which were introduced in Sections 2.6.3.1 and 2.6.3.2, respectively. The decomposition parameters are assumed to be Gaussian distributed. The estimate of the parameters in these PDFs are completed through the method of moments.

The entropy-alpha Wishart classifier and MRF classifier were introduced above. Note that the purpose of using the entropy-alpha Wishart classifier is to label the images instead of achieving the final classification output. The entropy-alpha Wishart classifier only includes the covariance matrix as input and the maximized likelihood. However, the MRF classifier includes more polarimetric features and considers the prior knowledge based on neighboring pixels. Therefore, in this research, the two classifiers were integrated as a whole, where the posterior was calculated through the product of maximized likelihood from Wishart classifier and the prior based on MRF.

2.8 RADARSAT-2

Data employed in this thesis are RADARSAT-2 Wide Standard Quadrature Polarimetric images. RADARSAT-2 is equipped with an active C-band antenna, and takes 24 days to revisit its original orbit path. Wide Standard Quad-pol beam mode images (single look complex, SLC, product) were used for extracting polarimetric features and then in classification. The images cover 50 km by 25 km area at ground range by azimuth range. The pixel spacing for the near side is 8.0 m by 5.1 m (slant range by azimuth range), and the pixel spacing for the far side is 11.8 m by 5.1 m (MDA, 2016). The slant range resolution is 9.0 m for SQ1 to SQ11 and 12.8 for SQ12 to SQ21. The azimuth resolution is 7.6 m. The noise-equivalent sigma-zero is -35± dB (MDA, 2016).

2.8.1 Radar Operation

The RADARSAT-2 system includes a radar transmitter, a radar receiver and a data downlink transmitter (MDA, 2016). The antenna in the radar transmitter and receiver directs the transmitted energy in a beam, normal to the satellite track. The elevation profile and angle are adjusted to ensure that the beam arrives at the earth surface at a certain range of incidence angle (MDA, 2016).

Radar imaging can be carried out in different beam modes, which contain their own unique imaging characteristics for variety of application needs. These characteristics include nominal swath widths, pulse bandwidths, sampling rates, and a specific set of available beams at specific incidence angles (MDA, 2016). The fundamental imaging modes available are Single Beam, ScanSAR, and Spotlight. These beam modes are summarized in the Figure 2.2 (MDA, 2016). When the radar operates in a given beam mode, the receiver receives scattered or reflected signals after the transmitted signals interacts with the earth surface.

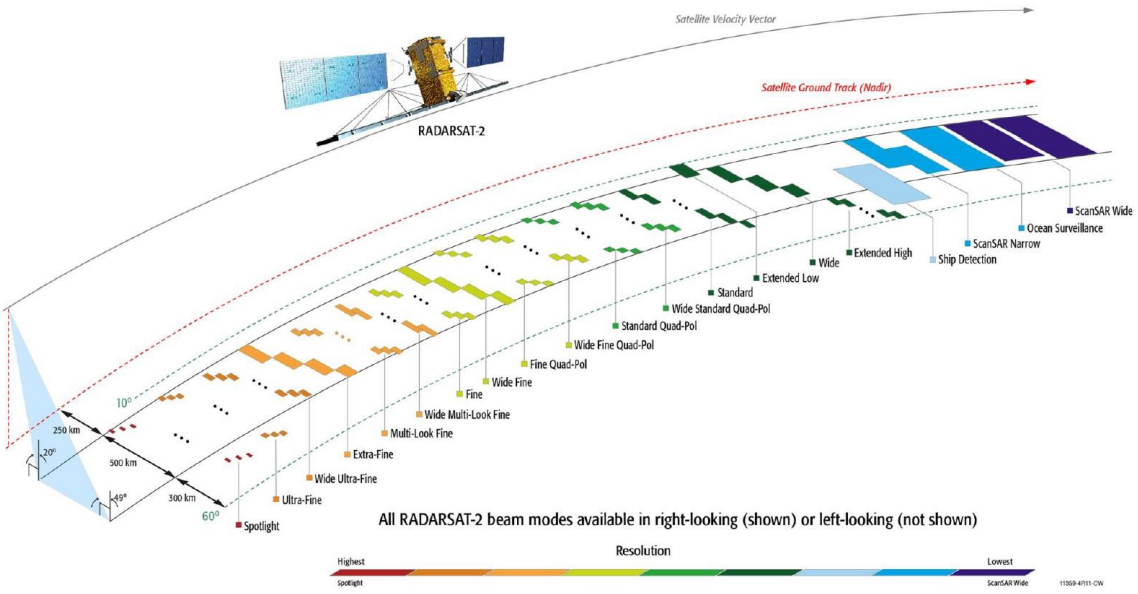

Figure 2.2: RADARSAT-2 SAR beam modes. It shows the unique imaging characteristics of the beam modes. These characteristics include nominal swath widths, swath position, and specific set of beams at specific incidence angles. Figure retrieved from RADARSAT-2 Product Description (MDA, 2016).

2.8.2 Wide Standard Quad Polarization Beam Mode

Single Beam modes are strip-map SAR modes. The beam elevation and profile are constant during the data collection. The beam mode employed in this thesis is the Wide Standard Quad Polarization. The radar transmits pulses in either horizontal or vertical polarizations alternatively, and receives the returns from each pulse in both horizontal and vertical polarizations separately but simultaneously (MDA, 2016). Therefore, it collects full polarimetric imaging signals at the same time. The Wide Standard Quad Polarization Beam Mode extends the swath range up to 50 km. The incidence angle, ranging 18-42 degrees, are covered by 21 beams. The characteristics of beam modes on swath length and resolution are illustrated in Figure 2.3.

2.8.3 Single Look Complex Product

The products offered by RADARSAT-2 can be one of three basic types: Slant Range data, Ground Range data, and Geocorrected data. The slant range is the length measured between the radar and the target, while the ground range is the length measured between the ground track and the target. Since it measures the distance in slant range instead of the distance along the ground, the distance in slant range always represents less than that in corresponding ground range and slant range scale distortion occurs, resulting in varying scales from near to far range in each image, which is depicted in Figure 2.4. The product employed in this thesis is the Single Look Complex product, which is Slant Range data; therefore, no interpolation into ground range is performed for this product, and slant range is therefore converted to ground range by

$$d_g = \frac{d_s}{\sin\theta} \tag{3.1}$$

where θ the incidence angle, d_s and d_g are slant range and ground range, respectively.

Each SLC Wide standard Quad Pol image covers 50 km by 25 km area at ground range by azimuth range. The pixel spacing for the near side is 8.0 m by 5.1 m (slant range by azimuth range), and the pixel spacing for the far side is 11.8 m by 5.1 m (MDA, 2016). The slant range resolution is 9.0 m for SQ1 to SQ11 and 12.8 for SQ12 to SQ21 (MDA, 2016). The azimuth resolution is 7.6 m. The noise-equivalent sigma-zero is -35± dB (MDA, 2016). The incidence angle ranges from 18 to 42 degrees for different swath positions, which are summarized in Table 2.4.

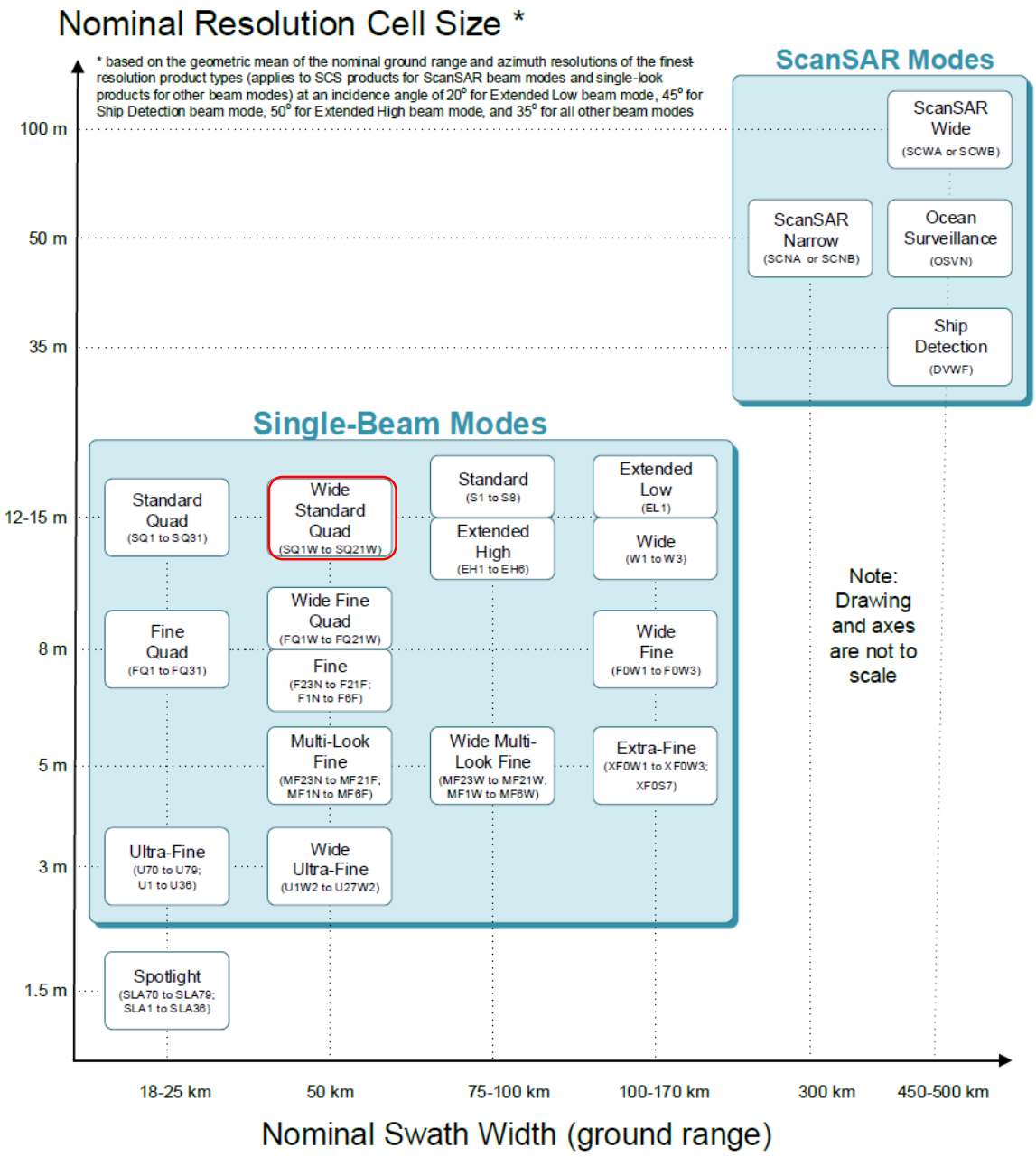

Figure 2.3: Relationship between beam modes and sensor modes including swath width and resolution cell size for RADARSAT-2 products. The beam positions for each beam mode are also indicated in parentheses. Figure retrieved from RADARSAT-2 Product Description (MDA, 2016).

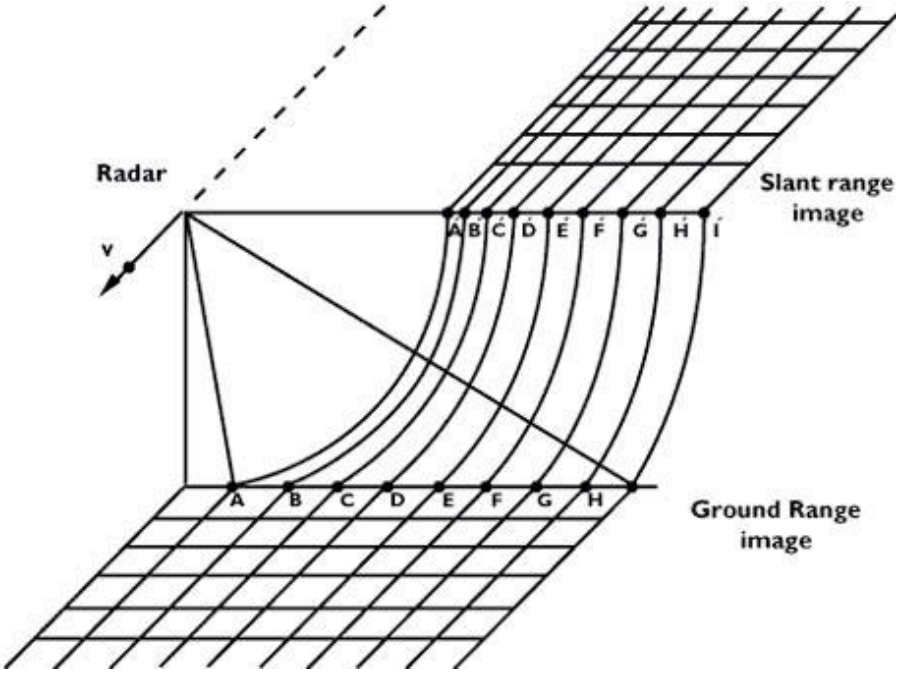

Figure 2.4: The relationship between slant range image and ground range image. The slant range is the length measured between the radar and the target, while the ground range is the length measured between the ground track and the target. This figure is retrieved from European Space Agency Earth Online Website: https://earth.esa.int/web/guest/missions/esa-operational-eo-missions/ers/instruments/sar/applications/radar-courses/content-2/-/asset_publisher/qIBc6NYRXfnG/content/radar-course-2-slant-range-ground-range

Table 2.4: Incidence Angle and Range Resolution for Specific Swath Position of Wide Standard Quad-Polarization Beam Mode

Beam/ Swath Position	Near Incidence Angle (degrees)	Far Incidence Angle (degrees)	Nominal Near Range Resolution (m)	Nominal Far Range Resolution (m)
SQ1W	17.5	21.2	30.0	24.9
SQ2W	19.0	22.7	27.7	23.4
SQ3W	20.0	23.6	26.3	22.5
SQ4W	21.3	24.8	24.9	21.5
SQ5W	22.5	26.0	23.6	20.6
SQ6W	23.7	27.2	22.4	19.8
SQ7W	24.9	28.3	21.4	19.0
SQ8W	26.1	29.4	20.5	18.4
SQ9W	27.2	30.5	19.7	17.8
SQ10W	28.4	31.6	19.0	17.2
SQ11W	29.5	32.6	18.3	16.7
SQ12W	30.6	33.7	26.5	24.3
SQ13W	31.7	34.7	25.7	23.7
SQ14W	32.7	35.7	24.9	23.1
SQ15W	33.7	36.7	24.3	22.6
SQ16W	34.8	37.6	23.6	22.1
SQ17W	35.7	38.6	23.1	21.6
SQ18W	36.7	39.5	22.5	21.2
SQ19W	37.7	40.4	22.0	20.8
SQ20W	38.6	41.3	21.6	20.4
SQ21W	39.5	42.1	21.2	20.1

2.8.4 Pixel Representation Radiometric Calibration

In a single-look complex mode, each pixel is represented by a complex number. The complex representation consists of two signed integers for the real and imaginary parts: i and q. The magnitude of the complex number is denoted as:

$$DN = \sqrt{i^2 + q^2} \tag{2.110}$$

Note that the magnitude of the complex number is different from the amplitude of the electromagnetic wave.

Radiometric calibration of the data is essential to adjust the radiometric values without contribution of the target characteristics (Richards, 2009). The digital values received by the sensor can be converted to calibrated physical parameters. The radar backscatter coefficient (sigma nought σ^0), radar brightness (beta nought β^0), and Gamma nought (γ^0) are three of the most common calibrated coefficients that can be scaled from original pixel values.

The backscatter coefficient is the averaged radar cross section per unit area; the radar brightness corresponds to the backscatter per unit area in slant range, which requires no prior of the local incident angle; Gamma corresponds to the backscattering coefficient normalized by the cosine of the incidence angle. The scaling procedure can be derived from the following (only the sigma nought is shown as an example):

$$\sigma^0 = \frac{|i+jq|^2}{A^2} = \frac{|DN|^2}{A^2} \tag{2.111}$$

where A is the corresponding range dependent gain for sigma nought. The corresponding gain value A of sigma nought, beta nought, and gamma can be found in corresponding Look-up Table files.

Calibrated sigma nought, beta nought and gamma nought can be converted through

$$\sigma^0 = \beta^0 \sin\alpha \tag{2.112}$$

$$\gamma^0 = \beta^0 \tan\alpha \tag{2.113}$$

where α is the local incidence angle. These coefficients in decibels (dB) can be given by the following (only the sigma nought in dB is shown as an example):

$$\sigma^0(dB) = 10\log_{10}\sigma^0 \tag{2.114}$$

With the assumption that the backscattering is constant across a pixel, we recall Equation 2.28, which indicated the relationship between the radar cross section and the elements in the scattering matrix. The elements in the scattering matrix can be related to sigma nought as follows:

$$\sigma^0 = \frac{\sigma}{A_0} = \frac{4\pi|S|^2}{\Delta r \Delta a} \tag{2.115}$$

where Δr and Δa are range spacing and azimuth spacing, respectively. Note that sigma nought is a real-valued coefficient, while scattering matrix is valuable only when the elements (so-called scattering coefficient or scattering amplitudes) are complex. The direct transformation from the complex pixel value to scattering amplitude is given by:

$$S = \frac{\sqrt{\Delta r \Delta a}}{2A\sqrt{\pi}}(i + jq) \tag{2.116}$$

where S is the element in the scattering matrix in equation 2.29. At this stage, the polarization descriptors including the intensities and amplitudes and scattering operators can be fully built from the RADARSAT-2 Standard quad-pol data.

2.9 Summary

This chapter reviewed recent studies on lake ice mapping and relevant methodologies that have been used for SAR image classifications. It identified the needs for improvement in the automated classification methodology to help operationalize lake ice monitoring using polarimetric RADARSAT-2 data at CIS. The basic principles of monochromatic electromagnetic waves are helpful for understanding the representations of polarization and further scattering processes. The characteristics of polarimetric scattering processes provide insight to the scatterers (open water and lake ice); therefore, the statistical properties of polarimetric parameters including multi-looked polarization intensity, covariance matrix, decomposition results, and secondary physical parameters (entropy and alpha angle) are introduced to the classifier for determining the likelihood function. The MRF provides an approach to calculate the prior probability, therefore the posterior probability can be achieved by following Bayes' theorem. The connections between the radar signal and the theories of polarization descriptors and scattering operators were summarized in the Section 2.8, which is the first step to generate polarimetric parameters from RADARSAT-2 images. The next chapter consists of a paper, to be submitted for publication in a journal, which used Wide Standard Quad-pol beam mode RADARSAT-2 images with the H-alpha Wishart classifier and MRF for the classification of lake ice and open water using Great Bear Lake as the study area.

3 Polarimetric Radar Imaging for Lake Ice Mapping

3.1 Introduction

In Canada, over 4 million square kilometres of waters are covered by ice in winter (Canadian Ice Service [CIS], 2017). Since lakes are a widespread land feature in many regions of Canada, lake ice cover is an important component of the Canadian cryosphere (Duguay et al., 2006). Lake ice phenology parameters (freeze-up, break-up, and ice cover duration) are highly relevant in the context of global climate change (Duguay et al., 2015) as lake ice has been proven to be a sensitive indicator of climatic variability and change (Duguay et al., 2006; Colbeck, 2012; Brown & Duguay, 2012). Ice extent and duration have an impact on local weather conditions and regional climate, influencing lake-atmosphere interactions (Duguay et al., 2006; Du et al., 2017). Lake ice also has a significant influence on aquatic ecosystems including the composition and abundance of aquatic species, as well as on human activities including marine transportation, fishing, resource development, and tourism (CIS, 2017).

Consistent and accurate records of ice phenology provide valuable information for weather forecasting and for climate change analysis (Du et al., 2017). The Canadian Ice Service (CIS) has the responsibility for operational monitoring of lake ice, sea ice, and iceberg conditions in Canadian Regions and adjacent waters (Arkett et al., 2013). The CIS primarily relies on visual interpretation of satellite optical and synthetic aperture radar (SAR) imagery to conduct analyses and prepare lakes ice products (fractional ice coverage for close to 140 lakes on a weekly basis and daily ice charts of the Laurentian Great Lakes). Since SAR can acquire data under polar darkness and cloud cover conditions, it is a tool of primary importance for lake ice monitoring across Canada. Since the performance of single (e.g. HH) and dual-polarized (e.g. HH and HV) imagery is limited by the loss of full polarization and phase information, there is a great deal of interest in using polarimetric SAR data for lake ice monitoring. Given the large volume of satellite images and the expected rapid growth of data from upcoming satellite missions such as the RADARSAT Constellation Mission (RCM), exploring automated image classification for polarimetric SAR imagery is paramount (Arkett et al., 2013; CIS, 2017).

Previous research using SAR for freshwater ice mapping/monitoring has largely focus on shallow Arctic and sub-Arctic lakes for the determination of floating and grounded ice as well as determination of freeze-up and break-up dates. Investigations of radar backscatter from large lakes have been more limited (e.g. Nghiem & Leshkevich, 2007; Leshkevich & Nghiem, 2013). SAR backscatter from thin lake ice during the initial ice formation has been reported to be lower than -18 dB (Morris et al., 1995; Duguay et al., 2002). Floating ice on shallow lakes later during the ice season has been characterized by high backscatter, attributed to the double-bounce scattering from columnar air inclusions and ice-water interface, and an increase of volume scattering (Geldsetzer, van der Sanden & Brisco, 2010). However, recent work supports single bounce scattering at the ice-water interface as the dominant scattering mechanism (Atwood et al., 2015). The low radar returns have been reported when ice freezes to the bottom of shallow lakes (e.g. Duguay et al., 2002; Atwood et al., 2015). A decrease in backscatter has also been document from floating ice during the break-up period due to radar signal absorption by the wet snow and specular reflection from the water or ponds on the ice surface (Duguay et al., 2002; Geldsetzer, van der Sanden & Brisco, 2010). Co-polarized backscattering at a given frequency from open water not only depends on incidence angle, but it is also influenced by wind speed and wind direction relative to the radar look direction (Geldsetzer & van der Sanden, 2013). However, cross-polarized backscattering can be independent of wind direction and incidence angle (Vachon & Wolfe, 2011). Both co-pol and cross-pol backscattering from lake ice are affected by the geometry of ice surface, ice structure, dielectric parameter, and incidence angle (Duguay et al., 2002; Geldsetzer & van der Sanden, 2013). Since single and dual-pol data are limited by their capability to distinguish open water from different ice types (Scheuchl et al., 2004; Geldsetzer & Yackel, 2009), dual-pol signals combined with polarimetric parameters may increase the potential for ice discrimination (Geldsetzer et al., 2011). C-band polarimetric and non-polarimetric parameters, including sigma naught of individual polarizations, co-pol and cross-pol ratios, the co-pol correlation coefficient, entropy, anisotropy and alpha angle, were assessed and summarized for their potential to discriminate lake ice and open water (Geldsetzer & van der Sanden, 2013). The study showed that the single-pol VV was preferred when wind speed measurements are available and incidence angle is low. The co-pol ratio was recommended when the incidence angle is larger than 31.2° and, in such case, wind speed data is not required (Geldsetzer & van der Sanden, 2013). Anisotropy also showed its great

potential when incidence angle is lower than 27.6°, and it is insensitive to wind as well (Geldsetzer & van der Sanden, 2013).

The characteristics of scattering mechanisms from ice and open water have been investigated. Using shipped-based and satellite SAR observations of the Great Lakes, it has been sown that when incidence angle is small (lower than 30°), scattering is dominated by surface scattering from open water where water with high relative permittivity has higher co-pol backscatter than ice (Leshkevich & Nghiem, 2013). For large incidence angles, surface scattering is dominant for both open water surface and ice covered area, and volume scattering tends to contribute more from ice (Nghiem & Leshkevich, 2007; Leshkevich & Nghiem, 2013). To be more specific, the surface scattering is mainly contributed from the air-ice (if no snow), air-snow, snow-ice and ice-water interfaces (Hossain et al., 2014; Atwood et al., 2015). When the ice surface is smooth (and thin) enough to act as a specular reflector, low or no backscatter can be observed (Cable et al., 2014). Volume scattering is contributed due to the dielectric discontinuities of the medium and geometry of the ice structure (Hossain et al., 2014). Double-bounce scattering occasionally occurs on ice ridges and ice fragments, and it is rarely dominant for the overall scattering compared to surface and volume scattering (Scheuchl, Hajnsek & Cumming, 2002).

The objective of this study was to develop an automated segmentation procedure of polarimetric SAR images for the classification of lake ice and open water. The physical scattering mechanisms of lake ice were analyzed from a quadrature polarimetric RADARSAT-2 dataset obtained over Great Bear Lake, Canada, with the intent of automatically mapping/monitoring open water and ice cover during the break-up and freeze-up periods of 2015. As the Canadian RADARSAT Constellation (RCM) and other future missions are being planned for launch, the use of compact polarimetry (CP) is also drawing attention for lake ice classification (Dabboor & Geldsetzer, 2014). However, the necessity of an efficient and automated segmentation approach of SAR imagery (single, dual-pol and polarimetric) is still paramount to enhance lake ice monitoring capabilities at ice services such as CIS.

3.2 Study Area

The SAR data used in this study were acquired over Great Bear Lake (GBL), Northwest Territories, which is the largest lake entirely within Canada (Figure 3.1). The lake straddles the Arctic Circle between 65° and 67° N and between 118° and 123° W. Its altitude is 156 m above sea level. It is one of the major freshwater resources of northern Canada. The surface area of GBL is 3,1153 km^2. Globally, the lake ranks 9th in surface area and 15th in depth (maximum depth: 446 m; average depth 71.7 m). RADARSAT-2 images acquired for this study cover an area of 25 km by 50 km in the northern part of GBL (Figure 3.1).

Figure 3.1: Location of Great Bear Lake within Canada on the left (delineated by solid red line) and area covered by RADARSAT-2 acquisitions on right (delineated by dashed blue line)

3.3 Data and Methods

3.3.1 Data

Data employed in this study is RADARSAT-2 Wide Standard Quadrature (SQ) Polarimetric imagery. Fourteen SQ images of single look complex product were acquired from both ascending and descending overpasses during spring break-up and fall freeze-up of 2015. RADARSAT-2 was launched in December 14, 2007. The orbit of the satellite is polar, sun-synchronous orbit with a period of approximately 101 minutes. The satellite takes 24 days to revisit its original orbit path. In the Wide SQ beam mode, the C-band steerable antenna transmits and receives 5405 MHz microwave pulses separately but simultaneously with an assigned bandwidth of 100,540 kHz (MacDonald, Dettwiler and Associates Ltd. [MDA], 2014). Therefore, full polarimetric imagery provides wide swaths of approximately 50 km with incidence angle from 18 degrees to 42 degrees for 21 swath positions. In the single look complex product of Wide SQ mode, images cover 50 km by 25 km in area at ground range by azimuth range. The pixel spacing for the near side is 8.0 m by 5.1 m (slant range by azimuth range) and the pixel spacing for the far side is 11.8 m by 5.1 m (MDA, 2016). The slant range resolution is 9.0 m for SQ1 to SQ11 and 12.8 for SQ12 to SQ21 (MDA, 2016). The azimuth resolution is 7.6 m. The noise-equivalent sigma-zero is -35± dB (MDA, 2016). A summary of radar parameters for all 14 polarimetric images is shown in the Table 3.1. Note that the daily temperature observations were retrieved from the Déline meteorological station (65°12´ N and 123°26´) from the historical climate database of Environment and Climate Change Canada. The maximum, minimum and mean near-surface air temperatures help with interpreting the snow cover and ice melting/freezing conditions, which may influence the backscatter and scattering mechanisms. For instance, high near-surface air temperature (over 0 °C) will cause wet snow cover and melting on the ice surface. A decrease can be observed in backscatter due to the signal being absorbed by the wet snow cover and specular reflection over the water or ponds on the lake ice surface (Duguay et al., 2002).

Table 3.1: Summary of RADARSAT-2 acquisition dates, modes and range of incidence angles. Also shown are the maximum, minimum and mean near-surface air temperatures recorded at the closest meteorological station (Déline, NWT)

Data Number	Time	Date	Year	Pass Orbits	Beam Swath Position	Near Incidence Angle (degrees)	Far Incidence Angle (degrees)	Near Range Resolution (m)	Far Range Resolution (m)	Max Temp (°C)	Min Temp (°C)	Mean Temp (°C)
Break-up Period												
1	01:36	Jun 16	2015	ASC	SQ18W	36.7	39.5	22.5	21.2	19.0	1.3	10.2
2	01:07	Jun 17	2015	ASC	SQ1W	17.5	21.2	30.0	24.9	16.7	7.3	12.0
3	14:46	Jun 17	2015	DES	SQ11W	29.5	32.6	18.3	16.7	16.7	7.3	12.0
4	14:29	Jun 21	2015	DES	SQ21W	39.5	42.1	21.2	20.1	24.4	5.2	14.8
5	14:42	Jun 24	2015	DES	SQ14W	32.7	35.7	24.9	23.1	26.6	9.7	18.2
6	01:15	Jun 27	2015	ASC	SQ5W	22.5	26.0	23.6	20.6	22.4	12.1	17.3
7	14:54	Jun 27	2015	DES	SQ6W	23.7	27.2	22.4	19.8	22.4	12.1	17.3
8	01:28	Jun 30	2015	ASC	SQ13W	31.7	34.7	25.7	23.7	20.6	13.4	17.0
Freeze-up Period												
9	01:15	Nov 18	2015	ASC	SQ5W	22.5	26.0	23.6	20.6	-14.7	-20.6	-17.7
10	14:54	Nov 18	2015	DES	SQ7W	24.9	28.3	21.4	19.0	-14.7	-20.6	-17.7
11	01:28	Nov 21	2015	ASC	SQ13W	31.7	34.7	25.7	23.7	-13.6	-19.0	-16.3
12	01:11	Nov 25	2015	ASC	SQ2W	19.0	22.7	27.7	23.4	-12	-19.8	-15.9
13	14:50	Nov 25	2015	DES	SQ9W	27.2	30.5	19.7	17.8	-12	-19.8	-15.9
14	01:24	Nov 28	2015	ASC	SQ11W	29.5	32.6	18.3	16.7	-3.3	-13.4	-8.4

3.3.2 Methods

3.3.2.1 Data pre-processing and processing steps

RADARSAT-2 Wide SQ-pol images were employed in this study. The distance measured in Single Look Complex product in slant range was converted to ground range. The number of looks for each image was calculated, and multi-looking was implemented to take the average of the corresponding single-looks in the azimuth direction. The number of looks for these 14 images are typically from 3 to 5, which is not large enough for reducing the noise effect (Lee & Pottier, 2009). Additional polarimetric speckle filtering was considered to further reduce the noise. The polarimetric refined Lee speckle filter (Lee, Grunes, & Grandi, 1999) was employed for weighted averaging covariance matrix from the neighboring pixels. The refined Lee filter preserves the polarimetric properties and statistical properties, avoiding crosstalk between polarization channels, and preserves the scattering features, edge sharpness, and point targets (Lee, Grunes, & Grandi, 1999). The above pre-processing steps, including the extraction of polarimetric parameters, were performed in the Sentinel Application Platform (SNAP) version 4.0.

The Entropy-alpha Wishart classifier proposed by Lee et al. (1999) was used to classify the images at the first stage. It initialized the original classes based on the entropy and alpha angle zones proposed by Cloude & Pottier (1997), and only used the covariance matrix for maximizing the likelihood based on the complex Wishart distribution (Lee et al., 1999). The Entropy-alpha Wishart classifier was summarized in Section 3.3.2.2. Since Entropy-alpha Wishart classifier assumed priors for all classes equal, the posterior did not incorporate the prior knowledge. To fulfill the prior probability by considering neighboring pixels, the supervised Markov Random Field (MRF) was implemented on top of Entropy-alpha Wishart classifier, which is detailed in Section 3.3.2.3. The classification results from Entropy-alpha Wishart classifier was used as labels for training the MRF. The features for MRF classifier included the co-pol and cross-pol multi-looked intensities, coherency matrix, Freeman-Durden decomposition results as well as two secondary physical parameters: entropy and alpha angle. The entropy represents the disorder of the scattering, and the alpha angle, directly related to three eigenvectors, can identify the dominant scattering mechanisms. After all features were extracted and labels were generated from Entropy-alpha Wishart classifier, 10 cross validation was used for training and testing: each image was

separated to 10 folds, 9 folds of the image were used for training and the rest fold was retained for testing. In the training process, the prior was calculated through the joint probability by considering the clique potential; the parameters for the individual distribution of input features were estimated by method of moments. In the testing step for each cross validation, the likelihood was determined by product of the probabilities of individual features with the parameters estimated in the training process. The posterior was determined by the multiplication of the likelihood and the prior based on the Bayes' Theorem. The class with highest posterior will be selected as the output. The final classes were merged according to the merging and termination criteria proposed in Section 3.4.2.4. The overall processing chain of feature extraction, label generation and MRF classifier are illustrated in Figure 3.2.

The accuracy assessment was conducted by an ice analyst of Canadian Ice Service at Environment and Climate Change Canada (ECCC). The open water and ice polygons were delineated through manual (visual) identification based on the RADARSAT-2 polarimetric images. These delineations of open water and ice were digitized as regions of interest and further projected into an image with the same size as multilooked images. The accuracy assessment will be detailed in Section 3.3.2.5.

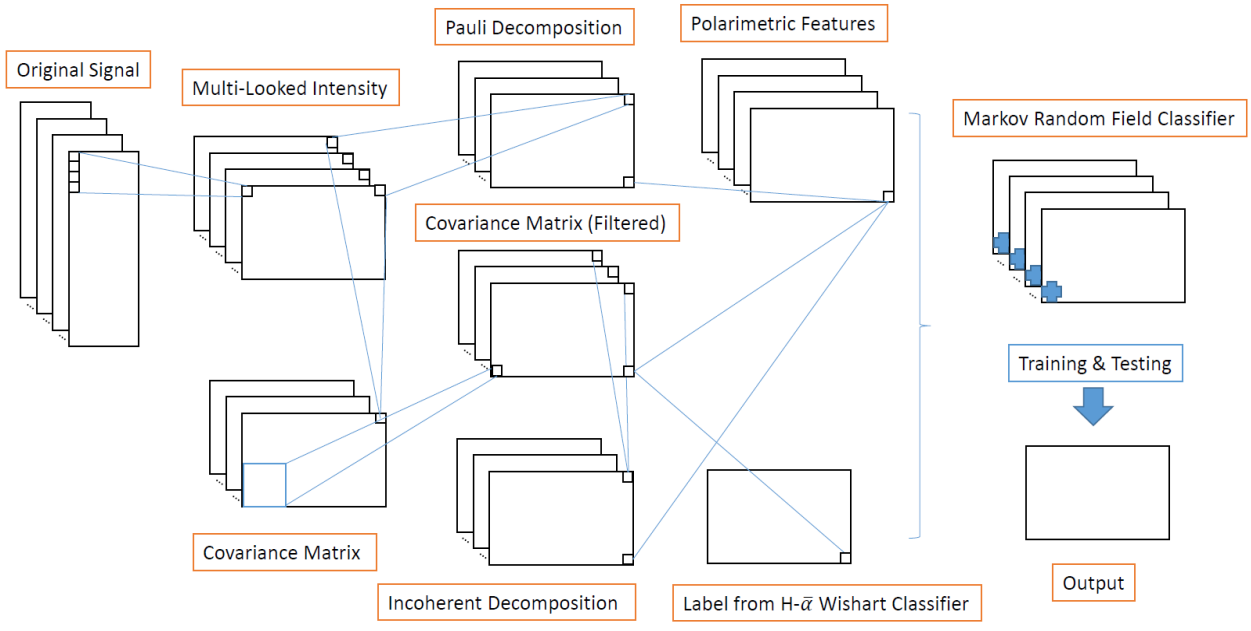

Figure 3.2: The processing chain of feature extraction, label generation and MRF classifier.

3.3.2.2 Entropy-Alpha Angle Complex Wishart Classifier

Since radar signals were averaged through multilooking and speckle filtering, only the covariance matrix or coherency matrix could be employed for analyzing the incoherent targets. The covariance matrix and coherency matrix are complex Wishart distributed:

$$f(\boldsymbol{C}|N,\boldsymbol{\Sigma}) = \frac{N^{Nn}|\boldsymbol{C}|^{N-n}}{I(N,n)|\boldsymbol{\Sigma}|^{N}} e^{-N\cdot Trace(\boldsymbol{\Sigma}^{-1}\boldsymbol{C})} \tag{3.3}$$

where $\boldsymbol{C}$ is the covariance matrix variable, N is the number of looks, n is the dimension of the target vector, and $\boldsymbol{\Sigma}$ is the positive definite covariance matrix of the variable $\boldsymbol{C}$.

The unsupervised H-alpha complex Wishart classifier proposed by Lee et al. (1999) aims to maximize the posterior: $P(\omega|\boldsymbol{X})$ by applying the Bayes' rule:

$$P(\omega|\boldsymbol{X}) = \frac{P(\boldsymbol{X}|\omega)P(\omega)}{P(\boldsymbol{X})} \tag{3.4}$$

where ω represents the classes or labels of a scattering vector $\boldsymbol{k}$. Since $P(\boldsymbol{X})$ is an independent constant number, $\boldsymbol{k}$ belongs to class $\omega = i$, if $P(\boldsymbol{X}|\omega = i)P(\omega = i) > P(\boldsymbol{X}|\omega = j)P(\omega = j)$, for all $j \neq i$. The $f(\boldsymbol{C}|N,\boldsymbol{\Sigma})$ is the model used for the likelihood of a feature given a label, $P(\boldsymbol{X}|\omega)$. Maximizing the posterior is equivalent to minimizing the negative natural logarithm of the posterior. The maximum a posterior (MAP) function is given by:

$$MAP = argmin \sum N \cdot Trace(\boldsymbol{\Sigma}^{-1}\boldsymbol{C}) + N\, ln(|\boldsymbol{\Sigma}|) - ln(P(\omega)) \tag{3.5}$$

Since the prior $P(\omega)$ has an unknown probability, Lee et al. (1999) assumed priors to be equal, thus this classifier now is equivalent to the maximum likelihood estimation instead of a MAP classifier. This maximum likelihood function is called a loss function

$$L(\omega,\boldsymbol{\Sigma},\boldsymbol{C}) = argmin \sum Trace(\boldsymbol{\Sigma}^{-1}\boldsymbol{C}) + \ln\left(\left|\left|\boldsymbol{\Sigma}\right|\right|\right) \tag{3.6}$$

Therefore, the pixels are assigned to the class with minimum of loss to achieve the overall minimum of the loss function.

The Entropy-alpha Wishart classification is a typical unsupervised classification, which uses the expectation maximization (EM) as its optimization algorithm. The initial classes are assigned according to the admissible alpha and entropy zones as shown in Figure 3.3. Once the initial classes are prepared, the following procedure involves two iterative steps. In the expectation step, for each class, the covariance matrix $\mathbf{\Sigma}$ can be estimated through the method of moments; in the second maximization step, it reassigns the pixels to the corresponding classes with the lowest loss for minimizing the entire loss function. These two steps are iterated until the loss function converges or the termination criterion is met, which will be presented in Section 3.3.2.4.

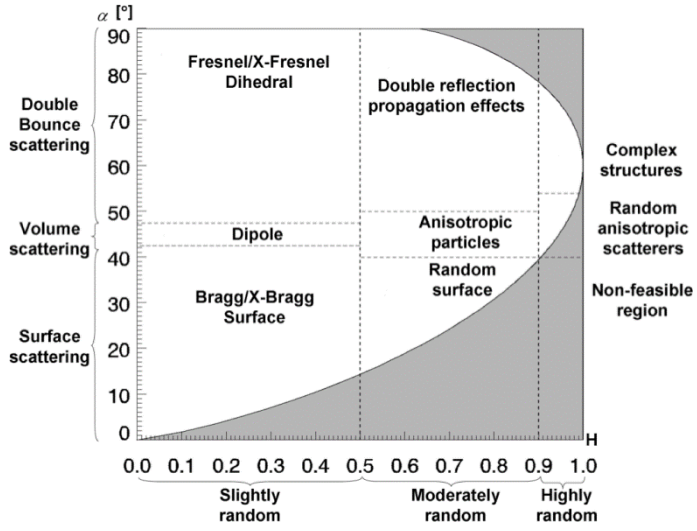

Figure 3.3: Entropy and alpha angle zones (Cloude & Pottier, 1997)

3.3.2.3 Markov Random Field

Since the Entropy-alpha Wishart classifier assumes that the priors for each class are equal at any time, the objective did not incorporate the prior knowledge. However, regions or clusters are often homogeneous with neighboring pixels having similar properties and features. To fulfill the knowledge of neighboring pixels and prior probability, the Markov properties are considered due to the conditional independence of any two non-adjacent pixels. Therefore, MRF, a graphical model of a joint probability distribution by considering the neighboring pixels, was employed.

Let $s = (i, j)$ denote the pixel at i, j in the graph S. For each pixel s in the image, it has a feature vector X_s; thus, we have the feature $\boldsymbol{X} = \{\boldsymbol{X}_s, s \in S\}$ for the whole image. Each pixel s has its corresponding label $\omega_s \in \Lambda$, where the Λ is the range of the classes the label can choose from. For the whole image, we have $\boldsymbol{\omega} = \{\omega_s, s \in S\}$. According to the Bayes' theorem, the posteriori $P(\boldsymbol{\omega}|\boldsymbol{X})$ is given by

$$P(\boldsymbol{\omega}|\boldsymbol{X}) = \frac{P(\boldsymbol{X}|\boldsymbol{\omega})P(\boldsymbol{\omega})}{P(\boldsymbol{X})} \tag{3.7}$$

which measures the probability of labelling given the observed feature $\boldsymbol{X}$. The objective of classifying the whole image is to find an optimal labelling which maximizes the $P(\boldsymbol{\omega}|\boldsymbol{X})$ by a MAP estimation. Since $P(\boldsymbol{X})$ is a constant and independent of any classes to be chosen, MAP is equivalent to

$$\arg max\, P(\boldsymbol{\omega}|\boldsymbol{X}) \propto P(\boldsymbol{X}|\boldsymbol{\omega})P(\boldsymbol{\omega}) \tag{3.8}$$

The labelling field can be modeled as a MRF if all the $\omega_s \in \Lambda: P(\boldsymbol{\omega}) > 0$; and if for every $s \in S,\ \omega_s \in \Lambda$, we have

$$P(\omega_s|\omega_r, r \neq s) = P(\omega_s|\omega_r, r \in N_s) \tag{3.9}$$

where the neighbour set N_s is defined as the surrounding pixels of a pixel s. Besides the neighbours, a subset C is defined as a clique if every pair of pixels in C are neighbours. A clique C_n containing n pixels is called an nth order clique, thus the set of cliques is denoted as

$$C = C_1 \cup C_2 \cup \cdots \cup C_k \tag{3.10}$$

The first order and second order clique are named after singleton and doubleton, respectively.

According to the Hammersley-Clifford theorem, the joint probability $P(\boldsymbol{\omega})$ of a MRF follows a Gibbs distribution:

$$P(\boldsymbol{\omega}) = \frac{1}{Z} e^{-U(\boldsymbol{\omega})} = \frac{1}{Z} e^{-\sum_{c \in C} V_c(\boldsymbol{\omega})} \tag{3.11}$$

where $Z = \sum_{\boldsymbol{\omega} \in \Omega} \exp(V_c(\boldsymbol{\omega}))$ is the normalizing constant, and Ω denotes all the possible labelling conditions, the $V_c(\boldsymbol{\omega})$ denotes the clique potential of clique C, the $U(\boldsymbol{\omega})$ is called the energy function, which requires taking the sum of potentials of all cliques:

$$U(\boldsymbol{\omega}) = \sum_{c \in C} V_c(\boldsymbol{\omega}) = \sum_{C_1} V_{C_1}(\omega) + \sum_{C_2} V_{C_2}(\omega) + \cdots \tag{3.12}$$

In this case, we do not have any hidden layer within the Markov model. Only the first order (singletons) and second order cliques (doubletons) are considered for determining the clique potential V_c, which are given by

$$V_{C_1}(\omega_s, r \in N_s) = \begin{cases} 0 & if \ \ \omega_s \\ \varepsilon & else \end{cases} \tag{3.13}$$

$$V_c(\omega_s, \omega_r, r \in N_s) = \begin{cases} \beta & if \ \ \omega_s \neq \omega_r \\ -\beta & if \ \ \omega_s = \omega_r \end{cases} \tag{3.14}$$

where $\varepsilon, \beta > 0$ is a parameter tuning the weights of contributions of corresponding clique potentials.

The likelihood $P(\boldsymbol{X}|\boldsymbol{\omega})$ is determined by the probability density function of the corresponding features. For instance, the multi-looked intensity from heterogeneous scattering should be K-distributed; the PDF can be given by

$$f(I_h|\mu = 1, v, N) = \frac{2(Nv)^{\frac{N+v}{2}} I_h^{\frac{N+v}{2}-1}}{\Gamma(N)\Gamma(v)} \mathrm{K}_{v-N}(2\sqrt{NvI_h}) \tag{3.15}$$

The covariance matrix is complex Wishart distributed as presented in Equation 3.3. The decomposition parameters are assumed to be Gaussian distributed (Lee & Pottier, 2009). The parameters in these PDFs can be estimated through the method of moments.

3.3.2.4 Class Merging and Termination Criteria

The number of classes provided by the classifiers is generally more than 2 classes: ice and open water; therefore, class merging and termination criteria are needed for combining the classes that indicate the same target and decreasing the number of classes. The number of classes cannot be specified due to the fact that open water or different ice types may have various manifestations in the space of polarimetric features. For instance, the surface roughness of water may differ over time, when water is disturbed by wind creating waves. Therefore, scattering from surface water may have significant difference in polarization and polarimetric parameters; more than one class should be reserved for water. The overflowing classes can be merged according to the following proposed algorithms. The dispersion is introduced at this stage to measure distance between classes. The dispersion within class i, D_{ii} is defined as the averaged distance from the covariance matrix $\boldsymbol{C}$ of each pixel in class i to the sum of covariance matrix $\boldsymbol{\Sigma_i}$ of the class i:

$$D_{ii} = \frac{1}{n_i}\sum_{k=1}^{K_i}\left[Trace\left(\boldsymbol{\Sigma_i}^{-1}\boldsymbol{C_k}\right) + \ln(|\boldsymbol{\Sigma_i}|)\right] = \ln(|\boldsymbol{\Sigma_i}|) + n \tag{3.16}$$

where K_i is the number of the pixels in the class i, n=3 is the dimension of the covariance matrix. The distance between two classes D_{ij} is defined as

$$D_{ij} = \frac{1}{2}\left\{\frac{1}{n_i}\sum_{k=1}^{K_i}\left[Trace\left(\boldsymbol{\Sigma_j}^{-1}\boldsymbol{C_k}\right) + \ln\left(|\boldsymbol{\Sigma_j}|\right)\right] + \frac{1}{n_i}\sum_{k=1}^{K_j}\left[Trace\left(\boldsymbol{\Sigma_i}^{-1}\boldsymbol{C_k}\right) + \ln(|\boldsymbol{\Sigma_i}|)\right]\right\}$$

$$= \frac{1}{2}\left\{\ln(|\boldsymbol{\Sigma_i}|) + \ln\left(|\boldsymbol{\Sigma_j}|\right) + Trace\left(\boldsymbol{\Sigma_i}^{-1}\boldsymbol{\Sigma_j}\right) + Trace\left(\boldsymbol{\Sigma_j}^{-1}\boldsymbol{\Sigma_i}\right)\right\} \tag{3.17}$$

Parameter R_{ij}, originally proposed by Davies & Bouldin (1979), is always provides an indication of the separation (Lee, et al., 1999):

$$R_{ij} = \frac{D_{ii}+D_{jj}}{D_{ij}} \tag{3.18}$$

where $R_{ij} \in (0, 2]$. When R_{ij} is close to 2, the two classes i and j is likely to be merged; when it is close to 0, the two classes are highly separated.

The termination criterion can be obtained by an optimization problem defined as

$$\arg min\, R = \arg min \left\{ \frac{1}{n_\Lambda} \sum_{i=1}^{n_\Lambda} R_{max-i} \right\} \tag{3.19}$$

where n_Λ is the number of classes, and R_{max-i} is the maximum separation of the class i, defined as

$$R_{max-i} = \max_j (R_{ij}), i \neq j \tag{3.20}$$

The procedure is as follows: the initial number of classes n_Λ is set as 9; calculate R for n_Λ; deduct the number of classes: $n_\Lambda = n_\Lambda - 1$; merge the two classes with the maximum R_{ij} value. If the current n_Λ is larger than 1, go back to the second step to calculate R, iteratively until the current n_Λ equals to 1.

3.3.2.5 Accuracy Assessment

The accuracy assessment was conducted by an ice analyst of CIS at ECCC. The open water and ice polygons were delineated through manual (visual) identification based on the hard copy of RADARSAT-2 polarimetric multi-looked images, which are the same images for the classification. These delineations of open water and ice were digitized as samplings of regions of interest (ROI) and further projected into the multi-looked images with the same size. As shown on the left of Figure 3.4, the blue spots were the ROI of open water and yellow spots were the ROI of ice, which were located within the original delineated open water and ice polygons. When we had the classification results from either Entropy-alpha Wishart classifier or MRF classifier as shown on the right of Figure 3.4, we summed the pixels within the ROI that were correctly classified and this number was divided by the overall pixels in the ROI to achieve the accuracy. For instance, if the pixels in blue ROIs was classified as open water shown in black on the right of Figure 3.4, they were marked as correctly classified pixels. If pixels within orange ROIs were identified as lake ice in the classification results, they were marked as correctly classified pixels. The overall accuracy was achieved by summing all the correctly classified pixels and dividing it by all the pixels within all ROIs.

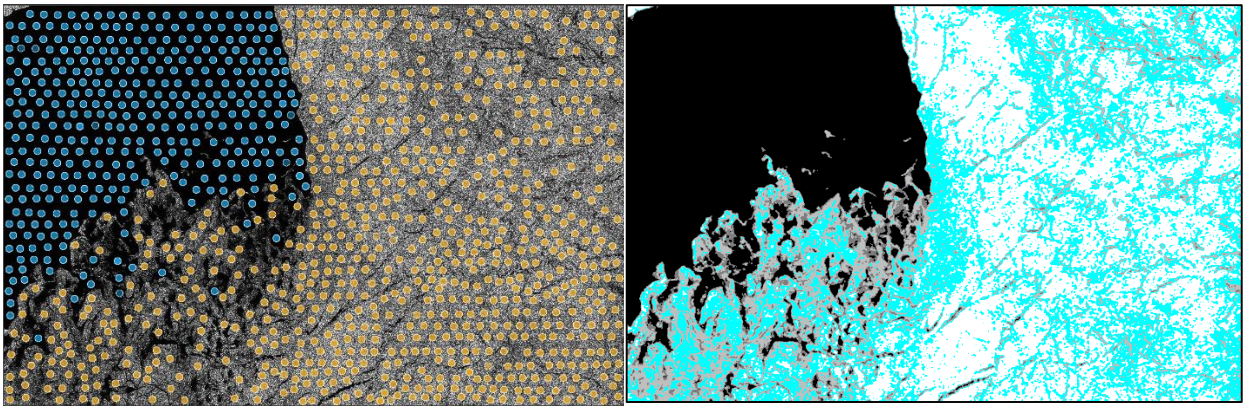

Figure 3.4: The image on the left shows the digitized ROI, which sampled the delineation of open water and ice by the ice analyst from CIS. The blue ROI represents open water, and orange ROI represents ice. The image on the right shows an example of classification results. The black corresponds open water area, and the rest of colored area correspond lake ice.

3.4 Results and Discussion

The multi-looked intensities are presented in Figures 3.5-3.18 through the Pauli decomposition (A), the diagonal elements of the coherency matrix (B), the powers of surface, double bounce and volume scattering from Freeman-Durden decomposition (C) as well as entropy (D) and alpha angle (E). The labels generated from the Entropy-alpha Wishart classifier (G) and the corresponding legend (F) for the classification results from the MRF classifier (H) are also shown in these figures. The characteristics of features and their physical meanings as well as accuracy assessments of the classifier are presented below.

RS2-SLC-SQ18W-ASC-16-Jun-2015_01.36

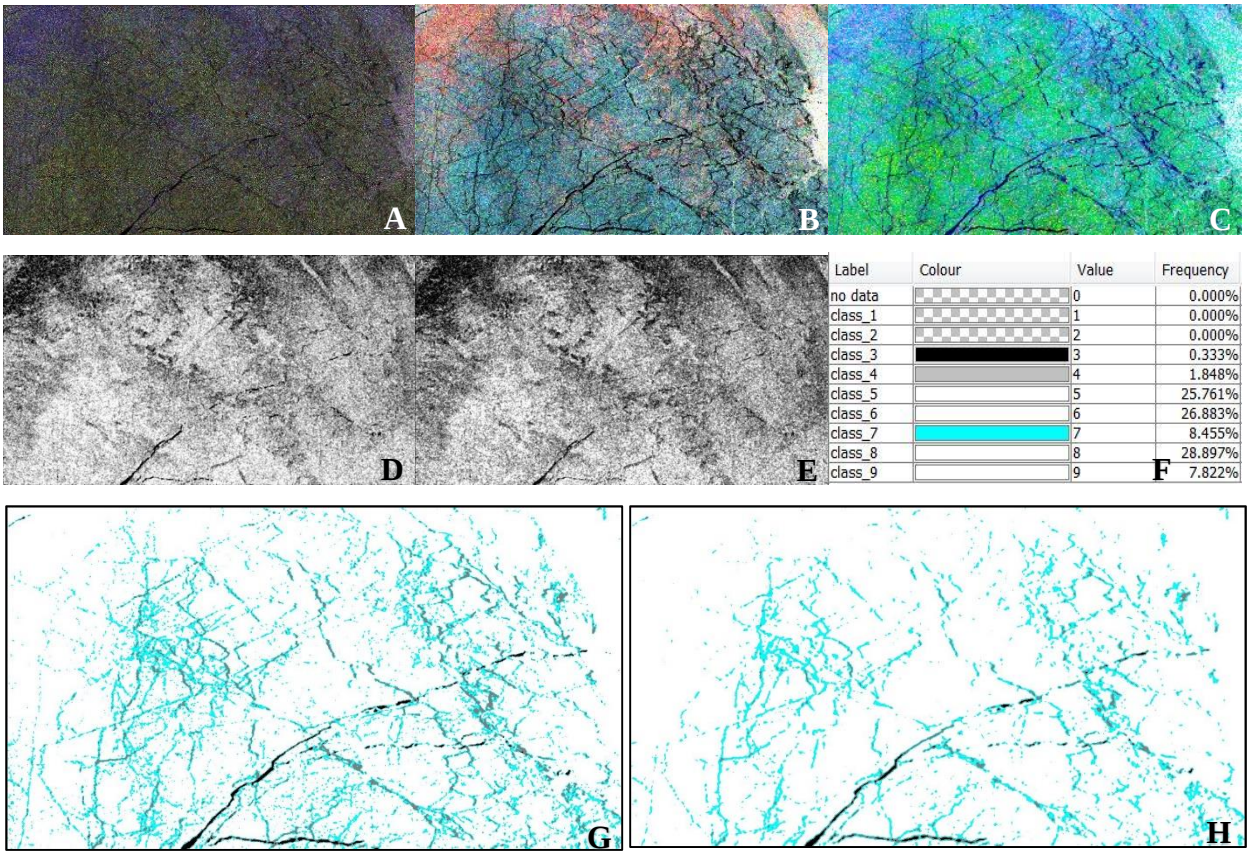

Figure 3.5: This image was acquired during the break-up period on June 16, 2015 at ascending orbit. See Table 3.1 for further details on image acquisition characteristics. A: Three features from Pauli decomposition (Red: HH-VV, Green: 2HV, Blue: HH+VV); B: Coherency matrix (Red: T11, Green: T22, Blue: T33); C: Surface, double bounce and volume scattering from Freeman-Durden Decomposition (Red: double-bounce, Green: volume, Blue: surface); D: Entropy (H); E: Alpha angle; F: Legend of labels and color codes from H-alpha classifier; G: Labels from H-alpha classifier developed by Lee et al. (1999); H: Results from the MRF classifier.

RS2-SLC-SQ1W-ASC-17-Jun-2015_01.07

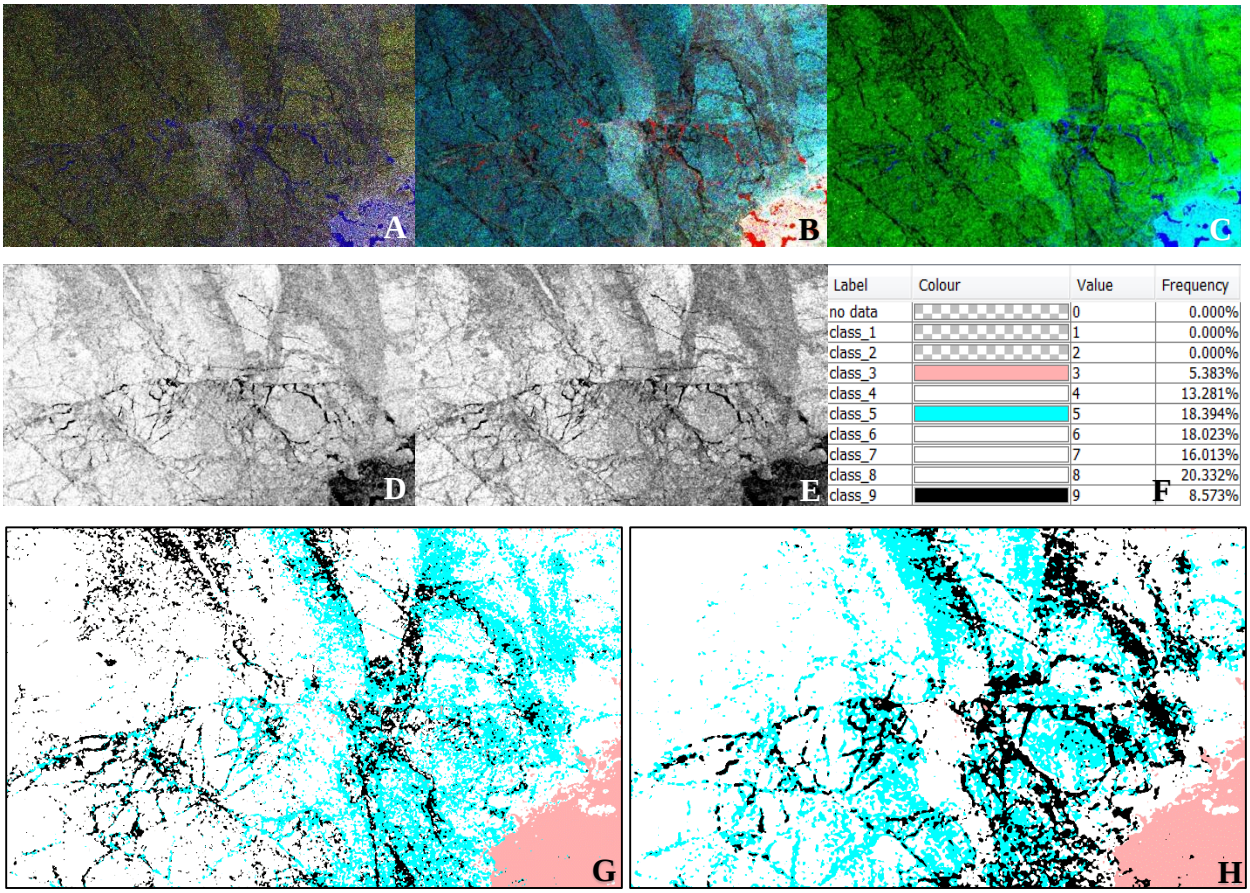

Figure 3.6: This image was acquired during the break-up period on June 17, 2015 at ascending orbit. See Table 3.1 for further details on image acquisition characteristics. A: Three features from Pauli decomposition (Red: HH-VV, Green: 2HV, Blue: HH+VV); B: Coherency matrix (Red: T11, Green: T22, Blue: T33); C: Surface, double bounce and volume scattering from Freeman-Durden Decomposition (Red: double-bounce, Green: volume, Blue: surface); D: Entropy (H); E: Alpha angle; F: Legend of labels and color codes from H-alpha classifier; G: Labels from H-alpha classifier developed by Lee et al. (1999); H: Results from the MRF classifier.

RS2-SLC-SQ11W-DES-17-Jun-2015_14.46

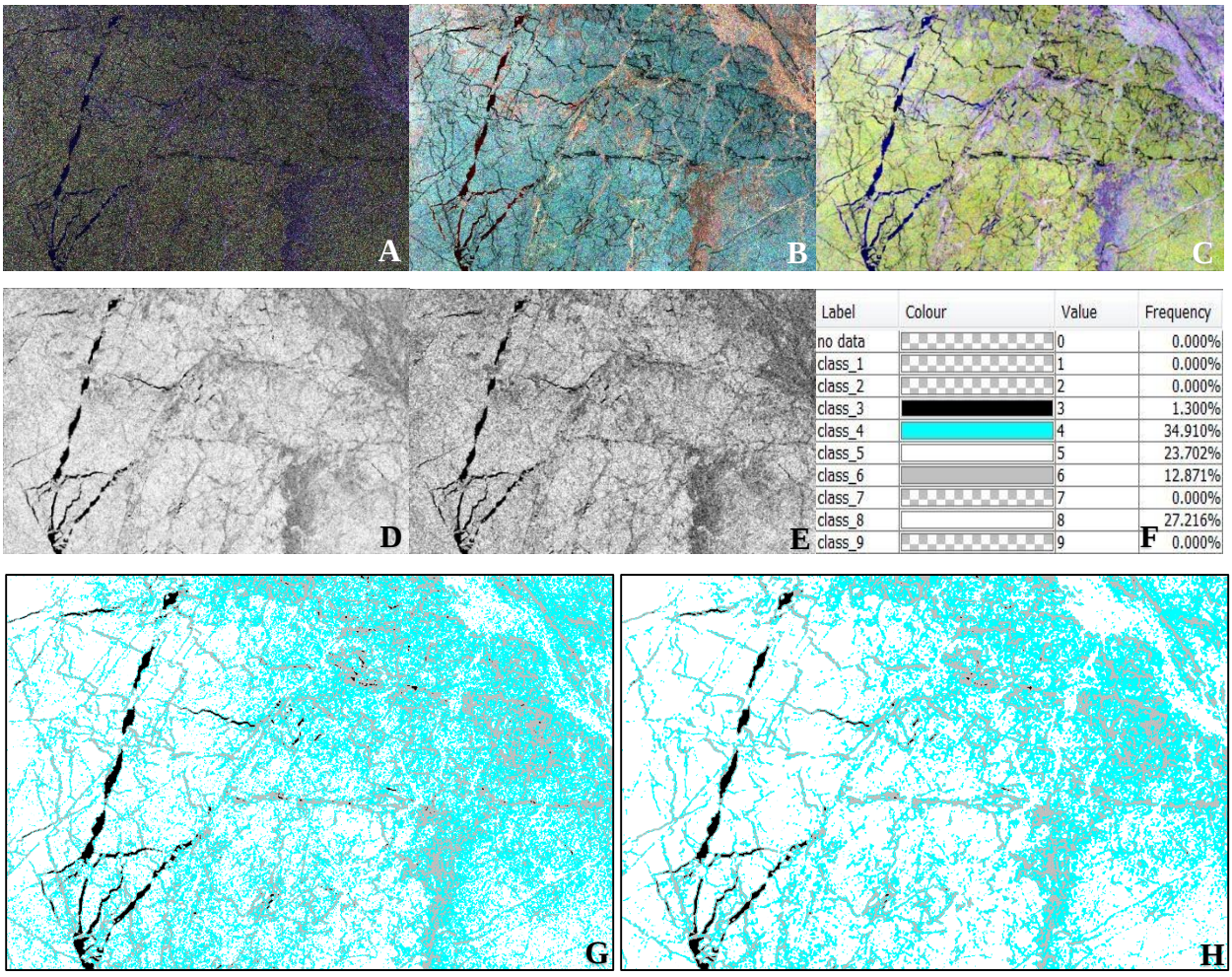

Figure 3.7: This image was acquired during the break-up period on June 17, 2015 at descending orbit. See Table 3.1 for further details on image acquisition characteristics. A: Three features from Pauli decomposition (Red: HH-VV, Green: 2HV, Blue: HH+VV); B: Coherency matrix (Red: T11, Green: T22, Blue: T33); C: Surface, double bounce and volume scattering from Freeman-Durden Decomposition (Red: double-bounce, Green: volume, Blue: surface); D: Entropy (H); E: Alpha angle; F: Legend of labels and color codes from H-alpha classifier; G: Labels from H-alpha classifier developed by Lee et al. (1999); H: Results from the MRF classifier.

RS2-SLC-SQ21W-DES-21-Jun-2015_14.29

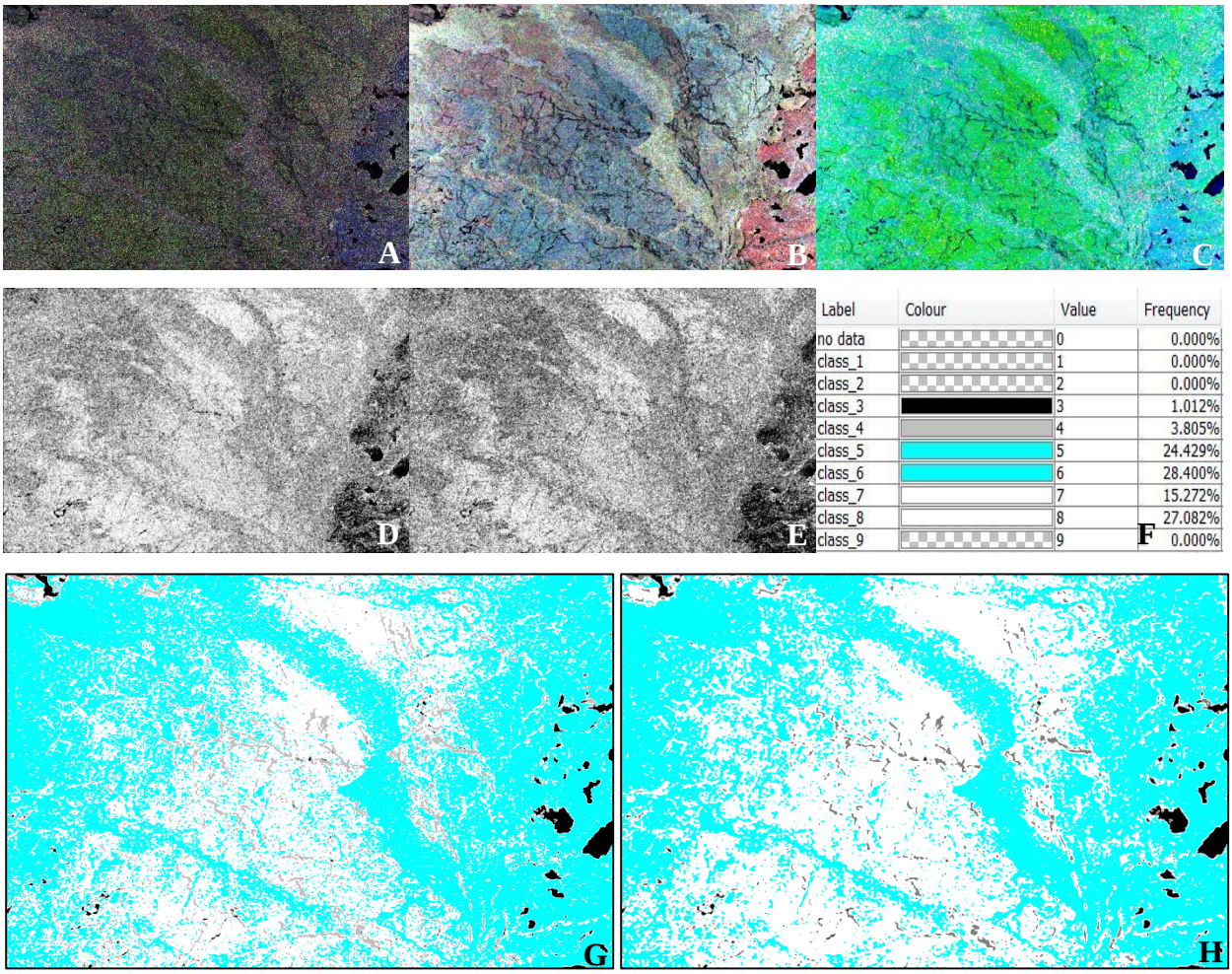

Figure 3.8: This image was acquired during the break-up period on June 21, 2015 at descending orbit. See Table 3.1 for further details on image acquisition characteristics. A: Three features from Pauli decomposition (Red: HH-VV, Green: 2HV, Blue: HH+VV); B: Coherency matrix (Red: T11, Green: T22, Blue: T33); C: Surface, double bounce and volume scattering from Freeman-Durden Decomposition (Red: double-bounce, Green: volume, Blue: surface); D: Entropy (H); E: Alpha angle; F: Legend of labels and color codes from H-alpha classifier; G: Labels from H-alpha classifier developed by Lee et al. (1999); H: Results from the MRF classifier.

RS2-SLC-SQ14W-DES-24-Jun-2015_14.42

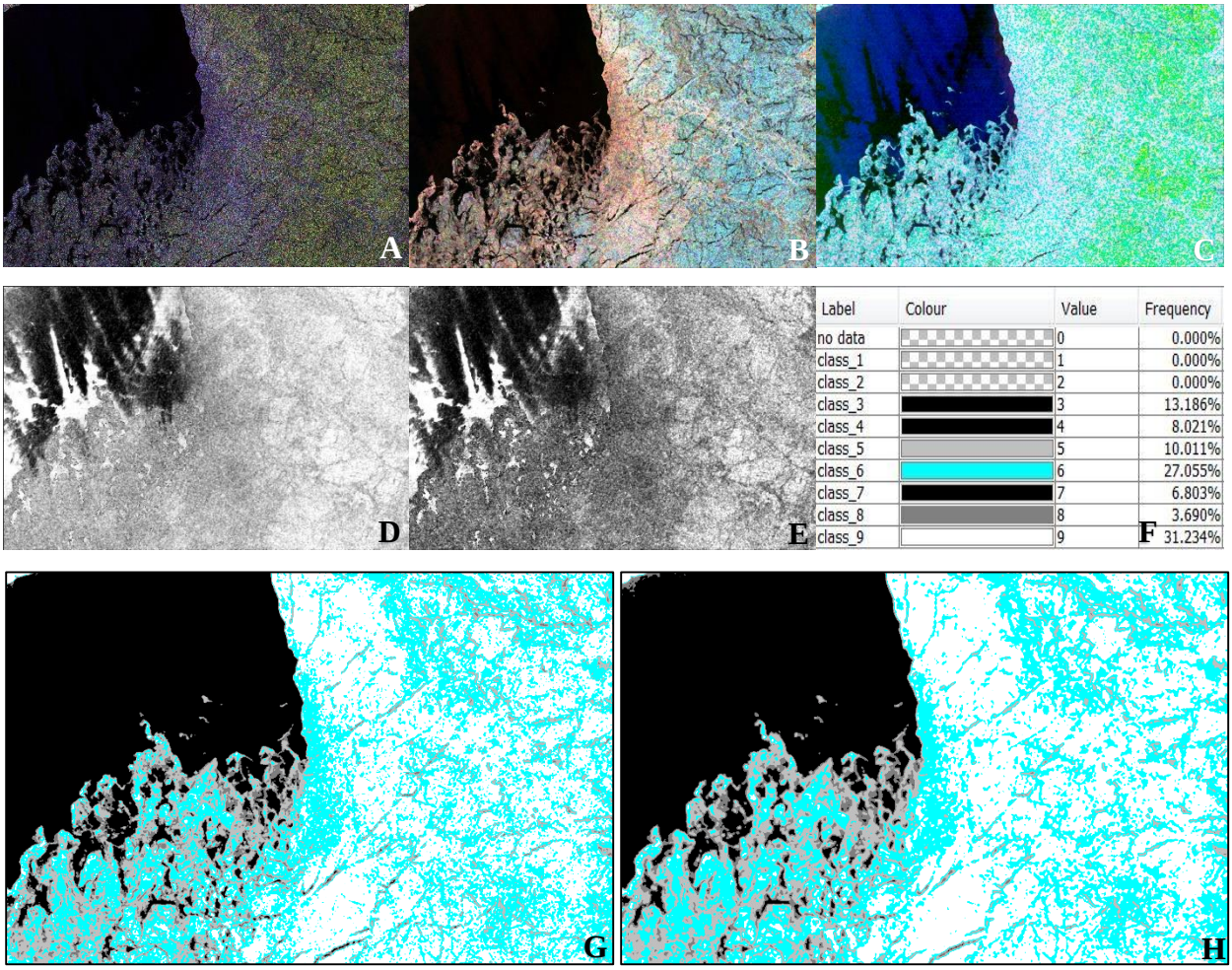

Figure 3.9: This image was acquired during the break-up period on June 24, 2015 at descending orbit. See Table 3.1 for further details on image acquisition characteristics. A: Three features from Pauli decomposition (Red: HH-VV, Green: 2HV, Blue: HH+VV); B: Coherency matrix (Red: T11, Green: T22, Blue: T33); C: Surface, double bounce and volume scattering from Freeman-Durden Decomposition (Red: double-bounce, Green: volume, Blue: surface); D: Entropy (H); E: Alpha angle; F: Legend of labels and color codes from H-alpha classifier; G: Labels from H-alpha classifier developed by Lee et al. (1999); H: Results from the MRF classifier.

RS2-SLC-SQ5W-ASC-27-Jun-2015_01.15

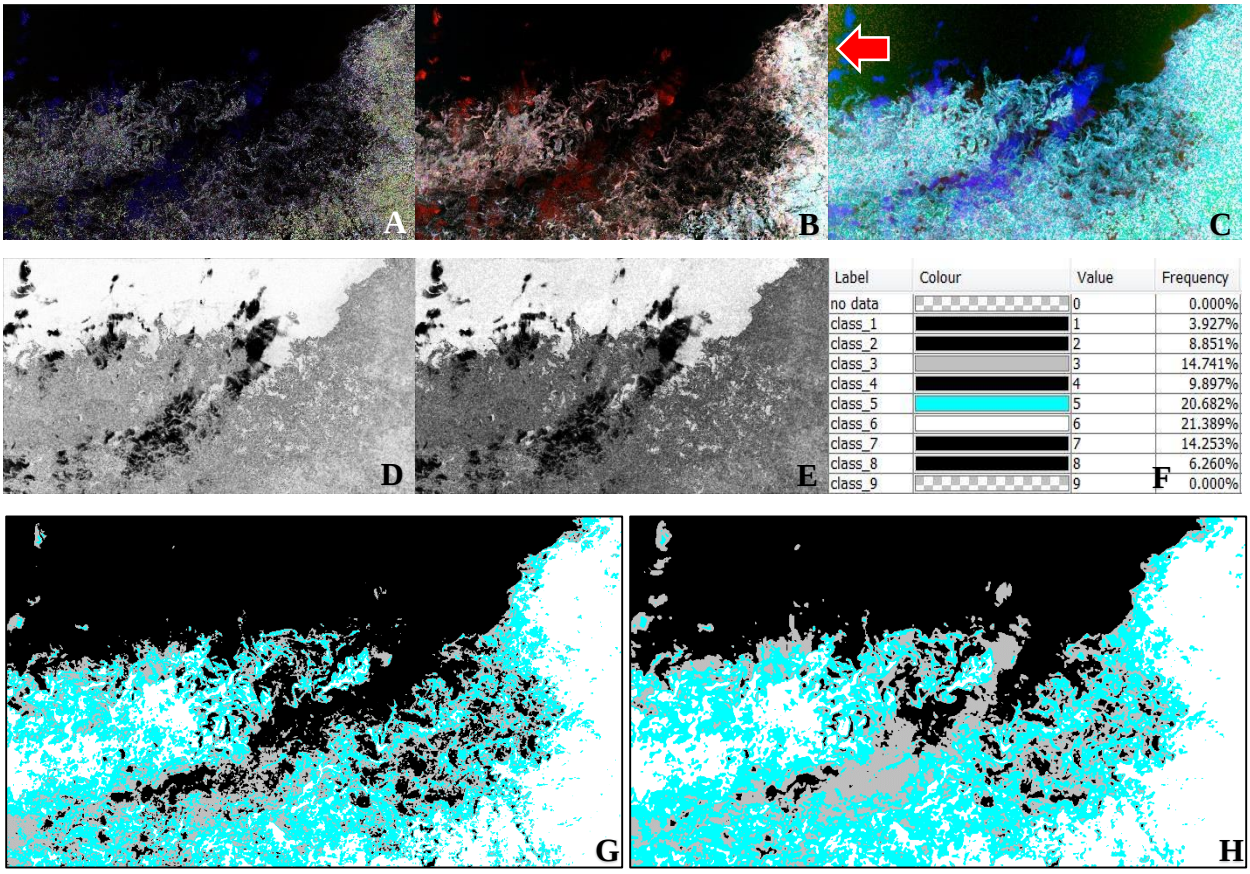

Figure 3.10: This image was acquired during the break-up period on June 27, 2015 at ascending orbit. See Table 3.1 for further details on image acquisition characteristics. A: Three features from Pauli decomposition (Red: HH-VV, Green: 2HV, Blue: HH+VV); B: Coherency matrix (Red: T11, Green: T22, Blue: T33); C: Surface, double bounce and volume scattering from Freeman-Durden Decomposition (Red: double-bounce, Green: volume, Blue: surface); D: Entropy (H); E: Alpha angle; F: Legend of labels and color codes from H-alpha classifier; G: Labels from H-alpha classifier developed by Lee et al. (1999); H: Results from the MRF classifier. Note that the red area pointed by red arrow cannot be interpreted as double-bounce scattering dominating on open water surface.

RS2-SLC-SQ6W-DES-27-Jun-2015_14.54

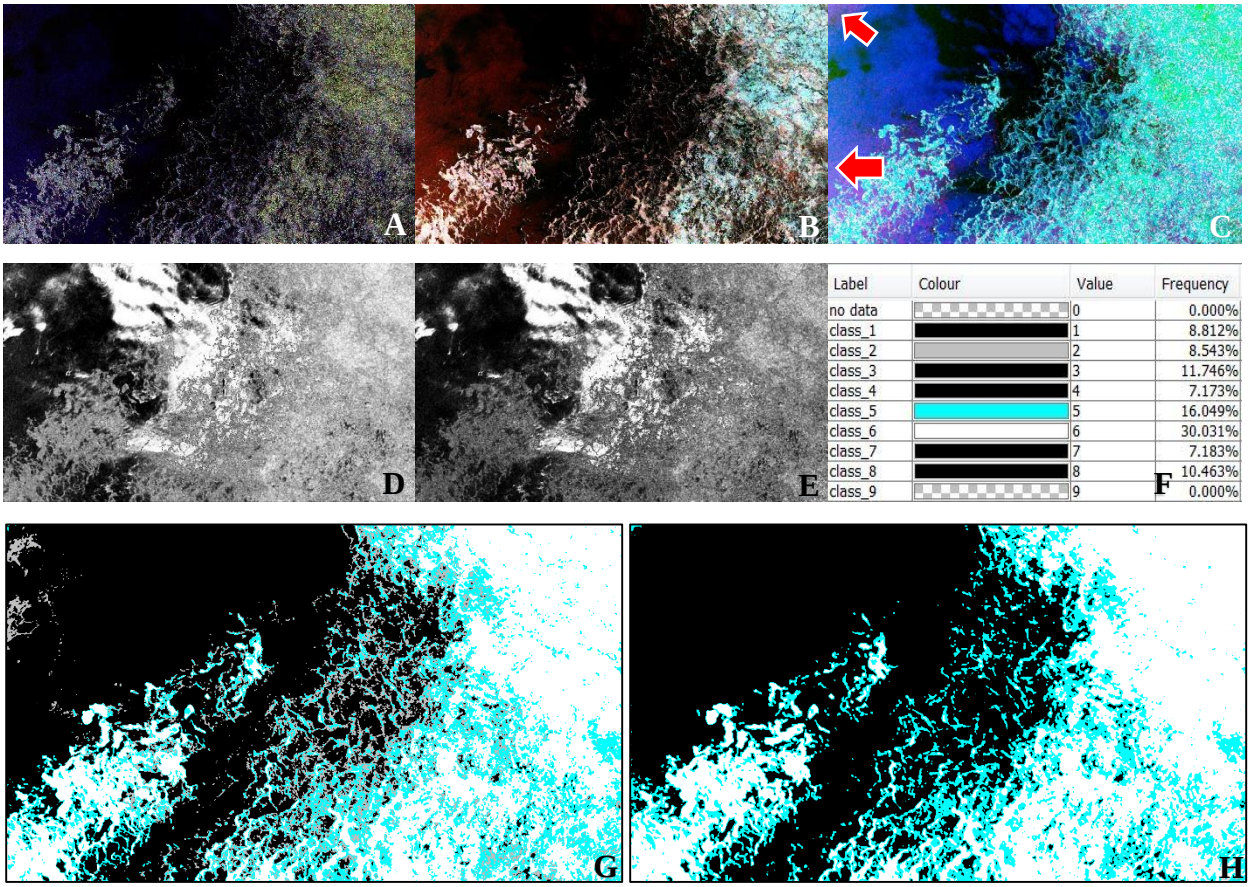

Figure 3.11: This image was acquired during the break-up period on June 27, 2015 at descending orbit. See Table 3.1 for further details on image acquisition characteristics. A: Three features from Pauli decomposition (Red: HH-VV, Green: 2HV, Blue: HH+VV); B: Coherency matrix (Red: T11, Green: T22, Blue: T33); C: Surface, double bounce and volume scattering from Freeman-Durden Decomposition (Red: double-bounce, Green: volume, Blue: surface); D: Entropy (H); E: Alpha angle; F: Legend of labels and color codes from H-alpha classifier; G: Labels from H-alpha classifier developed by Lee et al. (1999); H: Results from the MRF classifier. Note that the red area pointed by red arrow cannot be interpreted as double-bounce scattering dominating on open water surface.

RS2-SLC-SQ13W-ASC-30-Jun-2015_01.28

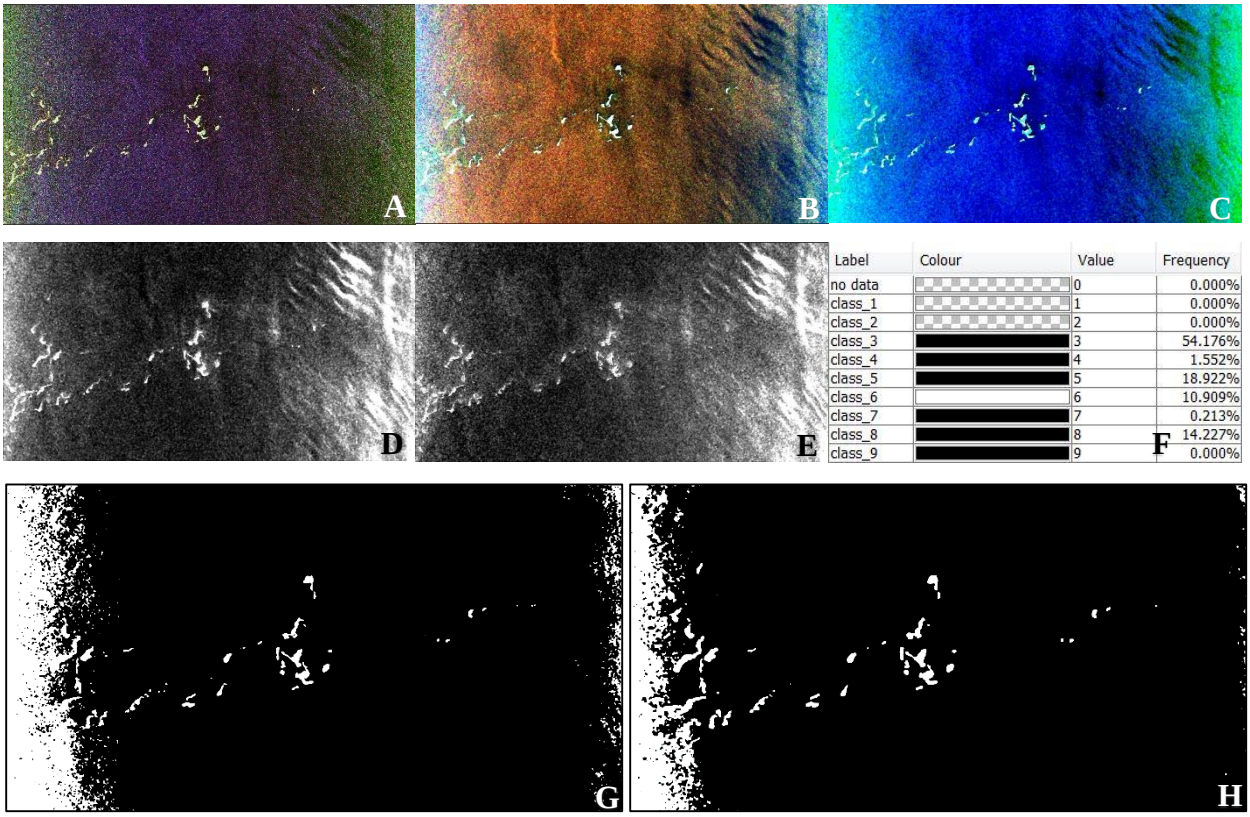

Figure 3.12: This image was acquired during the break-up period on June 30, 2015 at ascending orbit. See Table 3.1 for further details on image acquisition characteristics. A: Three features from Pauli decomposition (Red: HH-VV, Green: 2HV, Blue: HH+VV); B: Coherency matrix (Red: T11, Green: T22, Blue: T33); C: Surface, double bounce and volume scattering from Freeman-Durden Decomposition (Red: double-bounce, Green: volume, Blue: surface); D: Entropy (H); E: Alpha angle; F: Legend of labels and color codes from H-alpha classifier; G: Labels from H-alpha classifier developed by Lee et al. (1999); H: Results from the MRF classifier.

RS2-SLC-SQ5W-ASC-18-Nov-2015_01.15

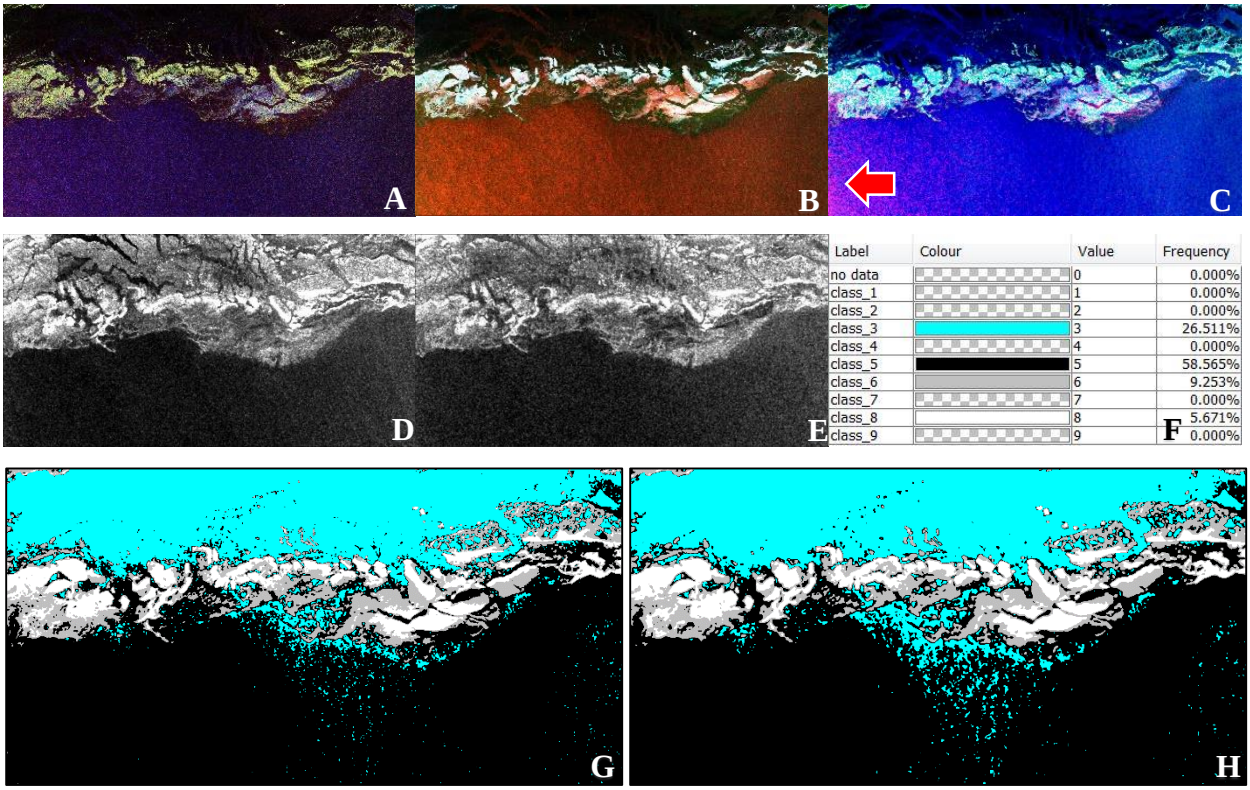

Figure 3.13: This image was acquired during the freeze-up period on November 18, 2015 at ascending orbit. See Table 3.1 for further details on image acquisition characteristics. A: Three features from Pauli decomposition (Red: HH-VV, Green: 2HV, Blue: HH+VV); B: Coherency matrix (Red: T11, Green: T22, Blue: T33); C: Surface, double bounce and volume scattering from Freeman-Durden Decomposition (Red: double-bounce, Green: volume, Blue: surface); D: Entropy (H); E: Alpha angle; F: Legend of labels and color codes from H-alpha classifier; G: Labels from H-alpha classifier developed by Lee et al. (1999); H: Results from the MRF classifier. Note that the red area pointed by red arrow cannot be interpreted as double-bounce scattering dominating on open water surface.

RS2-SLC-SQ7W-DES-18-Nov-2015_14.54

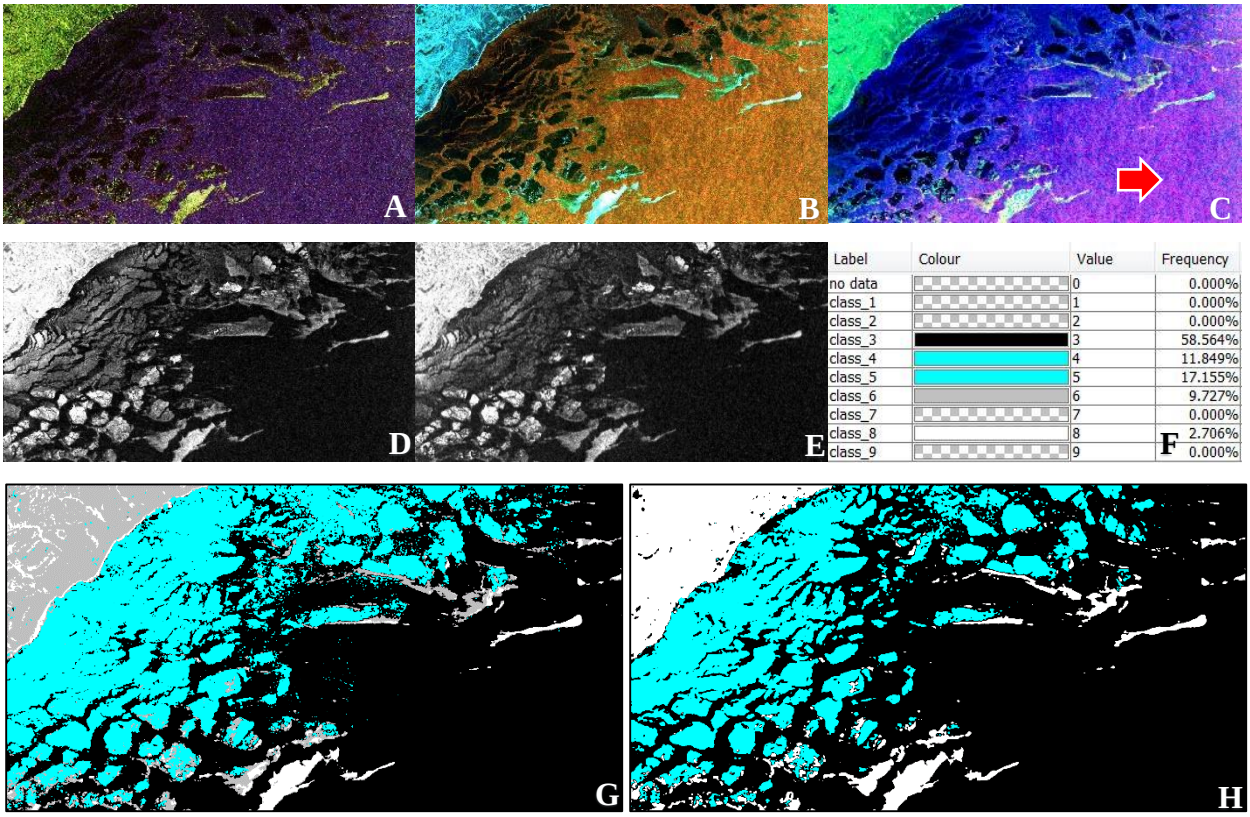

Figure 3.14: This image was acquired during the freeze-up period on November 18, 2015 at descending orbit. See Table 3.1 for further details on image acquisition characteristics. A: Three features from Pauli decomposition (Red: HH-VV, Green: 2HV, Blue: HH+VV); B: Coherency matrix (Red: T11, Green: T22, Blue: T33); C: Surface, double bounce and volume scattering from Freeman-Durden Decomposition (Red: double-bounce, Green: volume, Blue: surface); D: Entropy (H); E: Alpha angle; F: Legend of labels and color codes from H-alpha classifier; G: Labels from H-alpha classifier developed by Lee et al. (1999); H: Results from the MRF classifier. Note that the red area pointed by red arrow cannot be interpreted as double-bounce scattering dominating on open water surface.

RS2-SLC-SQ13W-ASC-21-Nov-2015_01.28

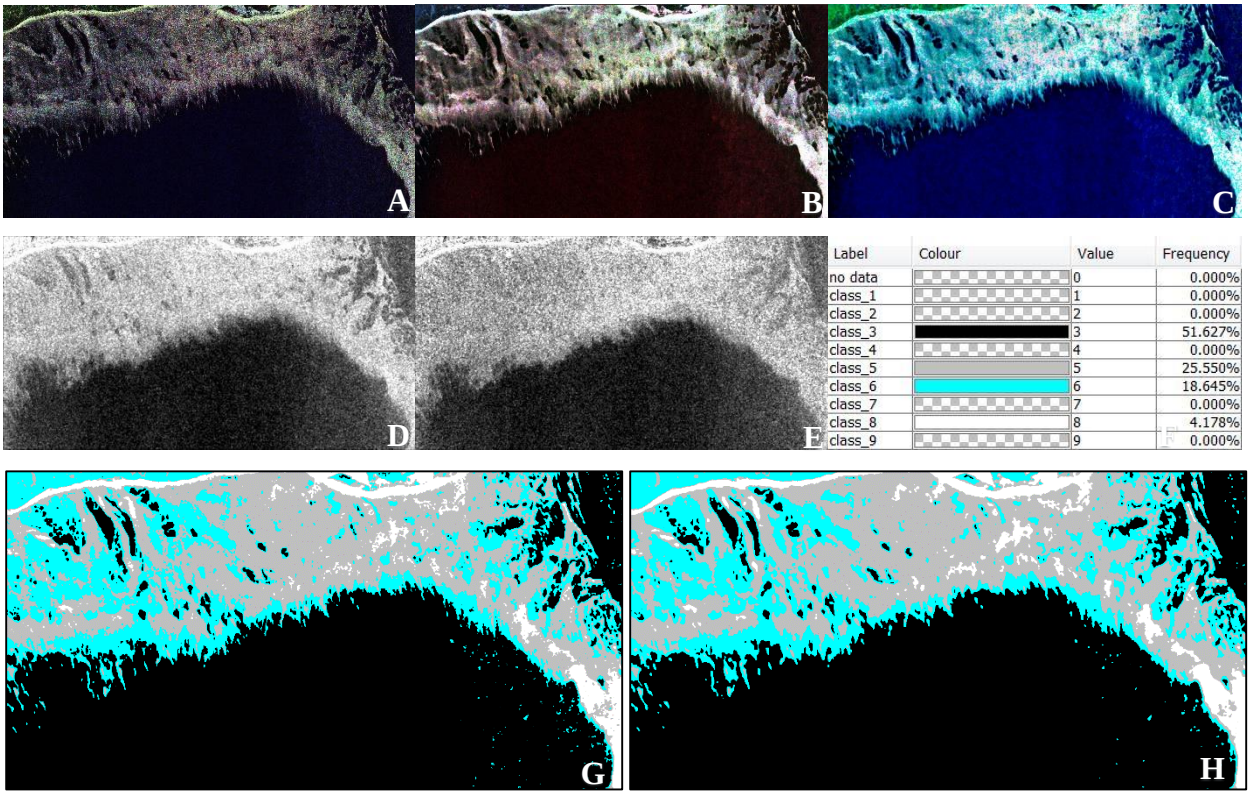

Figure 3.15: This image was acquired during the freeze-up period on November 21, 2015 at ascending orbit. See Table 3.1 for further details on image acquisition characteristics. A: Three features from Pauli decomposition (Red: HH-VV, Green: 2HV, Blue: HH+VV); B: Coherency matrix (Red: T11, Green: T22, Blue: T33); C: Surface, double bounce and volume scattering from Freeman-Durden Decomposition (Red: double-bounce, Green: volume, Blue: surface); D: Entropy (H); E: Alpha angle; F: Legend of labels and color codes from H-alpha classifier; G: Labels from H-alpha classifier developed by Lee et al. (1999); H: Results from the MRF classifier.

RS2-SLC-SQ2W-ASC-25-Nov-2015_01.11

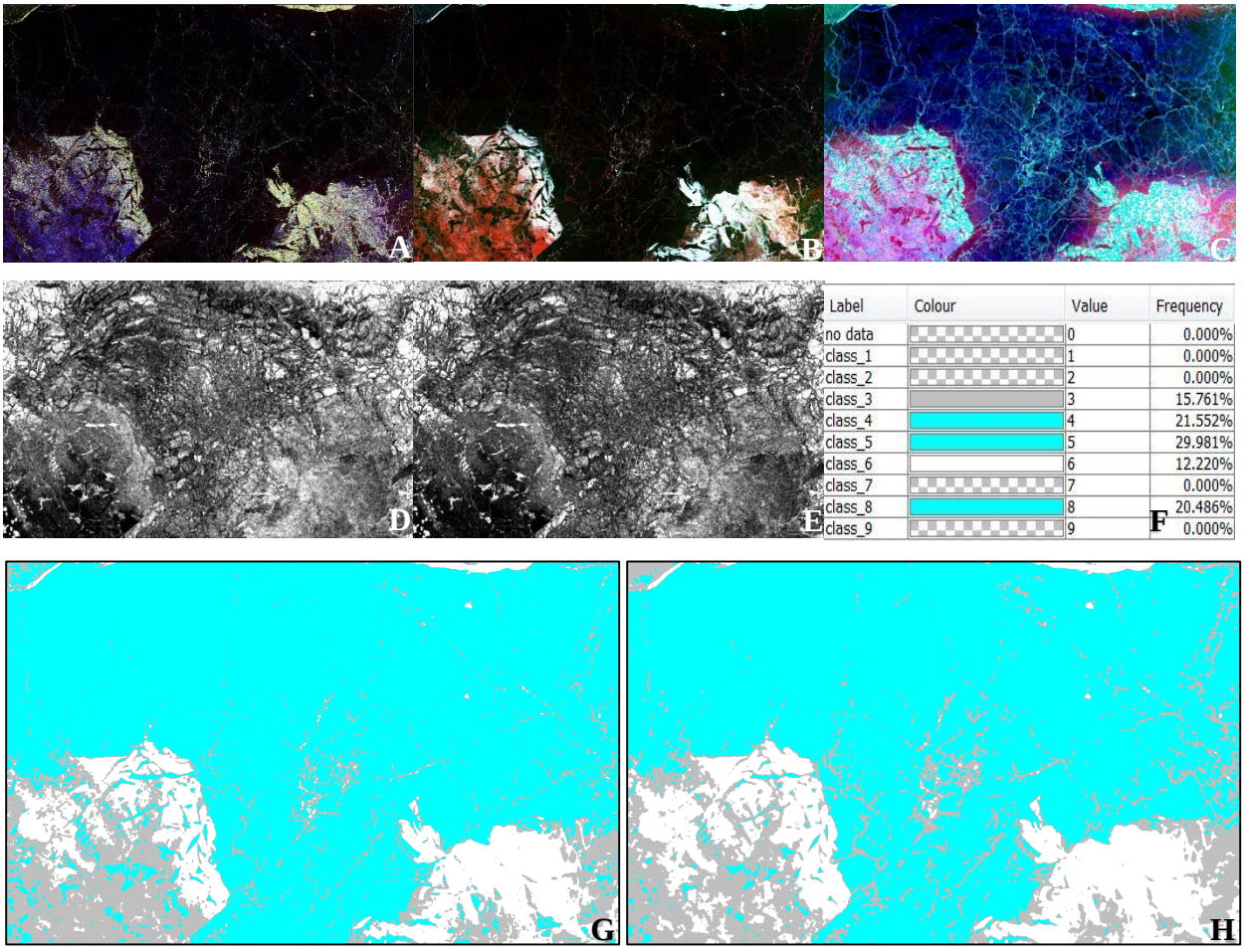

Figure 3.16: This image was acquired during the freeze-up period on June 25, 2015 at ascending orbit. See Table 3.1 for further details on image acquisition characteristics. A: Three features from Pauli decomposition (Red: HH-VV, Green: 2HV, Blue: HH+VV); B: Coherency matrix (Red: T11, Green: T22, Blue: T33); C: Surface, double bounce and volume scattering from Freeman-Durden Decomposition (Red: double-bounce, Green: volume, Blue: surface); D: Entropy (H); E: Alpha angle; F: Legend of labels and color codes from H-alpha classifier; G: Labels from H-alpha classifier developed by Lee et al. (1999); H: Results from the MRF classifier.

RS2-SLC-SQ9W-DES-25-Nov-2015_14.50

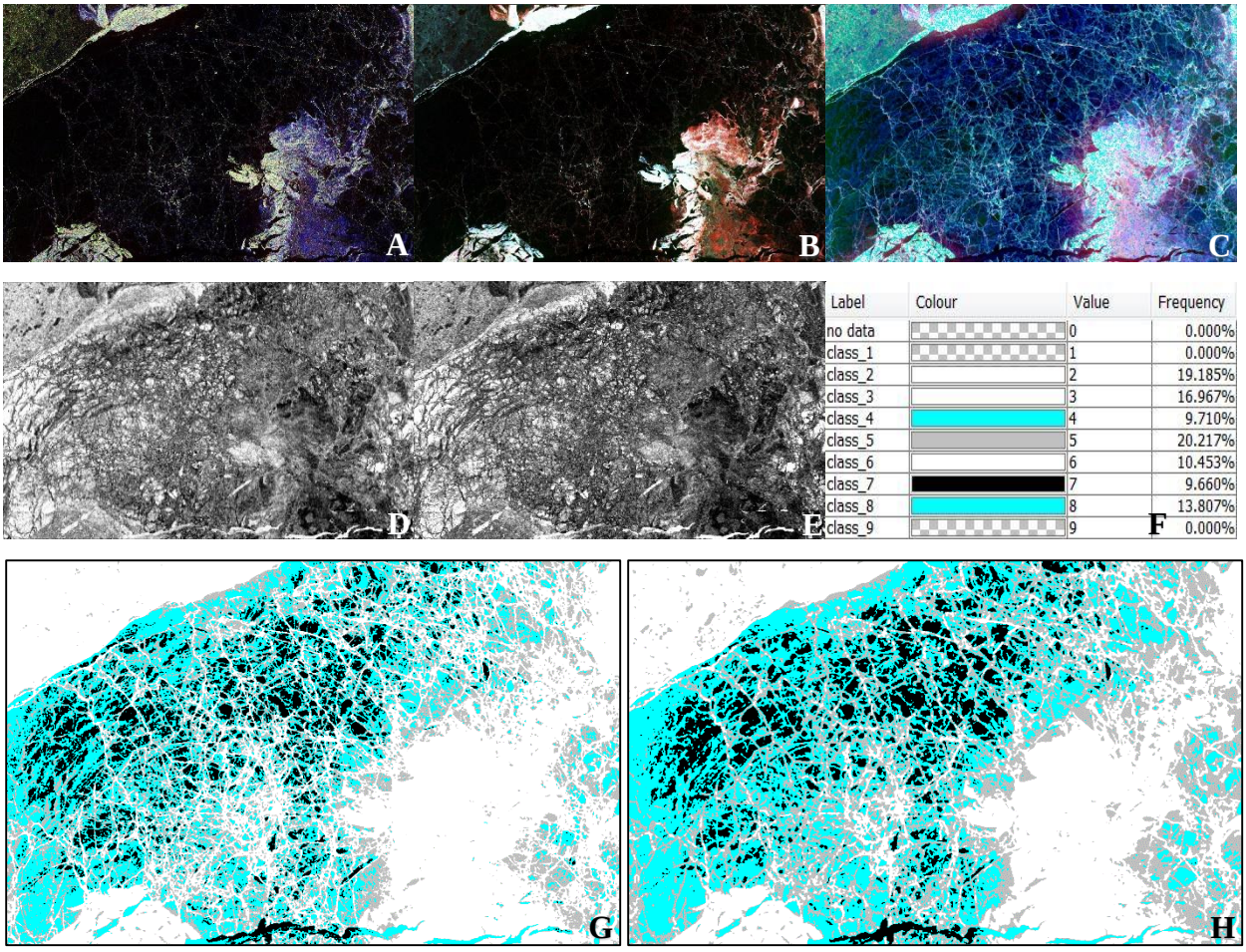

Figure 3.17: This image was acquired during the freeze-up period on November 25, 2015 at descending orbit. See Table 3.1 for further details on image acquisition characteristics. A: Three features from Pauli decomposition (Red: HH-VV, Green: 2HV, Blue: HH+VV); B: Coherency matrix (Red: T11, Green: T22, Blue: T33); C: Surface, double bounce and volume scattering from Freeman-Durden Decomposition (Red: double-bounce, Green: volume, Blue: surface); D: Entropy (H); E: Alpha angle; F: Legend of labels and color codes from H-alpha classifier; G: Labels from H-alpha classifier developed by Lee et al. (1999); H: Results from the MRF classifier.

RS2-SLC-SQ11W-ASC-28-Nov-2015_01.24

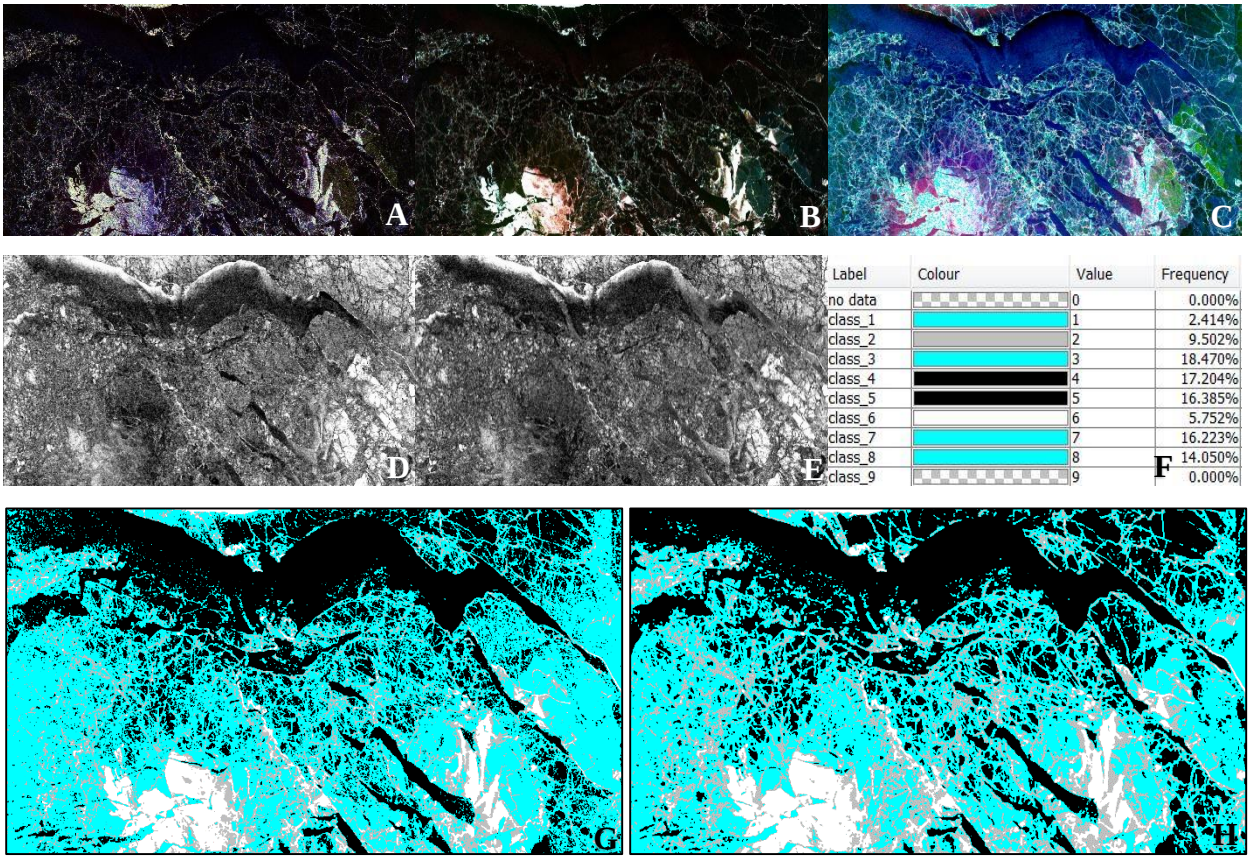

Figure 3.18: This image was acquired during the freeze-up period on November 28, 2015 at ascending orbit. See Table 3.1 for further details on image acquisition characteristics. A: Three features from Pauli decomposition (Red: HH-VV, Green: 2HV, Blue: HH+VV); B: Coherency matrix (Red: T11, Green: T22, Blue: T33); C: Surface, double bounce and volume scattering from Freeman-Durden Decomposition (Red: double-bounce, Green: volume, Blue: surface); D: Entropy (H); E: Alpha angle; F: Legend of labels and color codes from H-alpha classifier; G: Labels from H-alpha classifier developed by Lee et al. (1999); H: Results from the MRF classifier.

3.4.1 Interpretation of Polarimetric Features

3.4.1.1 Pauli Decomposition and Coherency Matrix

In the scattering elements from the Pauli-feature scattering vector (Figures 3.5-3.18, A), calm open water tends to be dark in most of these images. When the radar signal is reflected away from the sensor, these areas are expected to be black, with less backscatter power. It is easy to notice that open water areas in the image of June 17 (Figure 3.6) are much bluer, because this image was acquired in swath position of SQ1W, where the incident angle is small, from $17.5°$ to $21.2°$, and more backscatter was received by the sensor. These areas are consistent with the single scattering mechanism ($S_{HH} + S_{VV}$) (Lee & Pottier, 2009; Van Zyl & Kim, 2010). For the same reason, in the image of June 27 (Figure 3.11) the left part of water area is also shown as blue. Ice covered areas tend to show a mixture of scattering, where even reflection ($S_{HH} - S_{VV}$) and random scattering ($2S_{HV}$) tend to contribute more to the ice signal than open water areas. Therefore, the mixture of blue and green is typically observed over ice covered areas. Different ice types show a different concentration of specific color due to the dielectric/scattering properties and incidence angle. This explanation proceeds from the Pauli basis, which has been chosen to interpret the scattering.

The diagonal elements of the coherency matrix are presented also presented in Figures 3.5 to 3.18 (B). The scattering mechanisms are coded as different colors compared to Pauli decompositions. The red, green and blue channels are filled by T_{11}, T_{22} and T_{33}, respectively. Therefore, single scattering or even-bounce scattering (surface) tends to be red, odd bounce scattering (double-bounce) tends to be green, and random scattering (volume) tends to be blue in these images. Note that the refined Lee filter was applied to coherency elements; thus, speckle noise was further reduced, and neighbouring stochastic processes considered. Since the signal received by the sensor was averaged or integrated by the scatterings from various single targets and a target itself may not be stationary, the distributed scatters can be analyzed more precisely through the second-order moments of fluctuations (Lee & Pottier, 2009; Van Zyl & Kim, 2010).

3.4.1.2 Freeman-Durden Decomposition

For large incidence angles, surface scattering is dominant for open water and volume scattering tends to be contributed mainly from ice (Leshkevich & Nghiem, 2013; Nghiem & Leshkevich, 2007). When the incidence angle is small (lower than 25°), scattering is dominated by surface scattering from open water where water with a high relative permittivity has higher co-pol backscatter than ice (Leshkevich & Nghiem, 2013). An increase of double-bounce scattering may be seen at the ridges or cracks of ice (Scheuchl, Hajnsek & Cumming, 2002).

When incidence angle is large (larger than 30°), it is expected that open water may have single scattering (surface), where the radar signal is reflected away from the radar; thus, open calm water tends to be dark generally. Even if the power received by the radar sensor is small, the surface scattering is still dominant for open water areas (Leshkevich & Nghiem, 2013). For example, the surface scattering can be observed as blue in the image of Jun 24 (Figure 3.9) during the break-up period and Nov 21 during fall freeze-up. As the incidence angle becomes smaller or waves form on the lake, higher power is received by the radar from open water areas, where surface scattering is dominant. The dominant surface scattering is easily detected as blue in many images; for example, the June 17 (Figure 3.6) and June 27 (Figure 3.11) for the break-up period, and Nov 18 for the freeze-up period.

It is noticeable that red (pink or orange) can be observed in open water area; however, it cannot be interpreted as double-bounce scattering dominating on the water surface; for example, red shows up in open water occasionally in the image of Jun 27 in Figure 3.10 and Figure 3.11 and Nov 18 in Figure 3.13 and Figure 3.14, pointed by red arrows. It can be explained by the small scale of double bounce scattering (intensity). Even if double bounce scattering still has the weakest contribution among three orthogonal scattering mechanisms, it is bright for the red channel when displaying due to the low maximum power. We randomly collected samples over these red areas, and the statistical properties for three scattering mechanisms were summarized in Table 3.2.

Table 3.2: The Summary of Statistical Properties of Samples over Red Areas

SCATTERING	Min.	Max.	Mean	Std. Dev.
Double Bounce	49.765	60.797	56.023	1.296
Volume	51.009	74.815	62.568	0.619
Surface	49.765	74.727	72.148	0.593

Over ice covered areas, backscatter from surface scattering is higher than volume scattering, and double bounce scattering has been reported as the weakest contribution (Scheuchl, Hajnsek, & Cumming, 2002; Leshkevich & Nghiem, 2013; Hossain et al., 2014). The total power is higher for low incidence angle than high incidence angles because of the sensitivity of surface scattering to incidence angle (Hossain et al., 2014). Although surface scattering still dominates over ice covered areas, the volume scattering contributes more to the total scattering for rough ice. Radar incidence angle has a limited effect on volume scattering for ice covered areas (Hossain et al., 2014). Double bounce scattering shows a greater contribution for rougher ice especially when ice ridges are present. During the freeze-up period, new ice with a smooth surface can easily be misidentified as calm open water. The total power of the three scattering mechanisms from the smooth ice is low, where volume scattering has an obvious decrease. Surface scattering increases as incidence angle becomes smaller (Hossain et al., 2014).

3.4.1.3 Entropy and Alpha Angle

Most open water areas are dominated by surface scattering for both large and small incidence angles (Scheuchl, Hajnsek, & Cumming, 2002; Leshkevich & Nghiem, 2013; Hossain et al., 2014). The dominant surface scattering corresponded to the eigenvector $\boldsymbol{u} = [1 \quad 0 \quad 0]^T$, where S_{HH} is close to S_{VV} (Lee & Pottier, 2009); thus $\bar{\alpha}$ is low (less than $42.5°$). Since surface scattering is the only scattering mechanism that is dominant over these open water areas, the entropy is relatively low. Therefore, it can be observed that most of water areas with Bragg (surface) scattering tend to have low or medium entropy and very low alpha angle (Lee & Pottier, 2009).

On the other hand, an exception can be observed when an open water surface is calm (no/low wind or wave disturbance). In such situation, the entropy and alpha angle are both observed as being high ($\bar{\alpha}$ larger than $47.5°$ and entropy larger than 0.9). The scattering mechanisms over open water cannot be simply interpreted as double reflection or complex structures as characterized in the traditional H and $\bar{\alpha}$ space (Cloude & Pottier, 1997); nevertheless, the scattering from such surface is single scattering and the sensor received very weak signals for all polarizations from calm open water areas. In this case, the surface acts as a specular reflector (Cable et al., 2014); therefore, the cross-pol signals are low enough (at the noise floor) to counter the existence of volume scattering (Cable et al., 2014), and co-pol signals are very weak as well, which results in both high entropy and alpha angle.

Double bounce scattering occurs in the presence of ice ridges and fracture, shown as red spots or lines in the image of Jun 21 (Figure 3.8 C). Such takes place when entropy is low (generally less than 0.5) and $\bar{\alpha}$ is more than $47.5°$, where S_{HH} is close to $-S_{VV}$; therefore, double-bounce scattering, that corresponds to eigenvector $\boldsymbol{u} = [0 \quad 1 \quad 0]^T$, is the dominant scattering mechanism (Lee & Pottier, 2009).

Entropy is generally moderate (0.5 to 0.9) for ice-covered areas, where scattering is highly random and mixed (Hossain, 2012; Cloude & Pottier, 1997). Surface scattering is still dominant; however, volume scattering tends to have a larger contribution. Power from double-bounce scattering is found to be low.

3.4.2 Accuracy Assessment of Classification Results

Accuracy assessments for the Entropy-alpha Wishart classifier and the MRF classifier in the identification of open water and ice cover (two classes) are summarized in Table 3.3 and Table 3.4, respectively. Note that the image of Nov 25 at ascending orbit was fully covered by ice; therefore, this image was not included in the accuracy assessments. The overall accuracy of the Entropy-alpha Wishart classifier is 95.55% for the 13 images, and the MRF classifier 96.75%, which provides a slight improvement of 1.20% in overall accuracy. For lake ice identification, the Entropy-alpha Wishart classifier performed better than the MRF classifier, which is due to a higher accuracy during the freeze-up period. The Entropy-alpha Wishart classifier displays a lower accuracy for water identification, especially on June 17 due to the lack of consideration of neighboring pixels. The MRF classifier provided a better and more stable performance for open water identification, where accuracies are 97.45% and 98.09% for the break-up and freeze-up periods, respectively. This is due to the prior being added to the probability calculation with MRF, in which case noise-like pixels misidentified as water were partially avoided.

Overall both classifiers performed better during the break-up period than the freeze-up period, mainly as a result of misidentification of new ice and thin ice during freeze-up. Compared to the Entropy-alpha Wishart classifier, the MRF classifier achieved a 2.03% higher accuracy during break-up. The two classifiers performed similarly during the freeze-up period with an accuracy of 94.3%. However, the Entropy-alpha Wishart classifier can identify ice better than the MRF classifier, while the MRF classifier is better at identifying open water. The misclassified pixels may result not only from the misclassification from the two classifiers, but also from the misidentification and mistakes in digitization of the manual (visual) delineation of open water and ice polygons.

Table 3.3: The Summary of Overall Accuracy for Entropy-Alpha Wishart Classifier

CLASS / DATE	Open Water	Ice	Overall
Jun 16, ASC	1	0.9989	0.99945
Jun 17, ASC	0.6574	0.9505	0.80395
Jun 17, DES	0.9990	0.9999	0.99945
Jun 21, DES	1	0.9872	0.9936
Jun 24, DES	1	1	1
Jun 27, ASC	1	0.9853	0.9927
Jun 27, DES	0.9937	0.9932	0.9935
Jun 30, ASC	0.8465	1	0.9233
Nov 18, ASC	0.9929	0.9032	0.9481
Nov 18, DES	0.9988	0.9291	0.9640
Nov 21, ASC	0.9977	1	0.9989
Nov 25, DES	0.8681	0.9068	0.8875
Nov 28, ASC	0.9582	0.8753	0.9168
Freeze-up Period	0.9631	0.9229	0.9430
Break-up Period	0.9371	0.9894	0.9632
Overall Accuracy	0.9471	0.9638	0.9555

Table 3.4: The Summary of Overall Accuracy for MRF Classifier

CLASS / DATE	Open Water	Ice	Overall
Jun 16 ASC	0.8688	1	0.9344
Jun 17 ASC	1	0.9366	0.9683
Jun 17 DES	0.9943	1	0.9972
Jun 21 DES	0.9846	0.9994	0.9920
Jun 24 DES	1	1	1
Jun 27 ASC	1	0.9996	0.9998
Jun 27 DES	0.9996	0.9948	0.9972
Jun 30 ASC	0.9489	1	0.9745
Nov 18 ASC	0.9826	0.9012	0.9419
Nov 18 DES	1	0.8659	0.9330
Nov 21 ASC	0.9983	1	0.9992
Nov 25 DES	0.9822	0.8973	0.9398
Nov 28 ASC	0.9416	0.8598	0.9007
Freeze-up	0.9809	0.9048	0.9429
Break-up	0.9745	0.9913	0.9829
Overall Accuracy	0.9770	0.9580	0.9675

3.5 Conclusion

In this study, we analyzed the scattering mechanisms associated with polarimetric parameters from RADARSAT-2 quadrature polarimetric data obtained over the Great Bear Lake during the break-up and freeze-up periods of 2015. When incidence angle is large, the power received by the sensor is weak. Surface scattering is dominant for open water area and volume scattering contributed more to the total scattering from ice covered area especially when ice surface is rough. When incidence angle is small, higher power can be received by the sensor from open water areas, where surface scattering is still dominant. Automated classification of lake ice was also presented by expanding the Entropy-alpha Wishart classifier to more polarimetric features and by introducing MRF to complete the prior probability. Labels used for training the MRF were generated from the H-alpha Wishart classifier proposed by Lee et al. (1999), which initialized the original classes based on the entropy and alpha angle zones proposed by Cloude & Pottier (1997), and only used the covariance matrix to maximize the likelihood based on the complex Wishart distribution (Lee et al., 1999). The parameters for features' distribution were estimated through the method of moments based on the labels, and these were further used to calculate the likelihood for each class. The priors were achieved through MRF, and the class with the highest posterior were chosen as the final output.

The MRF classifier used in this study successfully classified open water and lake ice, with an overall accuracy of 96.75%, which provided a small improvement of 1.2% over the Entropy-alpha Wishart classifier. Results from MRF classifier were in strong agreement with the manual identification of ice and open water areas delineated by the ice analyst of Canadian Ice Service, Environment and Climate Change Canada (ECCC). Therefore, the MRF classifier developed in this study has a large potential to semi-automatically operate lake ice classification and substitute visual interpretation in the face of large volume of data and analytics pressures.

The limitation of this study was the lack of optical satellite data sources for the evaluation of classification results. The coarse resolution, cloud cover and polar darkness highly influenced the availability of using optical data. On the other hand, the classifications in this study still rely

on manual combination and identification at the end to determine if a class belongs to water or ice. The polarimetric parameters can be characterized for ice and open water in the future studies, so that classes can be automatically combined and identified based on their polarimetric characteristics instead of manual operations. This study employed the method of moments instead of EM optimization due to the balance of running time and classification performance; therefore, it utilized the Entropy-alpha Wishart classification results as labels. In the future work, the MRF can be easily transformed to unsupervised clustering by replicating the EM algorithm to estimate the parameters and maximizing the posterior iteratively.

4 Conclusion

4.1 Summary

The overall objective of this research was to analyze polarimetric parameters in identifying open water and lake ice to improve the understanding of lake ice observations, and to develop a classification approach that can discriminate open water and lake ice. This work did not only contribute to an improved understanding of polarimetric radar imaging of the cryosphere, but it also provided insight into canonical scattering mechanism of microwave interactions with ice and open water. The MRF algorithm implemented in this study successfully classified open water and lake ice, which was in close great agreement with manual (visual) identification by the ice analyst of the Canadian Ice Service (CIS). Therefore, the MRF classifier with pixels labeled by H-alpha Wishart classifier has a large potential for semi-automated lake ice classification as a complement to visual interpretation of a large volume of RADARSAT-2 images at CIS.

Chapter 1 introduced the necessity for lake ice monitoring and an overview of current remote sensing techniques for lake ice research. It also identified the need for improvement in automated lake-ice classification. The background chapter then provided a more detailed review of SAR research for lake ice mapping/monitoring and approaches being used for SAR classification. It also summarized the basics of electromagnetic and polarimetric radar theory, relevant probabilities and mathematical statistics, and the classifiers used to this study. The manuscript chapter implemented the Markov Random Field with pixels labeled by H-alpha Wishart classifier for discriminating open water and lake ice. This chapter provides an overall summary of the thesis, identifies some of its limitations and gives possible directions for future research.

The study presented an application of the Markov Random Field in polarimetric radar imaging. To reduce the running time caused by the optimization of the unsupervised clustering (EM), the entropy-alpha Wishart classifier was introduced for labeling; therefore, the parameters of the individual distributions can be determined by the method of moments estimator. Instead of using covariance matrix alone, the feature space has been extended by introducing more

polarimetric features. In the Entropy-alpha classifier, the prior was fixed to a constant; however, this study employed the Markov Random Field to determine the prior according to the neighbors of a pixel. For initializing the original classes, we retained the entropy and alpha space of the Entropy-alpha Wishart classifier. Since each sample was labeled, the parameters for the likelihood of the MRF classifier could be estimated by the method of moments instead of expectation maximization optimizer. The class merging and termination criteria introduced an optimizing problem for determining the number of classes. However, it was difficult to deduct the classes to the desired number of classes because of the characteristics of the statistical distribution over the feature spaces. Nonetheless, results showed a strong agreement with visual interpretation by an ice analyst CIS, with an overall accuracy of 96.75%. New thin ice during the freeze-up period was the main source of misclassification, resulting in a lower accuracy of 90.48%.

4.2 Limitations

The greatest limitation of this study was the lack of other (optical) satellite data sources for the evaluation of classification results. Some MODIS images were available during the time of RADARSAT-2 image acquisitions during the break-up period (no useful MODIS images were available during the freeze-up period due to polar darkness). However, the spatial resolution of the MODIS corrected reflectance product is 250 m, which is much coarser than that of the RADARSAT-2 images (9.0 - 12.8 m by 7.6 m) used in this thesis. We also turned to possible Landsat scenes; however, the radar illuminated areas were not clear in these optical images as they were highly affected by cloud cover and were acquired only once weekly. In addition, the time of acquisitions between Landsat and RADARSAT-2 presented a problem for comparison. The movement of ice floes over time scales of minutes to hours during the freeze-up and break-up periods made the use of Landsat images difficult for the evaluation of classification results.

The manual (visual) delineation of open water and ice polygons by the ice analyst from CIS had its advantages and disadvantages. It did not present the same type of problems as mentioned above because the analysis and classifications were both performed on the radar images directly. Although the available RADARSAT-2 images were employed to help recognize and distinguish

open water and ice targets during the delineation, the accuracy of this process fully depends on the ice analyst's experiences of visual identification, which may introduce errors and uncertainties due to artificial factors. The assessment of this process when humans are involved is very difficult to control.

As mentioned in Section 3.3.2 (methodology of the manuscript), the performance of the running time for optimization, expectation maximization, should be improved. This process in the Entropy-alpha Wishart classifier operates only on the covariance matrix. When the EM algorithm is expanded to more polarimetric features like intensities and decomposition parameters, the time complexity may increase exponentially. In the end, we decided to retain the low-dimensional EM processes for seeking the clusters as unsupervised labeling and recalculate the probability for each pixel in the following supervised training and testing. The complexity of the model has been decreased, but it has also uncovered some limitations. First, it might be constrained from the Entropy-alpha Wishart classifier, and not take advantage of the newly introduced polarimetric features, due to the influences of low-dimensional labeling. For instance, these classes or targets, which can only be discriminated in the higher dimensional space, may not be correctly distinguished in covariance relations, the second order space. Second, there are no further iterative processes to adjust the centre of each class for labeling. The Entropy-alpha Wishart classifier takes advantage of the zones in entropy and alpha angle space to initiate the clusters, and then iteratively seek for the updated centre. However, in this study, once these pixels are labeled by Entropy-alpha Wishart classifier, the centre of the classes no longer moved during the training. In addition, the classes are initialized according to the admissible zones in alpha and entropy plane as shown in Figure 3.3. However, it could be divided into more classes. It could be applied to achieve the desired number of classes instead of a fixed 9 zones.

The likelihoods of decomposition parameters in the Bayesian inference are assumed to be Gaussian distributed. As they arise from application of the central limit theorem, when independent random variables are sampled, their sum tend to a Gaussian distribution. However, the original variables may not be normally distributed. The convergence in Gaussian distribution is toward a

single peak; however, each class may contain multi targets or distributed targets, where the decomposition parameters may converge towards multi peaks or at least a single value.

Fourteen images (eight during the break-up period and six during the freeze-up period) were used for testing the model built in this study. Unfortunately, these radar images were acquired at individual swath position, and each swath position corresponds to a different incidence angle range. The incidence angle plays an important role in scattering, which will be manifested in the radar return and polarimetric parameters. To control the variance caused by the incidence angle, the training and testing of the MRF can be conducted only at a fixed swath position, which means the parameter estimate and elements in the Bayesian inference cannot be shared among different images or, to be more specific, different swath position.

4.3 Future Work

The model built in this study has high potential to be fully unsupervised by simply replicating the EM algorithm to estimate the parameters and maximizing the inference iteratively for newly introduced polarimetric features. This study employed the method of moments instead of EM optimization for the parameter estimate due to a balance of the running time and classification performance. The model can be improved by optimizing the Matlab code or moving onto a new platform with a faster running and operating performance, such as machine learning libraries and Hadoop distributed systems.

As mentioned in Section 4.2, to control the variance caused by the incidence angle, the training and testing of the MRF could be conducted only at a fixed swath position; in other words, the parameter estimate and elements in the Bayesian inference could not be shared among different images. However, as images acquired at the same swath position increase, the samples from the specific swath position are large enough to be generalized to any new images at the same swath position. At this time, previous images that have been validated with confident labels could be employed to characterize the statistical properties of open water and different ice types. A supervised classification (the same algorithm as in this study) could be conducted for more

accurate inference and faster classification. To accomplish this task, one needs to take advantage of big data development, as it enables a computing solution that maintains computing speed in the processing of a large dataset.

References

Arkett, M., Carrieres, T., Zagon T., Zabeline, V., Buehner, M., Caya, A., Luo, Y. (2013). Preparations by the Canadian Ice Service for Future Earth Observation Missions, In Proc. Earth Observation and Cryosphere Science Conference 2012, Frascati, Italy.

Ashton, G. D. (Ed.). (1986). River and lake ice engineering. Water Resources Publication.

Atwood, D. K., Gunn, G. E., Roussi, C., Wu, J., Duguay, C., & Sarabandi, K. (2015). Microwave backscatter from Arctic lake ice and polarimetric implications. IEEE Transactions on Geoscience and Remote Sensing, 53(11), 5972-5982.

Brown, L. C., & Duguay, C. R. (2012). Modelling lake ice phenology with an examination of satellite-detected subgrid cell variability. Advances in Meteorology, 2012.

Cable, J. W., Kovacs, J. M., Shang, J., & Jiao, X. (2014). Multi-temporal polarimetric RADARSAT-2 for land cover monitoring in northeastern Ontario, Canada. Remote Sensing, 6(3), 2372-2392.

Canadian Ice Service of Environment and Climate Change Canada. (2017). https://www.ec.gc.ca/glaces-ice

Canadian Space Agency. (2014). http://www.asc-csa.gc.ca/eng/satellites/radarsat1/

Canadian Space Agency. (2015). http://www.asc-csa.gc.ca/eng/satellites/radarsat2/

Canadian Space Agency. (2017). http://www.asc-csa.gc.ca/eng/satellites/radarsat/

Charbonneau, F. J., Brisco, B., Raney, R. K., McNairn, H., Liu, C., Vachon, P. W.,Geldsetzer, T. (2010). Compact polarimetry overview and applications assessment. Canadian Journal of Remote Sensing, 36(S2), S298-S315.

Colbeck, S. C. (Ed.). (2012). Dynamics of snow and ice masses. Elsevier.

Cloude, S. R. (1985). Radar target decomposition theorems. Electronics Letters, 21(1), 22-24.

Cloude, S. R., & Pottier, E. (1996). A review of target decomposition theorems in radar polarimetry. IEEE Transactions on Geoscience and Remote Sensing, 34(2), 498-518.

Dabboor, M., & Geldsetzer, T. (2014). Towards sea ice classification using simulated RADARSAT Constellation Mission compact polarimetric SAR imagery. Remote sensing of environment, 140, 189-195.

Du, J., Kimball, J. S., Duguay, C., Kim, Y., & Watts, J. D. (2017). Satellite microwave assessment of Northern Hemisphere lake ice phenology from 2002 to 2015. The Cryosphere, 11, 47.

Duguay, C. R., Pultz, T. J., Lafleur, P. M., & Drai, D. (2002). RADARSAT backscatter characteristics of ice growing on shallow sub-Arctic lakes, Churchill, Manitoba, Canada. Hydrological Processes, 16(8), 1631-1644.

Duguay, C. R., Prowse, T. D., Bonsal, B. R., Brown, R. D., Lacroix, M. P., & Ménard, P. (2006). Recent trends in Canadian lake ice cover. Hydrological Processes, 20(4), 781-801.

Duguay, C. R., Bernier, M., Gauthier, Y., & Kouraev, A. (2015). Remote sensing of lake and river ice. Remote sensing of the cryosphere, 273-306.

European Space Agency. (2017). http://www.esa.int/Our_Activities/Observing_the_Earth.

Freeman, A., & Durden, S. L. (1993). Three-component scattering model to describe polarimetric SAR data. In San Diego'92 (pp. 213-224). International Society for Optics and Photonics.

Freeman, A., & Durden, S. L. (1998). A three-component scattering model for polarimetric SAR data. IEEE Transactions on Geoscience and Remote Sensing, 36(3), 963-973.

Geldsetzer, T., & van der Sanden, J. J. (2013). Identification of polarimetric and nonpolarimetric C-band SAR parameters for application in the monitoring of lake ice freeze-up. Canadian Journal of Remote Sensing, 39(3), 263-275.

Geldsetzer, T., van der Sanden, J. V. D., & Brisco, B. (2010). Monitoring lake ice during spring melt using RADARSAT-2 SAR. Canadian Journal of Remote Sensing, 36(S2), S391-S400.

Geldsetzer, T., van der Sanden, J. J., & Drouin, H. (2011, July). Advanced SAR applications for Canada's river and lake ice. In Geoscience and Remote Sensing Symposium (IGARSS), 2011 IEEE International (pp. 3168-3170). IEEE.

Gill, J. P., & Yackel, J. J. (2012). Evaluation of C-band SAR polarimetric parameters for discrimination of first-year sea ice types. Canadian Journal of Remote Sensing, 38(3), 306-323.

Gurney, R. J., Foster, J. L., & Parkinson, C. L. (1993). Atlas of satellite observations related to global change. Cambridge University Press.

Hossain, M. (2012). Polarimetric synthetic aperture radar measurements of snow covered first-year sea ice (Doctoral dissertation, University of Calgary).

Hossain, M., Yackel, J., Dabboor, M., & Fuller, M. C. (2014). Application of a three-component scattering model over snow-covered first-year sea ice using polarimetric C-band SAR data. International journal of remote sensing, 35(5), 1786-1803.

Huynen, J. R. (1970). Phenomenological theory of radar targets. Ph.D. dissertation, Drukkerij Bronder-offset N.V., Rotterdam.

Kheyrollah Pour, H., Duguay, C. R., Martynov, A., & Brown, L. C. (2012). Simulation of surface temperature and ice cover of large northern lakes with 1-D models: a comparison with MODIS satellite data and in situ measurements. Tellus A: Dynamic Meteorology and Oceanography, 64(1), 17614.

Lee, J. S., & Pottier, E. (2009). Polarimetric radar imaging: from basics to applications. CRC press.

Leshkevich, G. A., & Nghiem, S. V. (2007). Satellite SAR remote sensing of Great Lakes ice cover, part 2. Ice classification and mapping. Journal of Great Lakes Research, 33(4), 736-750.

Leshkevich, G. A., & Nghiem, S. V. (2009, May). Using satellite radar data to map and monitor variations in Great Lakes Ice Cover. In Radar Conference, 2009 IEEE (pp. 1-3). IEEE.

Leshkevich, G., & Nghiem, S. V. (2013). Great Lakes ice classification using satellite C-band SAR multi-polarization data. Journal of Great Lakes Research, 39, 55-64.

Morris, K., Jeffries, M. O., & Weeks, W. F. (1995). Ice processes and growth history on Arctic and sub-Arctic lakes using ERS-1 SAR data. Polar Record, 31(177), 115-128.

Natural Resources Canada. (2017). https://www.nrcan.gc.ca/home

Nghiem, S. V., & Leshkevich, G. A. (2007). Satellite SAR remote sensing of Great Lakes ice cover, Part 1. Ice backscatter signatures at C band. Journal of Great Lakes Research, 33(4), 722-735.

Rignot, E., & Chellappa, R. (1992). Segmentation of polarimetric synthetic aperture radar data. IEEE Transactions on Image Processing, 1(3), 281-300.

Scheuchl, B., Hajnsek, I., & Cumming, I. (2002). Sea ice classification using multi-frequency polarimetric SAR data. In Geoscience and Remote Sensing Symposium, 2002. IGARSS'02. 2002 IEEE International (Vol. 3, pp. 1914-1916). IEEE.

Scheuchl, B., Flett, D., Caves, R., & Cumming, I. (2004). Potential of RADARSAT-2 data for operational sea ice monitoring. Canadian Journal of Remote Sensing, 30(3), 448-461.

Ulaby, F. T., Moore, R. K., & Fung, A. K. (1981). Microwave remote sensing: Active and passive. volume I: Microwave remote sensing fundamentals and radiometry.

Ulaby, F. T., Moore, R. K., & Fung, A. K. (1982). Microwave Remote Sensing Active and Passive-Volume II: Radar Remote Sensing and Surface Scattering and Emission Theory.

Ulaby, F. T., Moore, R. K., & Fung, A. K. (1986). Microwave remote sensing active and passive-volume III: from theory to applications. (1986).

van Zyl, J. J. & Kim, J. (2010). Synthetic aperture radar polarimetry (Vol. 2). John Wiley & Sons.

Warner, T. A., Foody, G. M., & Nellis, M. D. (2009). The SAGE handbook of remote sensing. Sage Publications.

Yamaguchi, Y., Moriyama, T., Ishido, M., & Yamada, H. (2005). Four-component scattering model for polarimetric SAR image decomposition. IEEE Transactions on Geoscience and Remote Sensing, 43(8), 1699-1706.

Yueh, H. A., Swartz, A. A., Kong, J. A., Shin, R. T., & Novak, L. M. (1988). Bayes classification of terrain cover using normalized polarimetric data. Journal of Geophysical Research: Solid Earth, 93(B12), 15261-15267.

Appendices

Appendix A: Performance Assessments on Individual Classes between Classification and Validation for Entropy-Alpha Wishart Classifier

RS2-SLC-SQ18W-ASC-16-Jun-2015_01.36

MODEL / VALIDATION	Water	Water	Ice	Ice	Ice	Ice	Ice
Water	0.9995	0.0005	0	0	0	0	0
Ice	0	0.0011	0.1693	0.4691	0.0194	0.2555	0.0857

RS2-SLC-SQ1W-ASC-17-Jun-2015_01.07

MODEL / VALIDATION	Land	Ice	Ice	Ice	Ice	Ice	Water
Water	0.8599	0	0.048	0	0	0	0.0921
Ice	0.0022	0.1586	0.1513	0.2596	0.1751	0.2037	0.0494

RS2-SLC-SQ11W-DES-17-Jun-2015_14.46

MODEL / VALIDATION	Water	Ice	Ice	Ice	Ice
Water	0.999	0	0	0.001	0
Ice	0.0001	0.3241	0.2631	0.0364	0.3763

RS2-SLC-SQ21W-DES-21-Jun-2015_14.29

MODEL / VALIDATION	Water	Water	Ice	Ice	Ice	Ice	Ice
Water	0.9866	0.0134	0	0	0	0	0.9866
Ice	0.0021	0.0107	0.3733	0.2984	0.0637	0.2518	0.0021

RS2-SLC-SQ14W-DES-24-Jun-2015_14.42

MODEL / VALIDATION	Water	Water	Ice	Ice	Water	Ice	Ice
Water	0.594	0.1647	0	0	0.2413	0	0
Ice	0	0	0.0072	0.2047	0	0.0004	0.7878

RS2-SLC-SQ5W-ASC-27-Jun-2015_01.15

MODEL / VALIDATION	Water	Water	Ice	Water	Ice	Ice	Water	Water
Water	0.0124	0	0	0.4897	0	0	0.4853	0.0125
Ice	0	0.0147	0.0369	0	0.1674	0.781	0	0

RS2-SLC-SQ6W-DES-27-Jun-2015_14.54

MODEL / VALIDATION	Water	Ice	Water	Water	Ice	Ice	Water	Water
Water	0.0522	0.006	0.4073	0.1028	0.0003	0	0.2493	0.1821
Ice	0.0003	0.0134	0.0065	0	0.138	0.8418	0	0

RS2-SLC-SQ13W-ASC-30-Jun-2015_01.28

MODEL / VALIDATION	Water	Water	Water	Ice	Water
Water	0.388	0.0694	0.2721	0.1535	0.117
Ice	0	0	0	1	0

RS2-SLC-SQ5W-ASC-18-Nov-2015_01.15

MODEL / VALIDATION	Ice	Water	Ice	Ice
Open Water	0.0071	0.9929	0	0
Thin Ice	0.8449	0.1485	0.0066	0
Ice Floes	0.0635	0.045	0.3186	0.5729

RS2-SLC-SQ7W-DES-18-Nov-2015_14.54

MODEL / VALIDATION	Water	Ice	Ice	Ice	Ice
Open Water	0.9988	0	0.0012	0	0
Ice	0.0709	0.5464	0.2128	0.0625	0.1075

RS2-SLC-SQ13W-ASC-21-Nov-2015_01.28

MODEL / VALIDATION	Water	Ice	Ice	Ice
Open Water	0.9977	0	0.0023	0
New Ice	0	0.6969	0.03	0.273

RS2-SLC-SQ2W-ASC-25-Nov-2015_01.11

MODEL / VALIDATION	Medium/Thick Ice	Thin Ice	Thin Ice	Medium/Thick Ice	Thin Ice
Thin Ice	0.0317	0.1906	0.3997	0.0019	0.3762
Medium Ice/ Thick Ice	0.0642	0	0	0.9358	0

RS2-SLC-SQ9W-DES-25-Nov-2015_14.50

MODEL / VALIDATION	Thin/New Ice	Thick Ice	Water	Thin/New Ice	Thick Ice	Water	Thin/New Ice
Open Water	0.0003	0	0.4383	0.0066	0	0.4297	0.125
Thin Ice/ New Ice	0.1749	0.0461	0.103	0.2619	0.0037	0.1666	0.2438
Medium Ice	0.0003	0.0288	0	0	0.9709	0	0
Thick Ice	0.004	0.8876	0	0.0003	0.1081	0	0

RS2-SLC-SQ11W-ASC-28-Nov-2015_01.24

MODEL / VALIDATION	Thin Ice	Medium/ Thick Ice	Thin Ice	Water	Water	Medium/ Thick Ice	Thin Ice	Thin Ice
Open Water	0.0002	0	0.0324	0.4727	0.4856	0	0.0091	0.0001
Thin Ice	0.0154	0.0822	0.2427	0.1585	0.0909	0.0033	0.2094	0.1977
Medium/ Thick Ice	0.0002	0.0972	0	0	0	0.9018	0	0.0007

Appendix B: Performance Assessments on Individual Classes between Classification and Validation for MRF

RS2-SLC-SQ18W-ASC-16-Jun-2015_01.36

MODEL / VALIDATION	Ice	Water	Ice	Ice	Ice	Ice	Ice
Water	0.1312	0.8688	0	0	0	0	0
Ice	0	0	0.3517	0.3163	0.0025	0.2623	0.0672

RS2-SLC-SQ1W-ASC-17-Jun-2015_01.07

MODEL / VALIDATION	Water	Land	Ice	Ice	Ice	Ice
Water	0.6388	0.3612	0	0	0	0
Ice	0.0012	0.0633	0.3045	0.2723	0.1682	0.1906

RS2-SLC-SQ11W-DES-17-Jun-2015_14.46

MODEL / VALIDATION	Water	Ice	Ice	Ice	Ice
Water	0.9943	0	0	0.0057	0
Ice	0	0.5487	0.2392	0.0158	0.1963

RS2-SLC-SQ21W-DES-21-Jun-2015_14.29

MODEL / VALIDATION	Water	Ice	Ice	Ice	Ice	Ice	Ice
Water	0.9845	0.0152	0	0	0.0002	0	0
Ice	0.0006	0.0044	0.3197	0.3098	0.0207	0.2357	0.1092

RS2-SLC-SQ14W-DES-24-Jun-2015_14.42

MODEL / VALIDATION	Water	Water	Ice	Ice	Water	Water	Ice
Water	0.6465	0.1262	0	0	0.2269	0.0004	0
Ice	0	0	0.0031	0.1509	0	0	0.846

RS2-SLC-SQ5W-ASC-27-Jun-2015_01.15

MODEL / VALIDATION	Ice	Water	Ice	Ice	Water	Water
Water	0	0.4194	0	0	0.5647	0.0159
Ice	0.0326	0	0.1405	0.8264	0	0.0004

RS2-SLC-SQ6W-DES-27-Jun-2015_14.54

MODEL / VALIDATION	Water	Water	Ice	Ice	Water	Water
Water	0.5042	0.118	0.0004	0	0.2592	0.1182
Ice	0.0052	0	0.0961	0.8987	0	0

RS2-SLC-SQ13W-ASC-30-Jun-2015_01.28

MODEL / VALIDATION	Water	Water	Ice	Water	Water
Water	0.361	0.3687	0.0511	0.05	0.1692
Ice	0	0	1	0	0

RS2-SLC-SQ5W-ASC-18-Nov-2015_01.15

MODEL / VALIDATION	Ice	Ice	Ice	Water
Open Water	0.0174	0	0	0.9826
Thin Ice	0.8481	0.0048	0	0.147
Ice Floes	0.0479	0.2922	0.6094	0.0506

RS2-SLC-SQ7W-DES-18-Nov-2015_14.54

MODEL / VALIDATION	Water	Ice	Ice
Open Water	1	0	0
Ice	0.1341	0.71	0.1558

RS2-SLC-SQ13W-ASC-21-Nov-2015_01.28

MODEL / VALIDATION	Water	Ice	Ice	Ice
Open Water	0.9983	0	0.0017	0
New Ice	0	0.3208	0.021	0.6582

RS2-SLC-SQ2W-ASC-25-Nov-2015_01.11

MODEL / VALIDATION	Medium/Thick Ice	Thin Ice	Medium/Thick Ice	Thin Ice	Thin Ice
Thin Ice	0.0607	0.3028	0.0026	0.3997	0.2342
Medium Ice/ Thick Ice	0.0444	0	0.9556	0	0

RS2-SLC-SQ9W-DES-25-Nov-2015_14.50

MODEL / VALIDATION	Thick Ice	Thin/New Ice	Thin/New Ice	Thick Ice	Water	Water
Open Water	0.0001	0.0108	0.0069	0	0.5072	0.4749
Thin Ice/ New Ice	0.0924	0.3069	0.288	0.0046	0.1919	0.1162
Medium Ice	0.004	0	0	0.996	0	0
Thick Ice	0.4616	0	0.0004	0.5379	0	0

RS2-SLC-SQ11W-ASC-28-Nov-2015_01.24

MODEL / VALIDATION	Thin Ice	Water	Water	Medium/Thick Ice	Thin Ice	Thin Ice
Open Water	0.0044	0.4122	0.5294	0	0.0536	0.0004
Thin Ice	0.297	0.1462	0.1343	0.0041	0.265	0.1534
Medium/ Thick Ice	0	0	0	0.9776	0	0.0224

Appendix C: Summary of Classification Performances after Manual Combination for Entropy-Alpha Wishart Classifier

RS2-SLC-SQ18W-ASC-16-Jun-2015_01.36

MODEL / VALIDATION	Water	Ice
Open Water	1	0
Ice	0.0011	0.9989

RS2-SLC-SQ1W-ASC-17-Jun-2015_01.07

MODEL / VALIDATION	Water	Ice
Open Water	0.6574	0.3426
Ice	0.0495	0.9505

RS2-SLC-SQ11W-DES-17-Jun-2015_14.46

MODEL / VALIDATION	Water	Ice
Open Water	0.999	0.001
Ice	0.0001	0.9999

RS2-SLC-SQ21W-DES-21-Jun-2015_14.29

MODEL / VALIDATION	Water	Ice
Open Water	1	0
Ice	0.0128	0.9872

RS2-SLC-SQ14W-DES-24-Jun-2015_14.42

MODEL / VALIDATION	Water	Ice
Open Water	1	0
Ice	0	1

RS2-SLC-SQ5W-ASC-27-Jun-2015_01.15

MODEL / VALIDATION	Water	Ice
Open Water	1	0
Ice	0.0147	0.9853

RS2-SLC-SQ6W-DES-27-Jun-2015_14.54

MODEL / VALIDATION	Water	Ice
Open Water	0.9937	0.0063
Ice	0.0068	0.9932

RS2-SLC-SQ13W-ASC-30-Jun-2015_01.28

MODEL / VALIDATION	Water	Ice
Open Water	0.8465	0.1535
Ice	0	1

RS2-SLC-SQ5W-ASC-18-Nov-2015_01.15

MODEL / VALIDATION	Water	Ice
Open Water	0.9929	0.0071
Ice	0.0968	0.9032

RS2-SLC-SQ7W-DES-18-Nov-2015_14.54

MODEL / VALIDATION	Water	Ice
Open Water	0.9988	0.0012
Ice	0.0709	0.9291

RS2-SLC-SQ13W-ASC-21-Nov-2015_01.28

MODEL / VALIDATION	Water	Ice
Open Water	0.9977	0.0023
Ice	0	1

RS2-SLC-SQ2W-ASC-25-Nov-2015_01.11

MODEL / VALIDATION	Medium/Thick Ice	Thin Ice
Medium Ice/ Thick Ice	1	0
Thin Ice	0.03360	0.96640

RS2-SLC-SQ9W-DES-25-Nov-2015_14.50

MODEL / VALIDATION	Water	Ice
Open Water	0.8681	0.1319
Ice	0.0932	0.9068

RS2-SLC-SQ11W-ASC-28-Nov-2015_01.24

MODEL / VALIDATION	Water	Ice
Open Water	0.9582	0.0418
Ice	0.1247	0.8753

Appendix D: Summary of Classification Performances of MRF after Manual Combination

RS2-SLC-SQ18W-ASC-16-Jun-2015_01.36

MODEL / VALIDATION	Water	Ice
Open Water	0.8688	0.1312
Ice	0	1

RS2-SLC-SQ1W-ASC-17-Jun-2015_01.07

MODEL / VALIDATION	Water	Ice
Open Water	1	0
Ice	0.0634	0.9366

RS2-SLC-SQ11W-DES-17-Jun-2015_14.46

MODEL / VALIDATION	Water	Ice
Open Water	0.9943	0.0057
Ice	0	1

RS2-SLC-SQ21W-DES-21-Jun-2015_14.29

MODEL / VALIDATION	Water	Ice
Open Water	0.9846	0.0154
Ice	0.0006	0.9994

RS2-SLC-SQ14W-DES-24-Jun-2015_14.42

MODEL / VALIDATION	Water	Ice
Open Water	1	0
Ice	0	1

RS2-SLC-SQ5W-ASC-27-Jun-2015_01.15

MODEL / VALIDATION	Water	Ice
Open Water	1	0
Ice	0.0004	0.9996

RS2-SLC-SQ6W-DES-27-Jun-2015_14.54

MODEL / VALIDATION	Water	Ice
Open Water	0.9996	0.0004
Ice	0.0052	0.9948

RS2-SLC-SQ13W-ASC-30-Jun-2015_01.28

MODEL / VALIDATION	Water	Ice
Open Water	0.9489	0.0511
Ice	0	1

RS2-SLC-SQ5W-ASC-18-Nov-2015_01.15

MODEL / VALIDATION	Water	Ice
Open Water	0.9826	0.0174
Ice	0.0988	0.9012

RS2-SLC-SQ7W-DES-18-Nov-2015_14.54

MODEL / VALIDATION	Water	Ice
Open Water	1	0
Ice	0.1341	0.8659

RS2-SLC-SQ13W-ASC-21-Nov-2015_01.28

MODEL / VALIDATION	Water	Ice
Open Water	0.9983	0.0017
Ice	0	1

RS2-SLC-SQ2W-ASC-25-Nov-2015_01.11

MODEL / VALIDATION	Medium/Thick Ice	Thin Ice
Medium Ice/ Thick Ice	1	0
Thin Ice	0.0633	0.9367

RS2-SLC-SQ9W-DES-25-Nov-2015_14.50

MODEL / VALIDATION	Water	Ice
Open Water	0.9822	0.0178
Ice	0.1027	0.8973

RS2-SLC-SQ11W-ASC-28-Nov-2015_01.24

MODEL / VALIDATION	Water	Ice
Open Water	0.9416	0.0584
Ice	0.1402	0.8598